APPLICATION OF TITANIUM ALLOY BARS FOR STRENGTHENING REINFORCED CONCRETE BRIDGE GIRDERS
(Part A: Shear)

Final Report

SPR 775

Oregon Department of Transportation

APPLICATION OF TITANIUM ALLOY BARS FOR STRENGTHENING REINFORCED CONCRETE BRIDGE GIRDERS

(Part A: Shear)

Final Report

PROJECT SPR 775

by
Jonathan Knudtsen
and
Christopher Higgins, PhD, PE (NY)

for

Oregon Department of Transportation
Research Section
555 13th Street NE, Suite 1
Salem OR 97301

and

Federal Highway Administration
400 Seventh Street, SW
Washington, DC 20590-0003

July 2017

Technical Report Documentation Page

1. Report No. FHWA-OR-RD-18-01	2. Government Accession No.	3. Recipient's Catalog No.
4. Title and Subtitle Application of Titanium Alloy Bars for Strengthening Reinforced Concrete Bridge Girders (Part A: Shear)		5. Report Date July 2017
		6. Performing Organization Code
7. Author(s) Jonathan Knudtsen and Christopher Higgins, PhD, PE (NY)		8. Performing Organization Report No.
9. Performing Organization Name and Address Oregon Department of Transportation Research Section 555 13th Street NE, Suite 1 Salem, OR 97301		10. Work Unit No. (TRAIS)
		11. Contract or Grant No.
12. Sponsoring Agency Name and Address Oregon Dept. of Transportation Research Section and Federal Highway Admin. 555 13th Street NE, Suite 1 400 Seventh Street, SW Salem, OR 97301 Washington, DC 20590-0003		13. Type of Report and Period Covered _______ Report
		14. Sponsoring Agency Code
15. Supplementary Notes		

16. Abstract

Large numbers of conventionally reinforced concrete bridges (RC) were constructed during the interstate highway expansion of the 1950's and remain in the national inventory. Coincidently, deformed steel reinforcing bars were standardized. The standardized deformation requirements dramatically changed bond provisions in all relevant design codes and designers began to use straight-bar terminations of the flexural reinforcing bars where they were no longer required by calculation. This produced terminations in flexural tension zones without special detailing provisions. At the same time, design codes overestimated the concrete contribution to shear resistance and thus designs provided less transverse steel than permissible by modern standards. These poor details combined with heavier loads have resulted in diagonal cracking of the girders. Application of modern design provisions to assess vintage RC members typically results in low predicted capacity. Load restrictions or replacement of bridges is expensive and thus structurally effective and economical strengthening approaches are required.

Near-surface mounting (NSM) of supplemental reinforcing bars has emerged as a common retrofit method for strengthening RC structures. In this method, bars are bonded with an adhesive within grooves that are cut into the surface of the member. The most common reinforcing material used in the NSM application is fiber reinforced polymer (FRP). FRP materials are elastic until fracture thus providing no ductility. In addition, they can debond prematurely limiting the effectiveness of the repair. For this reason, new titanium alloy bars (TiABs) were developed as a potential alternative for FRP bars in NSM applications.

Small diameter (1/4 in.) NSM TiABS were applied to full-size bridge girder specimens that were shear deficient and tested to failure in the laboratory. Two different epoxy materials were considered, as well as two different configurations of TiAB bars (single leg and double leg stirrups). The combined effects of high-cycle fatigue loading and repeated freeze-thaw exposure were investigated to assess long-term durability of the proposed approach and materials.

Results showed that NSM TiABs provided significant increases in the strength when compared to similar unstrengthened specimens. The TiABs were observed to achieve the yield stress prior to/at ultimate. Anchorage of the TiABs was sufficient to produce rupture over the main diagonal cracks. The double leg TiABs were easier to construct and provide additional confinement across the beam soffit. It was determined that some reduction in strength was observed for one of the epoxy materials due to the combined fatigue and environmental effects. Three methods were used to analyze the experimental results which could conservatively predict strength. Strength reduction factors were developed for each method to be used in design.

17. Key Words Titanium; bridge; alloy; concrete; reinforce	18. Distribution Statement Copies available from NTIS, and online.

19. Security Classification (of this report) Unclassified	20. Security Classification (of this page) Unclassified	21. No. of Pages 136	22. Price

SI* (MODERN METRIC) CONVERSION FACTORS

APPROXIMATE CONVERSIONS TO SI UNITS					APPROXIMATE CONVERSIONS FROM SI UNITS				
Symbol	When You Know	Multiply By	To Find	Symbol	Symbol	When You Know	Multiply By	To Find	Symbol
		LENGTH					**LENGTH**		
in	inches	25.4	millimeters	mm	mm	millimeters	0.039	inches	in
ft	feet	0.305	meters	m	m	meters	3.28	feet	ft
yd	yards	0.914	meters	m	m	meters	1.09	yards	yd
mi	miles	1.61	kilometers	km	km	kilometers	0.621	miles	mi
		AREA					**AREA**		
in^2	square inches	645.2	millimeters squared	mm^2	mm^2	millimeters squared	0.0016	square inches	in^2
ft^2	square feet	0.093	meters squared	m^2	m^2	meters squared	10.764	square feet	ft^2
yd^2	square yards	0.836	meters squared	m^2	m^2	meters squared	1.196	square yards	yd^2
ac	acres	0.405	hectares	ha	ha	hectares	2.47	acres	ac
mi^2	square miles	2.59	kilometers squared	km^2	km^2	kilometers squared	0.386	square miles	mi^2
		VOLUME					**VOLUME**		
fl oz	fluid ounces	29.57	milliliters	ml	ml	milliliters	0.034	fluid ounces	fl oz
gal	gallons	3.785	liters	L	L	liters	0.264	gallons	gal
ft^3	cubic feet	0.028	meters cubed	m^3	m^3	meters cubed	35.315	cubic feet	ft^3
yd^3	cubic yards	0.765	meters cubed	m^3	m^3	meters cubed	1.308	cubic yards	yd^3
NOTE: Volumes greater than 1000 L shall be shown in m^3.									
		MASS					**MASS**		
oz	ounces	28.35	grams	g	g	grams	0.035	ounces	oz
lb	pounds	0.454	kilograms	kg	kg	kilograms	2.205	pounds	lb
T	short tons (2000 lb)	0.907	megagrams	Mg	Mg	megagrams	1.102	short tons (2000 lb)	T
		TEMPERATURE (exact)					**TEMPERATURE (exact)**		
°F	Fahrenheit	(F-32)/1.8	Celsius	°C	°C	Celsius	1.8C+32	Fahrenheit	°F

*SI is the symbol for the International System of Measurement

ACKNOWLEDGEMENTS

The authors would like to thank the Oregon Department of Transportation for funding this research. Dr. Matthew Mabey served as the ODOT project coordinator and his assistance and patience is greatly appreciated. The authors also would like to thank the ODOT Technical Advisory Committee for this project and the helpful advice provided by them on the direction of work.

Perryman Company of Houston, PA manufactured the titanium alloy bars and we thank them for their technical assistance in developing the bars used in this study.

This project was made possible through the contributions of many undergraduate research assistants who assisted with the laboratory work including Anthony Quinn, Tyler Redman, Nathanael De Wilde, and Liam Kucey. The technical assistance of Mr. Jeff Gent in the OSU laboratory is also gratefully acknowledged.

DISCLAIMER

TABLE OF CONTENTS

Page

1.0 INTRODUCTION 1
- 1.1 RESEARCH SIGNIFICANCE 1

2.0 LITERATURE REVIEW 3
- 2.1 DEVELOPMENT OF NSM SHEAR STRENGTHENING 3
- 2.2 BOND STRENGTH 4
- 2.2 INNOVATIVE SHEAR STRENGTHENING METHODS 9
- 2.3 ENVIRONMENTAL TESTS 10
- 2.4 FATIGUE 11
- 2.5 DESIGN GUIDEANCE 12
- 2.6 SUMMARY 12

3.0 EXPERIMENTAL PROGRAM 13
- 3.1 SPECIMEN DESIGN 13
- 3.2 CONTROL SPECIMENS 14
- 3.3 SPECIMEN DETAILS 15
- 3.4 INSTRUMENTATION 18
- 3.5 MATERIAL PROPERTIES 19
  - *3.5.1 Concrete 19*
  - *3.5.2 Reinforcing Steel 20*
  - *3.5.3 Titanium 21*
  - *3.5.4 Epoxy 22*
- 3.6 SPECIMEN CONSTRUCTION 23
- 3.7 RETROFITTING METHODOLOGY 24
- 3.8 TESTING METHODOLOGY 26
- 3.9 FATIGUE TEST PROCEDURE 27
- 3.10 FREEZE-THAW TEST PROCEDURE 30
- 3.11 BOND TESTS 31

4.0 EXPERIMENTAL RESULTS 33
- 4.1 GLOBAL BEHAVIOR 33
- 4.2 SPECIMEN T5.24.12.E1 35
- 4.3 SPECIMEN T5.24.12S.E1* 37
- 4.4 SPECIMEN IT6.18.18.E1 39
- 4.5 SPECIMEN IT6.18.12.E1 41
- 4.6 SPECIMEN IT6.18.12.E1.FTG 43
- 4.7 SPECIMEN IT6.18.12.E2 45
- 4.8 SPECIMEN IT6.18.12.E2.FTG 47
- 4.9 SPECIMEN STRENGTH INCREASES 49
- 4.10 CRACK MAPS AND INSTRUMENTATION 50
- 4.11 STRAINS IN STEEL AND TITANIUM ALLOY BARS 53
- 4.12 VERTICAL STRAIN ANALYSIS 56
  - *4.12.1 Panel Strain 56*

4.13 TITANIUM STRAIN FROM PANEL ZONE MEASUREMENTS 60
4.8 FATIGUE AND FREEZE-THAW EFFECTS 62
5.0 COMPARATIVE ANALYSIS 65
5.1 RESPONSE 2000 65
5.2 ACI 318 AND ACI 440 PREDICTED STRENGTH 67
5.3 AASHTO-LRFD PREDICTED STRENGTH 69
5.4 SHEAR STRENGTHENING STRAIN LIMITS 71
5.5 EPOXY COMPARISON 72
5.6 STRAIN COMPATIBILITY 73
5.7 SERVICE-LEVEL PERFORMANCE 75
5.8 STIRRUP DEBONDING R2K ANALYSIS 76
5.9 ACTUAL M/V RATIO R2K ANALYSIS 77
5.10 STRENGTH REDUCTION FACTORS 78
5.11 SUMMARY 80
6.0 CONCLUSIONS 81
6.1 ADDITIONAL RESEARCH 82
REFERENCES 83

LIST OF FIGURES

Figure 3.1: Specimen Naming Convention....13
Figure 3.2: Prediction Plot for Specimen IT6.18.12.E1....14
Figure 3.3: IT Specimen Cross Section....15
Figure 3.4: Specimen T5.24.12.E1 Cross Section....16
Figure 3.5: Specimen T5.24.12S.E1* Cross Section....16
Figure 3.6: Elevation of Specimen T5.24.12.E1....17
Figure 3.7: Elevation of Specimen T5.24.12S.E1*....17
Figure 3.8: Elevation of Specimen IT6.18.18.E1....17
Figure 3.9: Elevation of All Other IT Specimens....18
Figure 3.10: Longitudinal Instrumentation....18
Figure 3.11: Displacement Sensor Locations....19
Figure 3.12: Titanium Alloy Bar (a) Double Leg Titanium Stirrup, (b) Single Leg Titanium Stirrup, (c) Hook Detail....22
Figure 3.13: Cage Construction Process (test section on left)....23
Figure 3.14: Concrete Placement Process....24
Figure 3.15: Groove Cutting Process with Aluminum Saw Guide....25
Figure 3.16: Titanium Installation Process....26
Figure 3.17: Schematic of test setup....27
Figure 3.18: Freezer and Fatigue Schematic....28
Figure 3.19: Specimen in Freezer....29
Figure 3.20: Freezer Temperature Data....30
Figure 4.1: T Beam Load-Deflection Backbone Curves....34
Figure 4.2: IT Beam Load-Deflection Backbone Curves....34
Figure 4.3: Specimen T5.24.12.E1 at Failure(a) Diagonal Cracking, (b) Flexural Failure, (c) Chevron Cracking, (d) Crack Feathering....36
Figure 4.4: Specimen T5.24.12S.E1* at Failure (a) Specimen at Failure, (b) Detail of Main Diagonal Crack, (c) T4 Ruptured at Failure, (d) Web Cracking Viewed from Beneath the Specimen....38
Figure 4.5: Specimen IT6.18.18.E1 at Failure (a) Specimen at Failure, (b) Detail of Main Diagonal Crack, (c) T3 Ruptured at Failure, (d) T2 Chevron Cracking....40
Figure 4.6: Specimen IT6.18.12.E1 at Failure (a) Diagonal Crack on Front Side, (b) Diagonal Crack on Backside, (c) T3 Ruptured at Failure, (d) T6 on Backside....42
Figure 4.7: Specimen IT6.18.12.E1.FTG Freeze-Thaw and Fatigue Damage (a) Efflorescence and Cracking at Titanium Alloy Bar Hook, (b) Efflorescence and Cracking of the Epoxy....43
Figure 4.8: Specimen IT6.18.12.E1.FTG at Failure (a) Front Side Diagonal Crack at End of Test, (b) Back Side Diagonal Crack at End of Test, (c) Video Screenshot of Front Diagonal Crack Immediately After Failure, (d) Crack Feathering at Titanium....44
Figure 4.9: Specimen IT6.18.12.E2 at Failure (a) Specimen at Failure, (b) Detail of Diagonal Crack, (c) T4 Feathering and Epoxy Cracking, (d) T3 Ruptured at Failure....46
Figure 4.10: Specimen IT6.18.12.E2.FTG Freeze-Thaw and Fatigue Damage (a) Epoxy Cracking, (b) Crack Feathering....47
Figure 4.11: Specimen IT6.18.12.E2.FTG at Failure (a) Specimen at Failure, (b) Detail of Diagonal Crack, (c) No Crack Feathering, Debonding, or Rupture at T5 Over Main Diagonal Crack, (d) T4 Ruptured at Failure....48
Figure 4.12: Specimen T5.24.12.E1 Crack Map....50
Figure 4.13: Specimen T5.24.12S.E1* Crack Map....50
Figure 4.14: Specimen IT6.18.18.E1 Crack Map....51
Figure 4.15: Specimen IT6.18.12.E1 Crack Map....51
Figure 4.16: Specimen IT6.18.12.E1.FTG Crack Map....52
Figure 4.17: Specimen IT6.18.12.E2 Crack Map....52
Figure 4.18: Specimen IT6.18.12.E2.FTG Crack Map....53
Figure 4.19: Specimen T5.24.12.E1 Average Panel Vertical Strain....56
Figure 4.20: Specimen T5.24.12S.E1* Average Panel Vertical Strain....57
Figure 4.21: Specimen IT6.18.18.E1 Average Panel Vertical Strain....57

Figure 4.22: Specimen IT6.18.12.E1 Average Panel Vertical Strain 58
Figure 4.23: Specimen IT6.18.12.E1.FTG Average Panel Vertical Strain 58
Figure 4.24: Specimen IT6.18.12.E2 Average Panel Vertical Strain 59
Figure 4.25: Specimen IT6.18.12.E2.FTG Average Panel Vertical Strain 59
Figure 4.26: Specimen IT6.18.12.E1.FTG Internal Stirrup Strain Range 63
Figure 4.27: Specimen IT6.18.12.E2.FTG Internal Stirrup Strain Range 63
Figure 5.1: R2K Beam Model 65
Figure 5.2: Epoxy E2 Voids 73
Figure 5.3: Specimen IT6.18.12.E1 Strain Compatibility S6-T6 74
Figure 5.4: Specimen IT6.18.12.E2 Strain Compatibility S4-T3 74
Figure 5.5: Specimen IT6.18.12.E2.FTG Strain Compatibility S4-T3 (Backbone Curves Shown for Clarity)...........75
Figure 5.6: R2K Debonding (Default Tensile Strength: 252 psi) 76
Figure 5.7: R2K Debonding (Default E = 15,500 ksi)..77

LIST OF TABLES

Table 2.1: Goebel (2011) Reported Epoxy Properties 5
Table 2.2: Sharaky Epoxy Properties 6
Table 2.3: Bond Strength Comparison (U.S. Customary Units) 7
Table 2.4: Bond Strength Comparison (S.I. Units) 8
Table 3.1: Concrete Mix Proportions 20
Table 3.2: Concrete Compressive Strengths 20
Table 3.3: Rebar Properties 21
Table 3.4: Epoxy Properties 23
Table 3.5: Fatigue Testing Intervals 29
Table 3.6: Freeze-Thaw Cycles for Representative Regions in Oregon [Higgins *et al.* 2009] 31
Table 4.1: Summary of Test Results 33
Table 4.2: Strength Increases 49
Table 4.3: Internal Stirrup Strain Gage Results 54
Table 4.4: Titanium Strain Gage Results 55
Table 4.5: Average Panel Vertical Deformations 60
Table 4.6: Calculated Shear in Specimen at Which Titanium Alloy Bars Yield 62
Table 5.1: R2K Prediction Bias 66
Table 5.2: ACI 318 and 440 prediction bias 68
Table 5.3: AASHTO-LRFD Prediction Bias 71
Table 5.4: Service Level Strength Increases 75
Table 5.5: Actual M/V Ratio R2K Analysis 78
Table 5.6: Reduction Factors for E1 Epoxy Specimens 79
Table 5.7: Reduction Factors for all Epoxies Including Long-Term Durability 79

LIST OF APPENDIX FIGURES

Figure A.1: Specimen T5.24.12.E1 Midspan Deflection..1
Figure A.2: Specimen T5.24.12S.E1* Midspan Deflection 2
Figure A.3: Specimen IT6.18.18.E1 Midspan Deflection 2
Figure A.4: Specimen IT6.18.12.E1 Midspan Deflection 3
Figure A.5: Specimen IT6.18.12.E1.FTG Midspan Deflection...3
Figure A.6: Specimen IT6.18.12.E2 midspan deflection...4
Figure A.7: Specimen IT6.18.12.E2.FTG Midspan Deflection...4
Figure A.8: Specimen T5.24.12.E1 Diagonal Sensor Displacement 5
Figure A.9: Specimen T5.24.12S.E1* Diagonal Sensor Displacement...5
Figure A.10: Specimen IT6.18.18.E1 Diagonal Sensor Displacement..6
Figure A.11: Specimen IT6.18.12.E1 Diagonal Sensor Displacement..6
Figure A.12: Specimen IT6.18.12.E1.FTG Diagonal Sensor Displacement 7
Figure A.13: Specimen IT6.18.12.E2 Diagonal Sensor Displacement..7
Figure A.14: Specimen IT6.18.12.E2.FTG Diagonal Sensor Displacement 8
Figure A.15: Specimen T5.24.12.E1 Longitudinal Strain 8
Figure A.16: Specimen T5.24.12S.E1* Longitudinal Strain 9
Figure A.17: Specimen IT6.18.18.E1 Longitudinal Strain 9
Figure A.18: Specimen IT6.18.12.E1 Longitudinal Strain 10
Figure A.19: Specimen IT6.18.12.E1.FTG Longitudinal Strain...10
Figure A.20: Specimen IT6.18.12.E2 Longitudinal Strain 11
Figure A.21: Specimen IT6.18.12.E2.FTG Longitudinal Strain...11
Figure A.22: Specimen T5.24.12.E1 Internal Stirrup Strain 12
Figure A.23: Specimen T5.24.12S.E1* Internal Stirrup Strain 12
Figure A.24: Specimen IT6.18.18.E1 Internal Stirrup Strain 13
Figure A.25: Specimen IT6.18.12.E1 Internal Stirrup Strain 13
Figure A.26: Specimen IT6.18.12.E1.FTG Internal Stirrup Strain...14
Figure A.27: Specimen IT6.18.12.E2 Internal Stirrup Strain 14
Figure A.28: Specimen IT6.18.12.E2.FTG Internal Stirrup Strain...15
Figure A.29: Specimen T5.24.12.E1 Titanium Strain 15
Figure A.30: Specimen T5.24.12S.E1* Titanium Strain 16
Figure A.31: Specimen IT6.18.18.E1 Titanium Strain 16
Figure A.32: Specimen IT6.18.12.E1 Titanium Strain 17
Figure A.33: Specimen IT6.18.12.E1.FTG Titanium Strain 17
Figure A.34: Specimen IT6.18.12.E2 Titanium Strain – Backbone Curves..18
Figure A.35: Specimen IT6.18.12.E2 Titanium Strain – T1 and T2 18
Figure A.36: Specimen IT6.18.12.E2 Titanium Strain – T3...19
Figure A.37: Specimen IT6.18.12.E2 Titanium Strain – T4...19
Figure A.38: Specimen IT6.18.12.E2 Titanium Strain – T5...20
Figure A.39: Specimen IT6.18.12.E2 Titanium Strain – T6...20
Figure A.40: Specimen IT6.18.12.E2.FTG Titanium Strain 21
Figure A.41: Specimen IT6.18.12.E1.FTG Midspan Deflection First Freezer Loading 21
Figure A.42: Specimen IT6.18.12.E2.FTG Midspan Deflection First Freezer Loading 22
Figure A.43: Specimen IT6.18.12.E1.FTG Diagonal Disp. First Freezer Loading 22
Figure A.44: Specimen IT6.18.12.E2.FTG Diagonal Disp. First Freezer Loading 23
Figure A.45: Specimen IT6.18.12.E1.FTG Longitudinal Strain First Freezer Loading 23
Figure A.46: Specimen IT6.18.12.E2.FTG Longitudinal Strain First Freezer Loading 24
Figure A.47: Specimen IT6.18.12.E1.FTG Internal Stirrup Strain First Freezer Loading 24
Figure A.48: Specimen IT6.18.12.E2.FTG Internal Stirrup Strain First Freezer Loading 25
Figure A.49: Specimen IT6.18.12.E1.FTG Titanium Strain First Freezer Loading 25
Figure A.50: Specimen IT6.18.12.E2.FTG Titanium Strain First Freezer Loading 26
Figure A.51: Specimen IT6.18.12.E1.FTG Fatigue Midspan Deflection..26

Figure A.52: Specimen IT6.18.12.E2.FTG Fatigue Midspan Deflection....27
Figure A.53: Specimen IT6.18.12.E1.FTG Fatigue Diagonal Sensor Elongation....27
Figure A.54: Specimen IT6.18.12.E2.FTG Fatigue Diagonal Sensor Elongation....28
Figure A.55: Specimen IT6.18.12.E1.FTG Fatigue Long. Strain at 210 kips (934 kN)....28
Figure A.56: Specimen IT6.18.12.E2.FTG Fatigue Long. Strain at 210 kips (934 kN)....29
Figure A.57: Specimen IT6.18.12.E1.FTG Fatigue Stirrup Strain at 210 kips (934 kN)....29
Figure A.58: Specimen IT6.18.12.E2.FTG Fatigue Stirrup Strain at 210 kips (934 kN)....30
Figure A.59: Specimen IT6.18.12.E1.FTG Fatigue Titanium Strain at 210 kips (934 kN)....30
Figure A.60: Specimen IT6.18.12.E2.FTG Fatigue Titanium Strain at 210 kips (934 kN)....31
Figure B.1: Grade 60 #11 Tensile Test Results....1
Figure B.2: Grade 60 #6 Tensile Test Results....2
Figure B.3: Grade 40 #4 Tensile Test Results....2
Figure B.4: 1/4 in. Titanium Alloy Bar Tensile Test Results – E1 Specimens....3
Figure B.5: 1/4 in. Titanium Alloy Bar Tensile Test Results – E2 Specimens....3
Figure C.1: Specimen T5.24.12.E1 R2K Prediction Curve....1
Figure C.2: Specimen T5.24.12S.E1* R2K Prediction Curve....2
Figure C.3: Specimen IT6.18.18.E1 R2K Prediction Curve....2
Figure C.4: Specimen IT6.18.12.E1 R2K Prediction Curve....3
Figure C.5: Specimen IT6.18.12.E1.FTG R2K Prediction Curve....3
Figure C.6: Specimen IT6.18.12.E2 R2K Prediction Curve....4
Figure C.7: Specimen IT6.18.12.E2.FTG R2K Prediction Curve....4

LIST OF APPENDIX TABLES

Table D.1: Material Properties.... iii
Table D.2: Groove Cutting Costs (USD) Per Square Foot [0.093 m^2].... iii
Table D.3: NSM Repair Costs (USD) Per Square Foot [0.093 m^2]....iv

1.0 INTRODUCTION

Many bridges built in the United States between 1940 and 1960 do not meet the modern requirements for shear. This is due to increased vehicle traffic as well as better code models for shear. Additionally, many of these bridges are reaching the end of their intended service lives. Strengthening these bridges has emerged as a cost-effective alternative to replacing them or posting load ratings.

Over the past 15 years, a method of shear strengthening called near-surface mounting (NSM) has been developed for shear and flexural strengthening of beams. This method involves epoxying a bar or strip into a groove cut on the side of a concrete beam. It was first developed for use with steel bars, but due to problems with corrosion, most recent research has focused on the use of fiber-reinforced polymer (FRP) bars.

This study proposes the use of hooked titanium alloy bars (TiABs) instead of FRP in NSM shear strengthening applications. The problems with using FRP bars are well documented, and include premature debonding, brittle failure, and lack of mechanical anchorage. The hooked ends of the titanium alloy bars provide anchorage in the event of bond failure, and allow the bar to reach higher stresses, meaning the repair is more efficient. Because scale effects can be significant when working with concrete, full-scale specimens with realistic internal reinforcement were used.

1.1 RESEARCH SIGNIFICANCE AND OBJECTIVES

This research investigates the application of TiABs for strengthening reinforced concrete bridge girders deficient in shear. TiABs were used in the NSM application, which has not previously been investigated. The objectives of the research were to experimentally test the effectiveness of TiAB shear retrofits to simulated 1950's era bridge girders using different TiAB configurations, compare the behavior and strength when using different epoxy bonding materials for anchoring the TiABs in the concrete substrate, and to assess deterioration and long-term durabilityt considering the influences of simultaneously applied freeze-thaw and fatigue cycles. The experimental results are used to compare analysis methods, for development of a design approach.

2.0 LITERATURE REVIEW

This section summarizes previous research done in the field of NSM shear strengthening. The historical development of NSM is presented, as well as more recent research. Recent research has largely focused on the interface between the NSM retrofit and the concrete, either quantifying bond strengths or testing mechanical anchorages.

2.1 DEVELOPMENT OF NSM SHEAR STRENGTHENING

The NSM technique was first used in Europe in 1949 (Asplundh 1949). In this instance, a bridge deck required flexural strengthening, so steel bars were placed in grooves which were filled in with grout. The method was successful, but likely due to steel's corrosive properties, it did not attract much interest until carbon fiber rods became a viable alternative.

De Lorenzis and Nanni (2001a) were the first to apply NSM CFRP rods in shear strengthening applications. They built eight T-shaped beams, each with a height of 16 in., and an a/d ratio of 3.0. The beams were tested in four-point bending. Six of the beams had no internal steel stirrups, and the authors used these to test the effects of changing the spacing and orientation of the FRP rods, and providing anchorage in the flange. Anchoring the bars in the flange was found to be the most efficient way to increase shear capacity.

Two of the eight beams were built with internal steel stirrups, one of which was a control specimen. The other specimen was strengthened with vertical NSM rods without anchorage, and provided an increase in capacity of 35%. As expected, the specimen with internal stirrups showed a smaller strength increase. Two failure mechanisms were observed: Sudden loss of concrete cover over the longitudinal steel, due to the absence of internal steel stirrups, and splitting of the epoxy cover over the NSM FRP rods.

Barros and Dias (2006) tested a series of rectangular beams, with heights of 150 mm and 300 mm, and a/d ratios of 2.0. The beams were strengthened with either externally bonded CFRP sheets, or NSM CFRP strips mounted in narrow slits. Internal steel stirrups were not provided for the strengthened specimens. The authors concluded that the NSM retrofit was the most effective, as the CFRP sheets increased the strength by 54%, while the NSM CFRP increased the strength by 83%. The NSM retrofit also provided higher ductility.

In previous research at OSU, Johnson (2011) tested eight T-shaped specimens with the same dimensions as those used in the present study. Internal stirrups were provided at 18 in. (457 mm) or 22 in. (559 mm). The beams were strengthened in shear using NSM CFRP strips spaced at 6 in. (152 mm) or 12 in. (305 mm). The CFRP strips provided strength increases between 29 and 101 percent. The specimens primarily failed in shear-compression, with significant debonding and slip of the CFRP strips. However, the specimens were significantly stronger than predicted. One of the specimens was subjected to fatigue loading, while another specimen was subjected to simultaneous fatigue loading and freeze-thaw conditions. However, these loading conditions produced no significant effect on the strength or stiffness of the specimens when compared to control specimens.

2.2 BOND STRENGTH

An accurate estimate of bond strength is critical to estimating the strength of NSM systems. A high bond strength reduces the active bond length, increasing the strain in the bar. Much of the research related to NSM in the last 15 years has focused on quantifying this bond strength. Up to yield, the average bond stress can be assumed to be half the peak stress, based on a triangular stress distribution. It can be calculated based on bar diameter, bar stress, and development length, using the following equation derived from force equilibrium:

$$\boldsymbol{\tau_b = \frac{d_b}{4l_{db}} f_{fd}} \qquad \textbf{[2.1]}$$

This equation, solved for development length, has been incorporated into ACI 440.2R-08 for NSM applications. For τ_b the code gives a range of 500 to 3000 psi (3.5 to 20.7 MPa), and recommends using a value of 1000 psi (6.9 MPa). These values are based on results from research presented in this section. For cases in which failure occurs in the concrete or at the concrete-epoxy interface, this equation still applies, but provides a lower bound estimate of bond strength.

De Lorenzis and Nanni (2001b) investigated the bond strength of NSM bars using beam pull-out tests. Five specimens were tested, each 48 in. (1219 mm) long and 10 in. (254 mm) in height. Each specimen was reinforced with one 3/8 in. (9.5 mm) NSM bar, with no internal steel. The epoxy had a compressive modulus of 400 ksi (2757 MPa), and a tensile strength of 2.00 ksi (13.8 MPa).The groove size varied from 1.33 to 2.67 times the bar diameter, and the bonded length varied from 6 to 18 times the bar diameter. Despite these variations, the average bond strength was found to be relatively constant, with a mean value of 1233 psi, and a COV of 5.7%. A slight decrease in bond stress was observed with increasing bond length.

Hassan and Rizkalla (2004) investigated the bond properties of NSM CFRP bars. They tested T-shaped beams with spans of 98.4 in. (2500 mm), and beam heights of 11.8 in. (300 mm). The beams were strengthened in flexure using 0.375 in. (9.5 mm) NSM CFRP bars. Two epoxies were used: Duralith-gel, with a compressive modulus of 174 ksi (1200 MPa) and tensile strength of 6.96 ksi (48 MPa), and Kemko 040, with a compressive modulus of 435 ksi (3000 MPa) and a tensile strength of 8.99 ksi (62 MPa). The embedment length varied from 5.9 in. (150 mm) to 47.2 in. (1200 mm). For all specimens, the mode of failure was splitting of the concrete surface at the concrete-epoxy interface. A decrease in average bond strength was observed with increasing bonded lengths. The authors report average bond strengths of 344 psi (2.37 MPa) and 329 psi (2.27 MPa) for Duralith-gel and Kemko 040 respectively. These values are very low when compared with other tests. This is likely because the average bond stress was calculated using the entire bonded length, which was between 3 and 10 times higher than the bonded lengths used in other studies. The debonding occurred where the internal steel terminated, and the authors note that this significantly affected the results. Since internal steel stirrups are not terminated, this study has limited applicability to shear strengthening applications.

Sena Cruz and Barros (2004) tested nine beam pull-out specimens strengthened with NSM FRP strips. The beams were 7.1 in. (180 mm) in height, and were tested with 25.6 in. (650 mm) spans. The FRP strip area was the equivalent of a 0.16 in. (4.1 mm) diameter bar. Using this conversion, the bonded lengths were 10d_b, 15d_b, and 20d_b. The epoxy type is not reported, but the tested tensile strength was 3.74 ksi (25.8 MPa). Three values of concrete strength were used: 10,000 psi (70 MPa), 6500 psi (45 MPa), and 5000 psi (35 MPa). The authors report that bond stress decreases with bond length, but is not affected by concrete strength. The reported bond stress values range from 1890 psi (13.0 MPa) to 2650 psi (18.3 MPa).

Soliman *et al.* (2011) investigated the bond properties of NSM CFRP and GFRP bars using modified pull-out tests. A group of specimens was subjected to freeze-thaw conditions for comparison with control specimens. The groove dimensions were either 1.5 or 2.0 times the bar diameter, and were filled with either epoxy or cement grout. The epoxy had a compressive modulus of 217 ksi (1493 MPA), and a tensile strength of 6.31 ksi (43.5 MPa). Bonded lengths varied from 6 to 48 times the bar diameter, though bars embedded more than 24 times their diameter developed their full ultimate stress and ruptured. The majority of the specimens were tested with 3/8 in. (9.5 mm) CFRP bars. For these specimens, the average bond stress was found to be inversely correlated to the bonded length, and for specimens not subjected to freeze-thaw, it ranged from 1530 psi (10.56 MPa) to 2880 psi (19.87 MPa). The authors state that this is due to non-uniform stress distribution over the longer lengths. Concrete tension failure was the primary failure mode, in some cases accompanied by splitting of the epoxy cover. Changes in the groove dimensions had a negligible effect on the average bond stress. Specimens tested with 1/2 in. (12.7 mm) bars experienced bar slip before concrete tension failure, and thus developed lower bond stresses. For the larger bars, the bond stress varied between 777 psi (5.36 MPa) and 1580 psi (10.90 MPa). The same decrease in average bond stress with increasing bond length was observed. Surprisingly, the less stiff GFRP bars tended to develop higher bond stresses. The authors do not comment on why this might be. The specimens grouted with cement had bond stresses ranging from 355 psi (2.45 MPa) to 698 psi (4.81 MPa). The specimens subjected to freeze-thaw conditions had slightly lower average bond stresses, and splitting of the epoxy cover became the dominant failure method.

Goebel (2011) used modified pull-out tests to quantify the bond strength of NSM CFRP strips using three different epoxies. The properties of these epoxies are listed in Table 2.1: Goebel (2011) reported epoxy properties. Epoxy E1 corresponds to epoxy E1 used in the present study, while epoxy E3 corresponds to epoxy E2 used in the present study.

Table 2.1: Goebel (2011) Reported Epoxy Properties

Epoxy Type	Compressive Modulus ksi (GPa)	Tensile Strength ksi (MPa)
E1: Concresive 1420	450 (3.06)	4.0 (27.6)
E2: Hilti Hit-Re 500-SD	216 (1.49)	6.31 (43.5)
E3: Unitex Pro-Poxy 400	270 (1.86)	Not reported

Environmental exposure tests, including submersion and freeze thaw under varying wet and dry conditions, were also performed and compared to control specimens. The control specimens for epoxies E1, E2, and E3, had average bond strengths of 1010 psi, 1200 psi, and 760 psi respectively. Epoxies E1 and E2 did not show any measurable decrease in bond strength after environmental exposure. Epoxy E3, however, exhibited reduced bond strength. Unlike Sharaky *et al.* (2013) below, the authors reported no correlation between epoxy ductility and bond strength.

Using the same E1 epoxy as Goebel, Johnson (2011) conducted modified pull-out tests on NSM CFRP strips mounted in 6 in. x 12 in. (152 mm x 305 mm) cylinders. Bond lengths tested were 5 in. (127 mm), 2.5 in. (64 mm), and 1.25 in. (32 mm). Nine sets of three cylinders were tested, but six of the sets had CFRP strips with smooth surfaces, and thus failed at very low loads. For the nine remaining specimens, the average bond strength was 1051 psi (7.24 MPa), with a COV of 23.1%. Bond strength decreased slightly with increasing bond length.

Sharaky *et al.* (2013) tested 32 specimens, varying the FRP type, bar diameter, compressive modulus, and epoxy type. A modified pull-out test was used, in which the flanges of a concrete channel were put in bearing, while the NSM bar was mounted in the web, thus limiting compression near the bar. The bar diameters varied between 0.31 in. (8 mm) and 0.47 in. (12 mm). The bonded length was held constant at 7.56 in. (192 mm). The properties of the four epoxies tested are listed in Table 2.2. Epoxies C and D were the same as epoxy B, but used an additive to reduce stiffness.

Table 2.2: Sharaky Epoxy Properties

Epoxy Type	Compressive Modulus ksi (MPa)	Tensile Strength ksi (MPa)
A	836 (5760)	2.73 (18.82)
B	1160 (8000)	3.33 (22.96)
C	1039 (7160)	3.24 (22.34)
D	1000 (6900)	3.05 (21.00)

Most of the specimens were tested using epoxy A. They showed very consistent bond stress values, with an average bond stress of 1110 psi (7.63 MPa) and a COV of 5.5%. All these specimens displayed longitudinal cracking of the epoxy at failure. Specimens using epoxies B, C, and D had average bond stress values of 1440 psi (9.94 MPa), 1540 psi (10.64 MPa), and 1650 psi (11.38 MPa) respectively. No longitudinal cracking was observed for these specimens. The authors concluded that epoxies with lower stiffness allow better distributions of stress over the bond length, resulting in improved load capacity and ductility. The authors also noted that for all specimens, failure occurred in the epoxy or at the bar-epoxy interface, and conclude that the concrete strength had no effect on the specimens tested. Groove dimensions and bar surface treatment were also varied, but had minimal effect on the bond strength.

Table 2.3 provides a summary of the epoxies used in each study and their representative bond strength. The list is not meant to be exhaustive, as each study included many specimens with varying bar diameters and bonded lengths. Thus a representative sample from each study was selected for comparison. An average value is reported where multiple samples had the same bar diameter and bonded length.

Table 2.3: Bond Strength Comparison (U.S. Customary Units)

Authors	Test Type	Epoxy	Compressive Modulus ksi	Tensile Strength ksi	Bar Diameter in.	Bonded length	Average Bond psi	Failure mode
De Lorenzis & Nanni (2001)	Beam	Master Builders	400	2.00	0.375	$12d_b$	1216	SE, C
Hassan & Rizkalla (2004)	Beam	Duralith-gel	174	6.96	0.375	$58d_b$	435	C
		Kemko 040	435	8.99	0.375	$58d_b$	421	C
Sena Cruz and Barros (2004)	Beam	Not reported	Not reported	3.74	CFRP strips	$20d_b$*	2090	SE
Wahab (2008)	Beam	Sikadur 30	390	3.60	0.375	$5.3d_b$	1700	S
Soliman *et al.* (2011)	Modified pull-out	Hilti HIT RE 500	217	6.31	0.375	$18d_b$	1888	SE, C
Goebel (2011)	Modified pull-out	E1: Concresive	450	4.00	CFRP strips	$10d_b$*	1010	C, S
		E2: Hilti HIT RE 500	216	6.31	CFRP strips	$10d_b$*	1200	C, S
		E3: Pro-poxy	270	Not reported	CFRP strips	$10d_b$*	760	C, S
Johnson (2011)	Modified pull-out	E1: Concresive	450	4.00	CFRP strips	$10d_b$*	1051	C, S
Sharaky *et al.* (2013)	Modified pull-out	A: BASF MBRACE	836	2.73	0.315	$24d_b$	1088	SE, C
		B, C, and D: ROBERLO POLYFIXER with varying amounts of additive	1160	3.33	0.315	$24d_b$	1484	SE, C
			1039	3.24	0.315	$24d_b$	1543	SE, C
			1000	3.05	0.315	$24d_b$	1650	SE, C

* Based on equivalent bar area for CFRP strips
SE = Splitting of Epoxy Cover
C = Concrete Cracking
S = Slip of bar

Table 2.4: Bond Strength Comparison (S.I. Units)

Authors	Test Type	Epoxy	Compressive Modulus GPa	Tensile Strength MPa	Bar Diameter mm	Bonded length	Average Bond MPa	Failure mode
De Lorenzis & Nanni (2001)	Beam	Master Builders	2.76	13.79	9.5	12d_b	8.38	SE, C
Hassan & Rizkalla (2004)	Beam	Duralith-gel	1.20	47.99	9.5	58d_b	3.00	C
		Kemko 040	3.00	61.99	9.5	58d_b	2.90	C
Sena Cruz and Barros (2004)	Beam	Not reported	Not reported	25.79	CFRP strips	20d_b*	14.41	SE
Wahab (2008)	Beam	Sikadur 30	2.69	24.82	9.5	5.3d_b	11.72	S
Soliman *et al.* (2011)	Modified pull-out	Hilti HIT RE 500	1.50	43.51	9.5	18d_b	13.02	SE, C
Goebel (2011)	Modified pull-out	E1: Concresive	3.10	27.58	CFRP strips	10d_b*	6.96	C, S
		E2: Hilti HIT RE 500	1.49	43.51	CFRP strips	10d_b*	8.27	C, S
		E3: Pro-poxy	1.86	Not reported	CFRP strips	10d_b*	5.24	C, S
Johnson (2011)	Modified pull-out	E1: Concresive	3.10	27.58	CFRP strips	10d_b*	7.25	C, S
Sharaky *et al.* (2013)	Modified pull-out	A: BASF MBRACE	5.76	18.82	8.0	24d_b	7.50	SE, C
		B, C, and D: ROBERLO POLYFIXER with varying amounts of additive	8.00	22.96	8.0	24d_b	10.23	SE, C
			7.16	22.34	8.0	24d_b	10.64	SE, C
			6.90	21.03	8.0	24d_b	11.38	SE, C

* Based on equivalent bar area for CFRP strips
SE = Splitting of Epoxy Cover
C = Concrete Cracking
S = Slip of bar

The calculated bond stresses vary greatly from study to study. This is even the case for Soliman and Goebel, who used the same Hilti epoxy. The epoxy properties also vary greatly, with the compressive modulus ranging from 174 ksi (1.20 GPa) to 1160 ksi (8.00 GPa). No clear correlation can be drawn between the epoxy properties and the bond strength. However, the results do tend to fall within the range prescribed by ACI 440.2R-08. More research, with more accurate test methods, is needed in this area.

2.2 INNOVATIVE SHEAR STRENGTHENING METHODS

Khalifa and Nanni (2000) tested six T-shaped beams strengthened with various configurations of externally bonded FRP sheets. Three of these beams are of interest to this study. The beam height was 15.9 in. (405 mm), with an a/d ratio of 3.0. The beams were tested in four point bending. No internal steel stirrups were provided. One beam was strengthened with CFRP strips applied to the beam sides. A second beam was strengthened with U-shaped CFRP strips wrapped all the way around the web. The third beam was similar to the second, except that the strips extended into the flange providing anchorage. For the first two beams, failure was initiated by CFRP debonding, while the third beam failed in flexure. The increases in shear capacity over the control specimen were 35%, 72%, and 145%, respectively. These numbers do not represent realistic strength gains since the base specimen did not include any internal steel stirrups. However, the study showed that anchoring the strips in the flange resulted in a strength increase significantly larger than the other specimens.

Galal and Mofidi (2010) developed an innovative method for shear strengthening by mechanically anchoring unbonded carbon fiber sheets to a beam. Three T-shaped beams were tested in four point bending. The beam height was 11 in. (280 mm), with an a/d ratio of 2.0. #3 (#10) internal steel stirrups spaced at 9.8 in. (250 mm) were provided. The first beam was a control specimen, while the second was strengthened with bonded external CFRP U-shaped wraps, and the third was strengthened with an innovative mechanical anchoring system. This system involved wrapping the ends of the U-shaped CFRP sheets around steel bars mounted on both sides of the web-flange joint. The steel bars were then bolted into the flange of the beam. No epoxy or bonding agent was used for this beam. The strengthened beams resulted in 27% and 48% increases in shear strength over the control specimen. This study showed that it is possible to increase the shear strength even without bonding the retrofitting materials to the concrete surface.

Rahal and Rumaih (2011) tested three T-shaped beams strengthened with NSM CFRP, as well as a control specimen. The beam height was 19.7 in. (500 mm), with an a/d ratio of 3.0, The beams were tested in four point bending. 0.25 in. diameter (6 mm) internal steel stirrups were provided for each specimen, spaced at 7.9 in. (200 mm). Each of the three beams were strengthened with 0.315 in. (8 mm) diameter CFRP bars on one half, and 0.315 in. (8 mm) diameter steel bars on the other half, both spaced at 7.9 in. (200 mm). For the first beam, the bars extended the length of the web. The second beam had CFRP bars extending through the flange, providing additional anchorage. For the third beam, the bars were placed at a 45° angle, but without anchorage in the flange. In all cases, the section strengthened with steel failed first. It was then clamped, allowing the other section to be tested. The CFRP provided increases of 47, 69, and 92 percent, respectively, over the control beam. Of particular interest to this study is the 22% greater increase in strength provided by anchoring the CFRP rods in the flange.

Jalali *et al.* (2012) tested five rectangular beams strengthened with custom made NSM FRP bars, as well as a control specimen. The beams were 9.8 in. (250 mm) deep, with an a/d ratio of approximately 3.0. 0.25 in. (6 mm) diameter internal steel stirrups were provided, spaced at 5.9 in. (150 mm). Two of the beams were strengthened with straight bars, while the other three beams were strengthened with anchored bars. The anchored bars were I-shaped, with the top and bottom rods aligned parallel to the beam axis. The specimens with anchored bars provided 12.41 and 13.93 percent greater maximum load, when compared to the non-anchored specimens. The failure mode for the anchored bar specimens was cover spalling, as the anchors did not penetrate into the concrete core.

In previous research at OSU, Amneus (2014) and Barker (2014) used titanium alloy bars to strengthen full-scale beams in flexure at poorly detailed flexural bar anchorages. The beams were 48 in. (1220 mm) in height, and were 26 ft. (7.92 m) long. The titanium alloy bars were 0.625 in. (15.9 mm) in diameter, and had 90 degree hooks at each end for anchorage. The beams were tested to failure under four-point bending. The hooks worked as intended, preventing the bars from completely debonding. The authors also used the titanium alloy bars to strengthen an in-service bridge, and reported a cost savings of 30% compared with CFRP bars.

2.3 ENVIRONMENTAL TESTS

Mitchell (2010) did freeze-thaw cycles on 4 in. (102 mm) thick concrete slabs strengthened with NSM FRP strips. The slabs were tested in four point bending with 55 in. (1397 mm) spans. Bond pull-out tests were also done using a C-shaped concrete section. Two adhesive types were used: Kemko 038 epoxy, and Target 1118 cementitious grout. The slabs were subjected to 300 freeze-thaw cycles. The freezer was set at -30°C for 5 hours, and then ramped up to 20°C, where it remained for 70 minutes. On each thaw cycle, the beams were submerged in warm water for the full 70 minutes. The pull-out specimens were only subjected to 150 cycles. For specimens strengthened with epoxy, the pull-out specimens had an average strength reduction of 27%, while the slabs only showed a strength reduction of 2% to 8%. The specimens strengthened with cementitious grout did not lose strength after freeze thaw cycles, though they were still significantly weaker than the specimens strengthened with epoxy.

As part of the bond pull-out test study above, Soliman *et al.* (2011) subjected 10 specimens to 200 cycles of freeze-thaw before testing them. The freezer was set at -20°C and 80% relative humidity for 12 hours, followed by 25°C and 100% relative humidity for 6 hours. The specimens were precracked to 30% of their failure load. The test results were compared with control specimens. The specimens using epoxy adhesive had strength reductions ranging from 8 to 14%, while the specimens using cement adhesive had strength reductions ranging from 30 to 45%.

Goebel (2011), as part of the bond pull-out tests above, did pull-out tests on 18 specimens that had been subjected to 400 cycles of freeze-thaw. The full cycle was 3 hours long, and the specimens were fully submerged in water for 30 minutes every day (every eight cycles) during a thaw cycle. Epoxies E1 and E2 (Concresive and Hilti) did not show any strength reduction compared to control specimens. Epoxy E3 (Pro-poxy) had an average strength reduction of 35.4%. While Soliman and Goebel both used the same Hilti epoxy, only Soliman reported strength reductions. This may indicate that Soliman's longer cycles with high relative humidity were more aggressive, even though only half as many cycles were done.

Johnson (2011) did 400 freeze-thaw cycles on a full-scale beam strengthened in shear with NSM FRP strips, while simultaneously subjecting it to fatigue loading. The beam had the same dimensions as those used in the present study. The CFRP strips had cross-sectional areas of 0.05 in^2 (32.3 mm^2), and were spaced at 6 in. (152 mm). The freezer was set to vary between -20°C and 16°C, with ramp times of 30 minutes, and soak times of 1 hour. Water was applied to the surface once per day (every eight cycles). No strength reduction was observed for this specimen, possibly because of a higher concrete strength when it was tested.

2.4 FATIGUE

Wahab *et al.* (2008) tested the fatigue performance of NSM CFRP rods using five small-scale beam tests. The beams were 5.9 in. (150 mm) deep and were tested over a span of 19.7 in. (300 mm). The beams were strengthened with a single NSM CFRP bar 0.375 in. (9.5 mm) in diameter. The bonded length was 2.0 in. (50 mm). The first beam was broken under monotonic loading, while the remaining four beams were subjected to cyclic loading. The load ranges were 10%-70%, 10%-65%, 10%-60%, and 10%-55%. The first three fatigue beams reached failure. The last beam, with a load range of 45%, sustained 1,000,000 cycles without failing. Failure occurred at the bar-epoxy interface. For the monotonically loaded specimen, the average bond stress was 1700 psi (11.81 MPa). The three beams that failed under fatigue loading had an average bond stress of 1020 psi (7.00 MPa), or about 60% of the static bond stress. Very short bond lengths were used for this test, meaning the reported bond stresses may be higher than is realistic.

Johnson (2011), as part of the study described above, tested two full-scale beams strengthened with CFRP strips under fatigue loading. The first beam was subjected to 1,000,000 cycles, with a load range of 11.7% to 26.0%. The second beam was simultaneously subjected to freeze-thaw cycles, and was fatigued for 2,400,000 cycles with a load range of 11.7% to 21.4%. Both beams showed strength increases with respect to the control specimen, suggesting that fatigue loading does not decrease the strength of NSM shear strengthening systems.

Fernandes *et al.* (2014) did fatigue tests using direct pullout tests, and load tests on slab specimens. The pullout samples were strengthened with a single CFRP strip with an area of 0.022 in^2 (14 mm^2), with a bonded length of 3.94 in. (100 mm). This results in an equivalent bonded length of $24d_b$. Nine pullout samples were tested. The first three were tested under monotonic loading to establish the maximum pullout force. The second set (S2) was tested with a load range of 23%-52%, and the third set (S3) were tested with a load range of 26%-58%. The S2 series did not reach fatigue failure after 3 million cycles. The three S3 specimens failed after 95,000, 376,000, and 561,000 cycles. Despite the scatter, they all failed by progressive debonding of the CFRP at the epoxy/CFRP interface. For all three specimens, a large initial slip tapered off, before increasing again immediately prior to failure. The authors also tested five slabs with thicknesses of 3.15 in. (80 mm), and spans of 71 in. (1800 mm). The slabs had internal flexural steel, and were strengthened with three NSM CFRP strips. One slab was tested monotonically to failure, while the other four were subjected to 2 million fatigue cycles with the following stress ranges: 42.4%-74.8%, 26.2%-47.8%, 51.2%-71%, and 62.0%-83.1%. After being fatigued, the slabs were tested monotonically to failure. Like Johnson (2011) above, all four slabs showed significant strength increases with respect to the control specimen. The authors conclude that the fatigue cycles did not affect the ultimate capacity of the slabs.

2.5 **DESIGN GUIDEANCE**

The current design code for FRP strengthening applications is ACI 440.2R-08: Design and Construction of Externally Bonded FRP Systems. This document specifies minimum groove dimensions, edge distances, and approximate bond stress values to be used in design. While this code provides detailed design provisions for externally bonded CFRP systems, it does not prescribe design procedures for NSM systems in the same detail. The applicable details of this design guide are reviewed in detail in Section 5.2.

2.6 **SUMMARY**

Research on the reliable bond strength of NSM shear strengthening systems has produced widely varying results. No clear correlation can be drawn across studies between bond strength and epoxy properties, FRP bar properties, or test type. This makes it very difficult to develop code equations for this method, and in practice means designers use very conservative values, limiting the effectiveness of this repair option.

Because the bond properties are so unreliable, there have been many attempts to develop mechanical anchorages for NSM bars. These tests have shown that anchoring the bars can delay debonding and significantly increase shear capacity. However, most of the methods developed are somewhat impractical in that they require specifically prefabricated bars or would be very difficult to implement in the field. Thus there is a need for a strengthening technique that does not rely on bond strength to transfer shear, while also being easy to implement.

While there have been several studies focusing on the fatigue and freeze-thaw properties of NSM systems, most of them have used small-scale beams. Johnson (2011) is the only study which used full-scale specimens, and only two specimens were tested. Thus, there is a need for full-scale specimens to further investigate environmental and fatigue effects on epoxy in shear strengthening NSM systems.

3.0 EXPERIMENTAL PROGRAM

For this study, seven full-scale beam specimens were constructed. After casting, the specimens were strengthened in shear with NSM titanium alloy bars fabricated with hooks for end anchorage. The specimens were then tested to failure. The specimens were designed to fail in diagonal tension, in order to quantify the contribution of the titanium alloy bars to the strength of the specimen. Two specimens were tested in positive moment bending, while the other five were inverted and tested in the more critical negative moment configuration. The T beams represent high shear, low moment sections near an abutments. The IT beams represent high shear, high moment sections of continuous girders at interior support locations. The naming convention used to identify the specimens is shown in Figure 3.1.

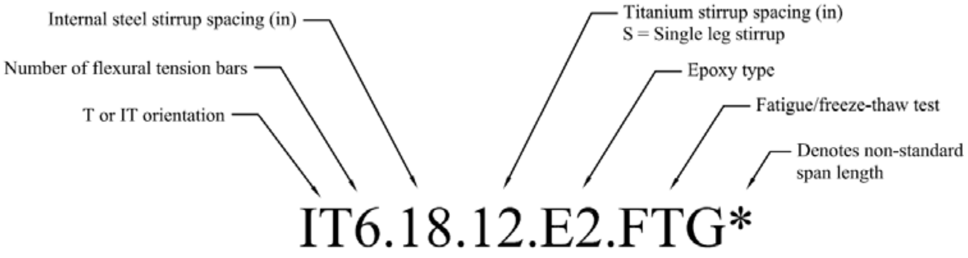

Figure 3.1: Specimen Naming Convention

3.1 SPECIMEN DESIGN

The beams used in this study were based on typical 1950's-era bridge girders, as documented by Higgins, *et al.* (2005). The internal flexural steel reinforcing was chosen based on realistic reinforcing ratios from that era. A computer analysis program called Response 2000 (R2K) (Bentz, 2000) was used in designing the transverse reinforcement. This program is based on the Modified Compression Field Theory (MCFT). In the MCFT model, increasing the transverse reinforcing pressure increases the shear strength of a beam, but not linearly. As the strains in the flexural bars increase, the effect of adding transverse reinforcement decreases. The effectiveness of R2K at predicting the shear capacity of beams was demonstrated by Higgins, *et al.* (2005) who tested 44 full-scale beams with the same dimensions as those used in the current study. The authors reported an average bias of 2% between the R2K predicted and tested strength values, with a coefficient of variation of 6.7%, indicating a high level of reliability.

Using R2K, the relationship between shear and transverse reinforcing pressure was plotted. The predicted response for specimen IT6.18.12.E1 is shown in Figure 3.2. The internal steel stirrups were designed to give transverse reinforcing pressures near the bottom of the steep slope shown in the figure, while still meeting the modern requirement of minimum stirrup spacing. This was done to avoid artificially overemphasizing the influence of the supplemental reinforcement. The design intent was to allow the beams to fail in diagonal tension, even after being strengthened with titanium alloy bars. The transverse reinforcing pressure (psi) was calculated as:

$$v = \frac{A_s f_{ys}}{b s_s} + \frac{A_{ti} f_{yti}}{b s_{ti}} \qquad [3.1]$$

where A_s and A_{ti} are the cross sectional areas of the steel and titanium alloy bars, f_{ys} and f_{yti} are the yield strengths of steel and titanium, b is the width of the web, and s_s and s_{ti} are the steel and titanium stirrup spacings.

In order to obtain more reliable predictions for the specimen geometry used in the present study, the results from R2K were modified using the bias and standard deviation calculated by Higgins (2005). Prediction plots for each specimen are shown in Appendix C.

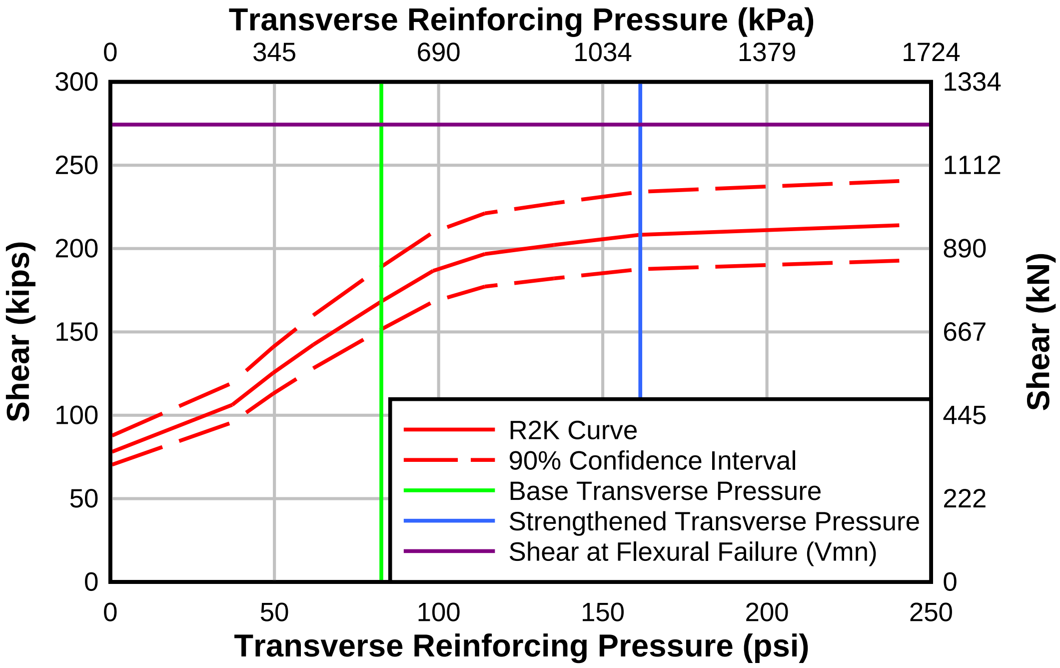

Figure 3.2: Prediction plot for specimen IT6.18.12.E1

The titanium alloy bars used in this study were round, with 1/4 in. (6.35 mm) diameter. This bar size was chosen to maintain reasonable horizontal bar spacing. Larger bar sizes result in very large spacings, in which only one or two bars cross the main diagonal crack. Smaller bars, with closer spacing, require much more labor to cut grooves and epoxy.

3.2 CONTROL SPECIMENS

In 2005, Higgins *et al.* tested a large number of unstrengthened beam specimens with the same dimensions as those used in the current study. Two of these beams had the same internal steel reinforcing as those used in this study, and are used as control specimens for the present study. The SPR specimens were labeled 1IT18 and 10T24-B4. For this study, they have been renamed SPR IT6.18* and SPR T5.24. The SPR IT6.18* specimen is marked with an asterisk since it was tested with a span of 24 ft. (7.32 m), while the IT beams used in the current study had a span of 21.8 ft. (6.64 m). The longer span results in a lower stiffness, but only a slightly lower strength. The material properties for these specimens can be found in Higgins *et al.* (2005).

3.3 SPECIMEN DETAILS

The T specimens were designed with five #11 Grade 60 tension bars in the web, and two #11 Grade 60 (#36 Grade 420) compression bars in the flange. The internal steel stirrups were #4 Grade 40 (#13 Grade 280), spaced at 24 in (610 mm). The IT specimens were designed with six #11 Grade 60 (#36 Grade 420) tension bars in the flange, and three #11 Grade 60 (#36 Grade 420) compression bars in the web. The internal steel stirrups were #4 Grade 40 (#13 Grade 280), spaced at 18 or 12 in. (457 mm or 305 mm) on center. For six of the seven specimens, titanium alloy bars were fabricated in U-shapes to act as double-leg stirrups, with 90 degree hooks at the free ends. Specimen T.5.24.12S* used offset single-leg stirrups, with hooks at both ends. The cross sections and elevations for each of these cases are shown below.

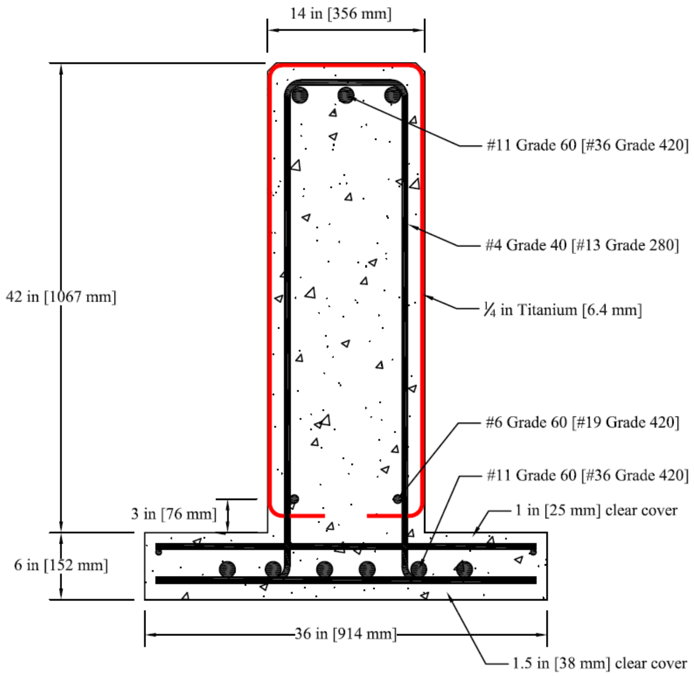

Figure 3.3: IT Specimen cross section

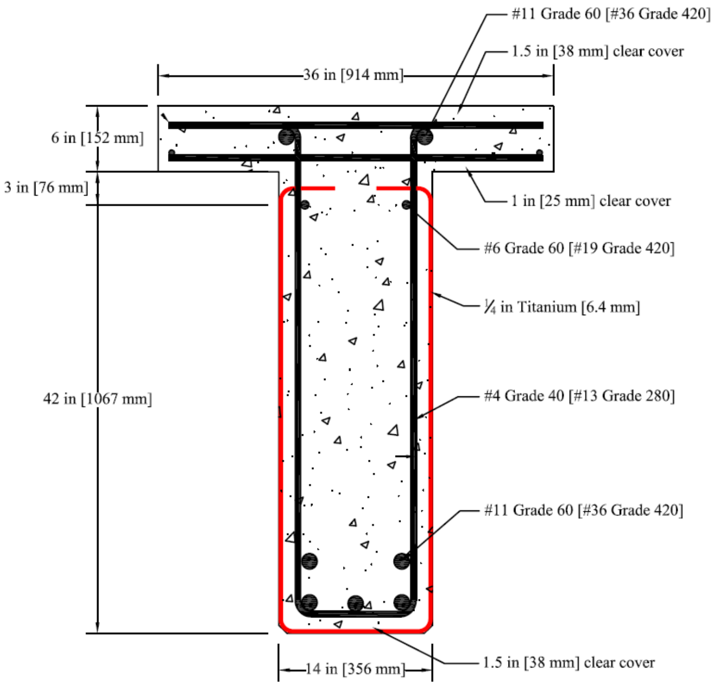

Figure 3.4: Specimen T5.24.12.E1 cross section

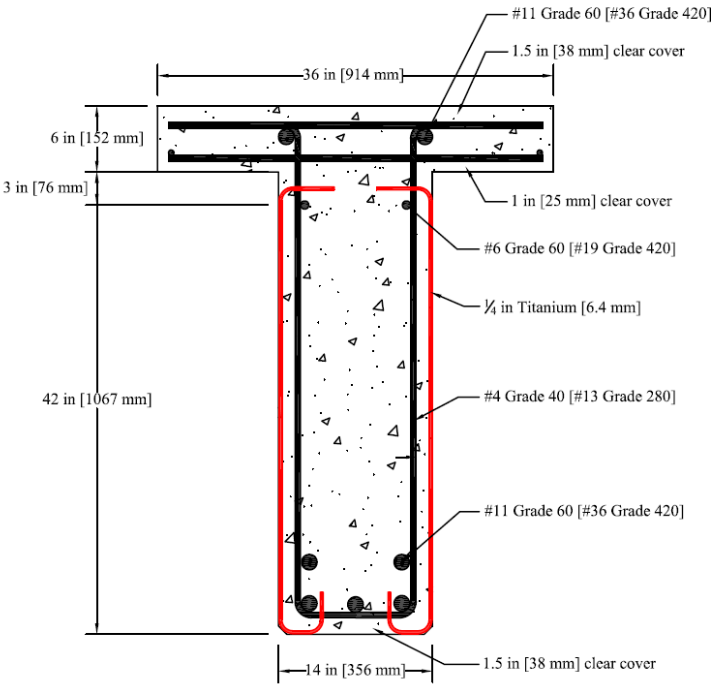

Figure 3.5: Specimen T5.24.12S.E1* cross section

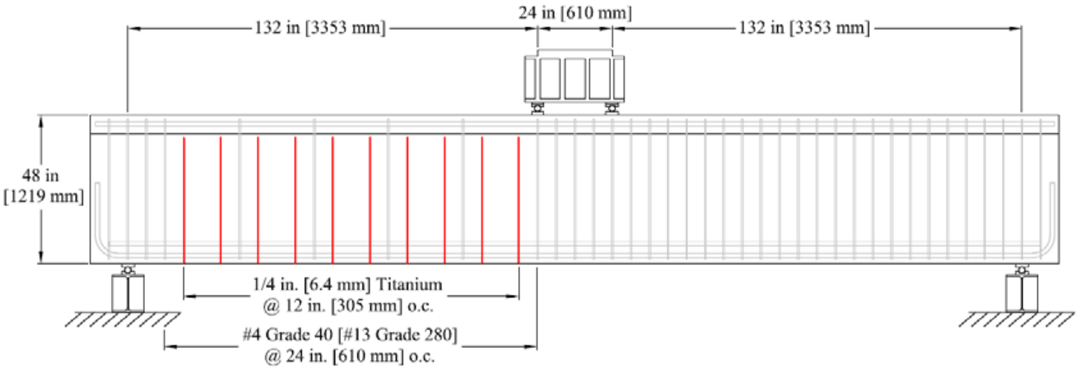

Figure 3.6: Elevation of specimen T5.24.12.E1

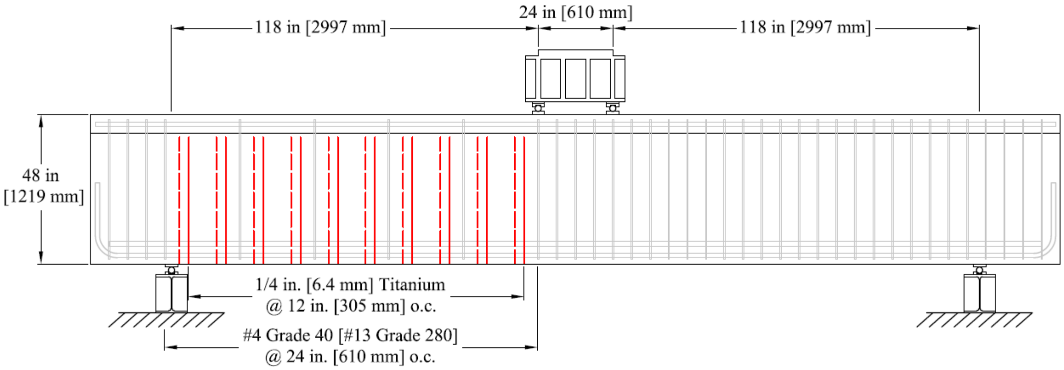

Figure 3.7: Elevation of specimen T5.24.12S.E1*

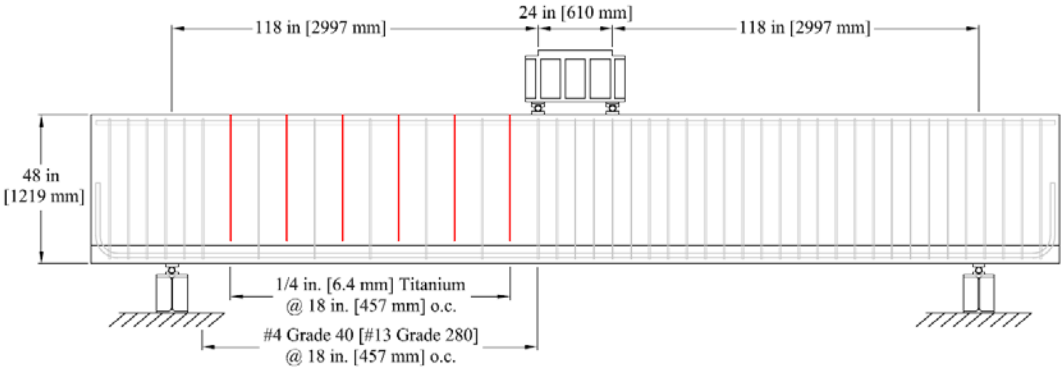

Figure 3.8: Elevation of specimen IT6.18.18.E1

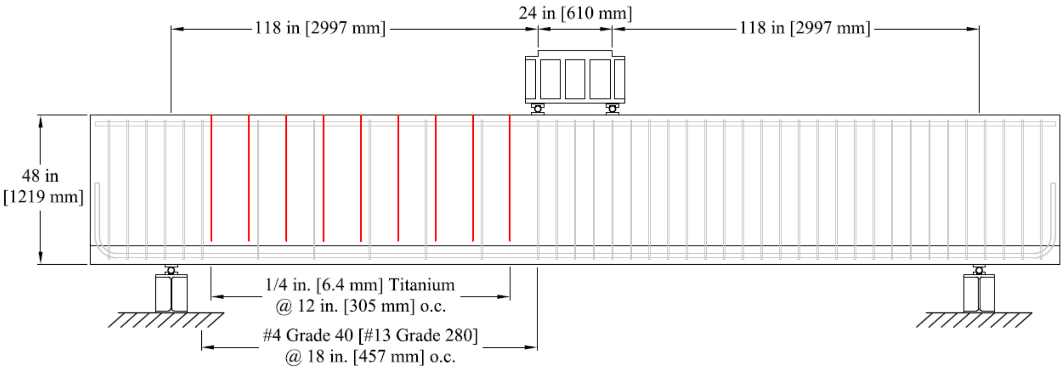

Figure 3.9: Elevation of all other IT specimens

3.4 INSTRUMENTATION

Three flexural bars were instrumented for each specimen, as shown in Figure 3.10. Each bar had three strain gages, at the following locations: Midspan, d_v away from the loading point, and at the point where a theoretical 30 degree crack would cross the flexural steel.

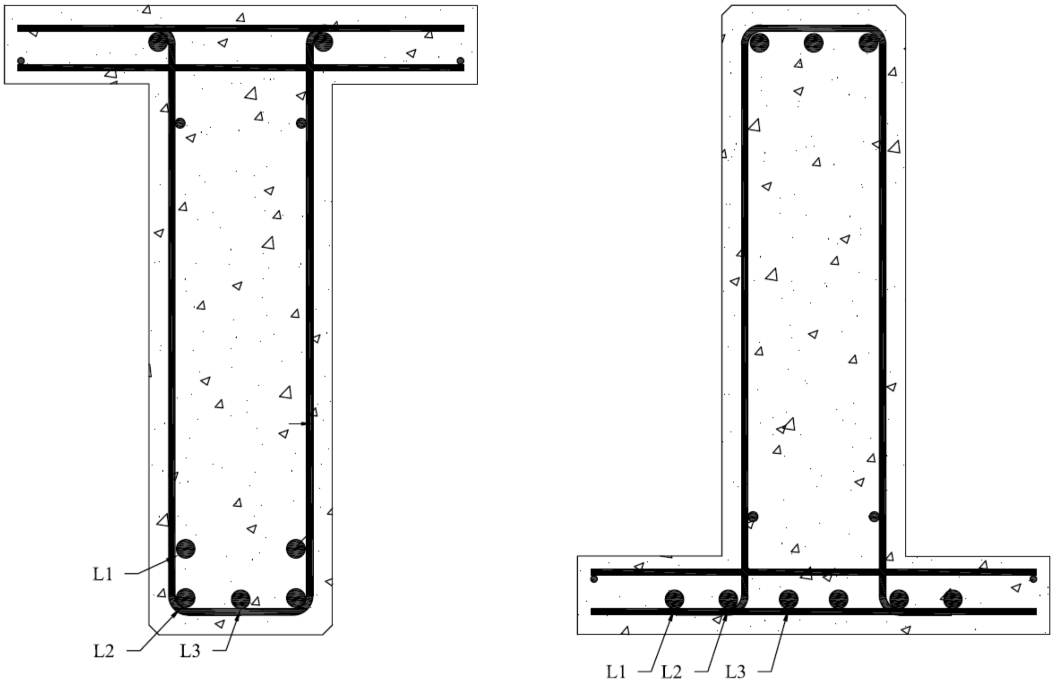

Figure 3.10: Longitudinal instrumentation

The locations of both the internal stirrup and titanium alloy bar strain gages were determined by projecting a 30° crack angle from the edge of the loading plate. Strain gages were installed at the points where this line intersected the stirrups. Strain gage locations are shown on the crack maps in Section 0. Four of the titanium alloy bars on specimen IT6.18.12.E2 were instrumented with an additional two strain gages, 3 in. (76 mm) above and below the projected crack to determine the active bond lengths.

Midspan displacement was measured using string potentiometers on the east and west sides of the beam. Support displacements were measured using linear displacement sensors placed at each end of the beam on the east and west sides. All displacements were measured relative to the strong floor. The true midspan deflection of the specimens was obtained by subtracting the average of the support displacements from the average of the overall midspan displacements.

To measure diagonal deformations, six string potentiometers were installed on the retrofitted half of the beam, as shown in Figure 3.11. When a diagonal crack formed or widened in one of the three panels, one of the potentiometers would elongate, while the other would contract. These measurements were used to determine the average vertical strain in each panel, which was then used to estimate crack widths and average stirrup strain. The T specimen instrumentation only differed from that shown in Figure 3.11 in that the horizontal spacing of the diagonal sensors was 44 in. (1118 mm) instead of 39.3 in. (998 mm).

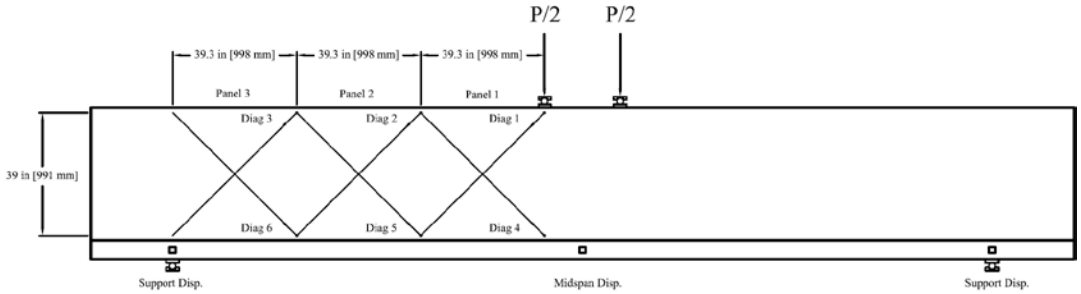

Figure 3.11: Displacement sensor locations

3.5 MATERIAL PROPERTIES

3.5.1 Concrete

The concrete was provided by a local ready-mix supplier. The concrete mix was based on the AASHTO Class A 3,000 psi (21 MPa) mixture, and was designed to have similar properties to that which was used in the 1950s. The mix was similar to that used by Higgins *et al.* (2005). The mixture proportions are given in Table 3.1. The target slump was 5.0 in. (127 mm), and additional water was added on site as necessary to achieve this slump. Actual slumps ranged from 4.5 in. to 6.0 in. (114 – 152 mm). The target 28-day strength was 3000 psi (21 MPa), but since such low strengths are difficult to achieve with modern cements, most of the specimens had strengths between 4000 psi and 5000 psi (27.6-34.5 MPa). Compressive strengths were determined using 4 in. x 8 in. (100 mm x 200 mm) cylinders. The cylinders for the first four specimens were not demolded prior to testing, so cores were drilled and tested after the failure testing of specimens T5.24.12.E1, T5.24.12S.E1*, and IT6.18.18.E1. For specimen

T5.24.12S.E1*, both cores and undemolded cylinders were tested. The results showed that the cores had 91% of the strength of the undemolded cylinders. Since cores were not taken for specimen IT6.18.12.E1, this factor was used to reduce the compressive strength measured using undemolded cylinders from 5003 psi (34.5 MPa) to 4553 psi (31.4 MPa). The compression strengths of the final three specimens were tested using properly demolded cylinders. The test day strengths for each specimen are shown in Table 3.2.

Table 3.1: Concrete Mix Proportions

Material	Quantity	
	lb/yd^3	kg/m^3
3/4" aggregate	1741	1033
Fine aggregate	1392	826
Type I cement	470	279
Water	259	154

Table 3.2: Concrete Compressive Strengths

Specimen ID	Age at Test (days)	Test Day Strength psi [MPa]
T5.24.12.E1	79	4372 [30.1]
T5.24.12S.E1*	98	4950 [34.1]
IT6.18.18.E1	85	3855 [26.6]
IT6.18.12.E1	77	4553 [31.4]
IT6.18.12.E1.FTG	188	5153 [35.5]
IT6.18.12.E2	127	3888 [26.8]
IT6.18.12.E2.FTG	136	4229 [29.2]

3.5.2 Reinforcing Steel

ASTM A615 Grade 40 (280) steel was used for the internal steel stirrups. This grade is representative of the reinforcing steel typically used in 1950's-era bridges. The other internal reinforcing steel was ASTM A615 Grade 60 (420). Coupon tests were performed to determine the steel material properties, and the results are summarized in Table 3.3.

Table 3.3: Rebar Properties

Bar	Bar Size	Grade	f_y ksi (MPa)	f_u ksi (MPa)	Elongation %
Stirrups	#4 [#13]	40 [280]	52.0 [359]	82.6 [570]	27.6
Flexural Reinforcing	#11 [#36]	60 [420]	70.7 [487]	110.3 [761]	21.7

3.5.3 **Titanium**

The titanium alloy bars used as NSM stirrups were made from the alloy Ti-6Al-4V, in which the 6 and 4 represent percentages of aluminum and vanadium respectively. The nominal bar diameter was 1/4 in. (6.4 mm). The bars were fabricated with a custom deformation pattern similar to a coil threaded bolt, slightly reducing the diameter at deformation locations. The deformations were cut out of the bar. The bars were deformed along their entire length. The average area of the bars used with the E1 epoxy was 0.047 in^2 (30.3 mm^2), and the average area of the bars used with the E2 epoxy was 0.045 in^2 (29.0 mm^2). These areas were calculated by weighing bars of known lengths, and dividing by the unit weight of the titanium alloy, which is 276.6 pcf (4.43 g/cc). The elastic modulus of the titanium was taken as 15,500 ksi (106.9 GPa).

The titanium alloy bars were deformed and bent to shape by the manufacturer. The out-to-out width of the stirrups was nominally 13.875 in. (352 mm). All bends were made about a 2 in. (51 mm) pin. The tail extensions past the hooks were 3.75 in. (95 mm). Figure 3.12 (a) shows a typical titanium alloy stirrup prior to installation. For T5.24.12S*, the titanium alloy stirrups were cut in half. The section that was cut was then heated and bent about a 2 in. pin, with a tail extension of approximately 2.25 in. (57 mm). Figure 3.12 (b) shows one of the single-leg stirrups used on specimen T5.24.12S*. A detailed view of the hooked end is provided in Figure 3.12 (c). Prior to installation, the deformations on the inside of the hooks were ground off, in order to prevent stress concentrations.

Coupon tests were conducted to determine the material properties of the titanium alloy bars. For the E1 specimens the titanium had a yield strength of 141.0 ksi (972 MPa), an ultimate strength of 151.1 ksi (1042 MPa), and an elongation of 12.6%. For the E2 specimens the titanium had a yield strength of 140.0 ksi (965 MPa), an ultimate strength of 150.6 ksi (1038 MPa), and an elongation of 7.6%.

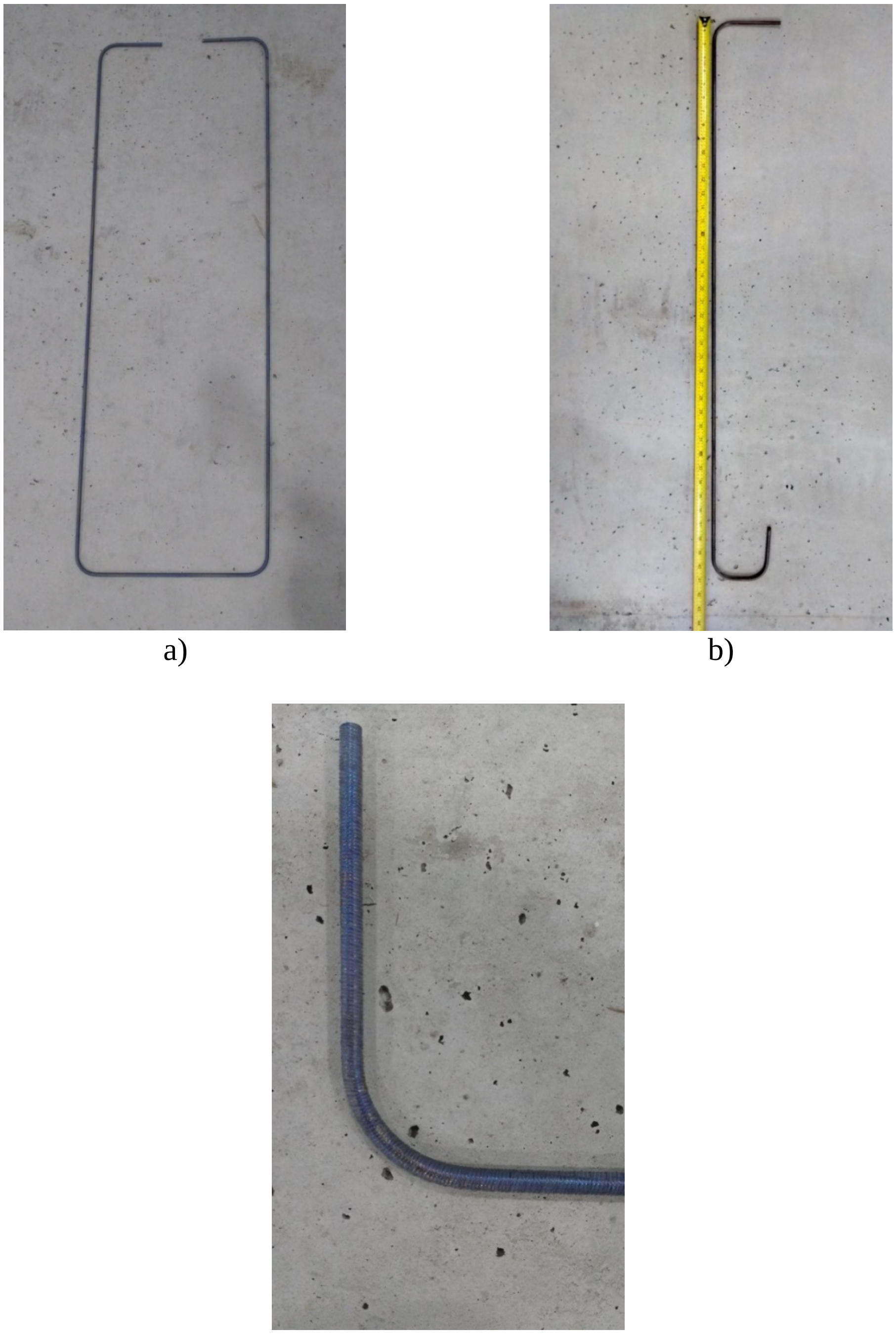

a) b)

c)

Figure 3.12: Titanium alloy bar (a) Double leg titanium stirrup, (b) Single leg titanium stirrup, (c) Hook detail

3.5.4 **Epoxy**

Two different kinds of epoxy were used in this study. In previous research at OSU, Goebel (2011) tested three commonly used epoxies in both strength and freeze-thaw loading conditions.

The strongest and most durable of these epoxies, BASF MasterEmaco ADH 1420 (formerly BASF Concresive 1420) (E1) was selected for the first five tests. Since the epoxy was not a limiting factor in any of these tests, the weakest epoxy tested by Goebel, Unitex Pro-Poxy 400 (E2), was used for the final two tests. Both epoxies were tested in strength and fatigue/freeze thaw loading conditions. The manufacturer reported properties for each epoxy are given in Table 3.4

Table 3.4: Epoxy Properties

Epoxy Type	Tensile Strength psi [MPa]	Elongation at Break %	Compressive Strength psi [MPa]	Compressive Modulus ksi [GPa]	Bond Strength psi [MPa]
E1: BASF MasterEmaco ADH 1420	4000 [27.6]	1.0	12,500 [86.2]	450 [3.06]	2000 [13.8]
E2: Unitex Pro-Poxy 400	Not reported	1.3	10,000 [68.95]	270 [1.86]	2800 [19.3]

3.6 SPECIMEN CONSTRUCTION

The specimens were constructed in the O.H. Hinsdale Wave Research Laboratory at Oregon State University. Formwork was built for the first two beams, and was reused for the remaining beams. Rebar cages were tied using standard rebar ties, and spacers were placed on the bars in order to provide the required cover. The concrete was placed in multiple lifts, with each lift being mechanically vibrated before the next lift was placed. After initial set, the concrete was covered with burlap and plastic, and kept moist for 7 days. Typical cage construction and concrete pouring procedures are shown in Figure 3.13 and Figure 3.14

Figure 3.13: Cage construction process (test section on left)


Figure 3.14: Concrete placement process

3.7 RETROFITTING METHODOLOGY

The first step in strengthening the beams required cutting grooves and drilling end anchor holes for the NSM titanium alloy bars. The grooves were intentionally placed so as to avoid intersecting the internal stirrups. The groove width was taken as $1.5d_b$, the minimum recommended value in ACI 440. This resulted in 3/8 in. (9.5 mm) wide grooves.

Groove depth varied for the initial specimens to identify the effect of groove depth on behavior. Specimen T5.24.12.E1 was tested with groove depths of 7/16 in. (11.1 mm) on the west side, and 9/16 in. (14.3 mm) on the east side. Although this specimen did not fail in diagonal-tension, the side with the deeper grooves exhibited noticeably fewer chevron cracks in the epoxy. Specimen IT6.18.18.E1 was tested with 3/8 in. (9.5 mm) deep grooves on both sides. This specimen developed significant chevron cracking in the epoxy, and at failure the epoxy cover along with adjacent concrete spalled off of two titanium alloy bars. This was the only E1 beam to exhibit this behavior. For all of the remaining specimens, a groove depth of 1/2 in. (13 mm) was used. This deeper groove depth also allowed for an increased tolerance in the out-to-out width of the titanium alloy stirrups. The grooves were wet cut in a single pass. The groove cutting process is shown in Figure 3.15.

Figure 3.15: Groove cutting process with aluminum saw guide

At the ends of the grooves near the deck soffit, holes were drilled to allow anchorage of the titanium alloy bar hooked ends. The end anchor holes were 3/8 in. (9.5 mm) diameter. This was selected based on recommendations for post-installed epoxy anchors. After the holes and grooves were cut, they were cleaned using an air hose and wire brushes. The titanium alloy bars were cleaned using soap and water, and allowed to dry. Duct tape was placed along the grooves to allow clean surfaces at the edges. The grooves and holes were filled 3/4 full with epoxy, and the bars were pushed into place. The surface was trowled smooth to cover the bars. The epoxy was allowed to cure for a minimum of seven days. Beams retrofitted during cold weather were covered by a tent and heated in order to achieve manufacturer recommended curing conditions. The titanium installation process is shown in Figure 3.16.


Figure 3.16: Titanium installation process

3.8 TESTING METHODOLOGY

After construction and curing, the specimens were tested to assess their structural performance. The specimens were tested in four-point bending using a 500-kip (2224 kN) hydraulic actuator. Load was applied to a spreader beam with a 24 in. (610 mm) span, centered above the midpoint of the beam. The load was transferred from the spreader beam to the specimen using 2 in. (51 mm) diameter rollers resting on 4 in. (102 mm) wide bearing plates. The specimens were supported on 4 in. (102 mm) wide bearing plates resting on 2 in. (51 mm) diameter rollers. The test setup is shown in Figure 3.17.

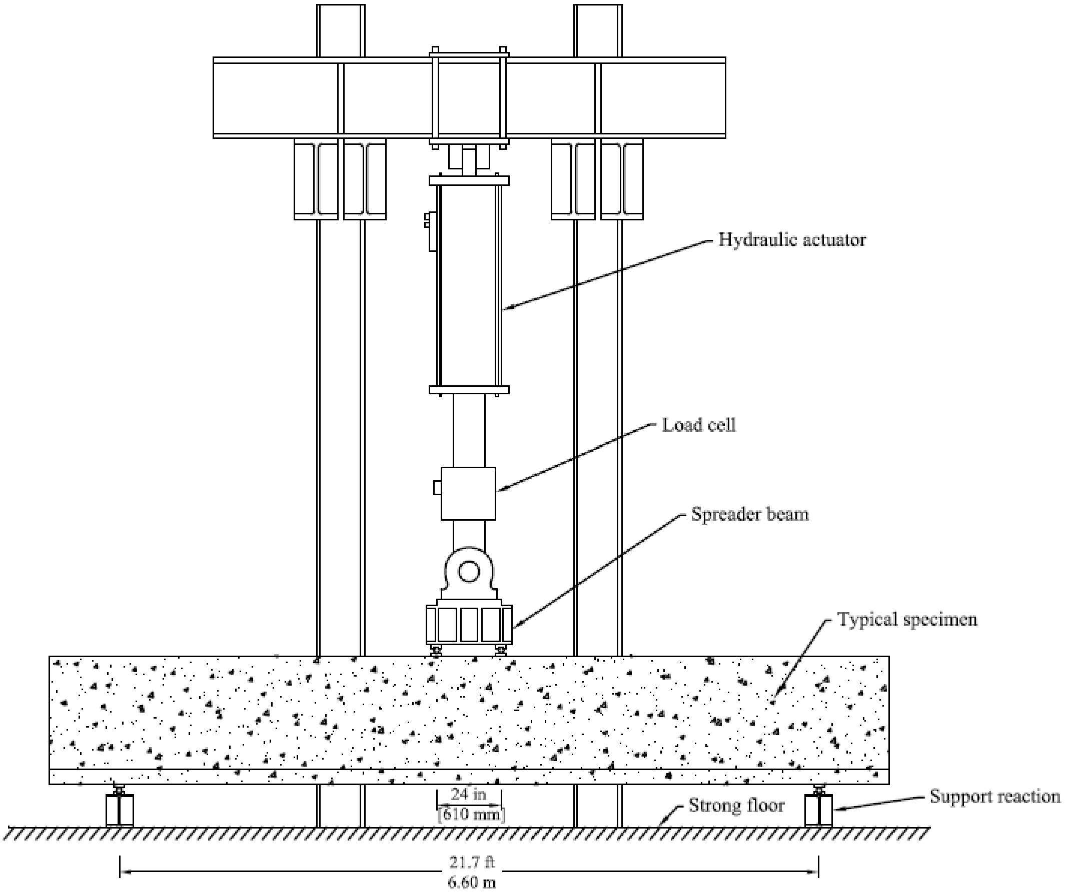

Figure 3.17: Schematic of test setup

T specimens, with the exception of T5.24.12S*, were tested with a 24 ft. (7.32 m) span. Specimen T5.24.12S* was initially tested at 24 ft. (7.32 m), but the supports were moved in to 21.67 ft. (6.61 m) in order to force diagonal-tension failure. All IT specimens were tested with a 21.67 ft. (6.61 m) span.

The actuator was controlled by displacement feedback, and was applied at a rate of 0.003 in./s (0.076 mm/s) for the first four tests, and 0.0083 in./s (0.21 mm/s) for the final three tests. The load was applied in 50 kip (222 kN) increments. After each increment, the load was reduced by 50 kips (222 kN), and cracks were marked. The load was then removed entirely before beginning the next load increment.

3.9 FATIGUE TEST PROCEDURE

To assess the durability of the NSM titanium strengthening approach, specimens IT6.18.12.E1.FTG and IT6.18.12.E2.FTG were subjected to fatigue loading. The fatigue loading protocol was based on prior work by Higgins *et al.* (2007) who used field instrumentation to measure stirrup stresses in existing bridges at diagonal crack locations. To simulate 50 years of damage in a laboratory setting, an equivalent stress range was calculated using Miner’s Rule below, and a stress of range of 13.8 ksi (95.1 MPa) for 2,000,000 cycles was found to cause equivalent damage.

$$SR_{eqv} = \sqrt[3]{\sum \frac{n_i}{N_{tot}} SR_i^3} \qquad \textbf{[4.2]}$$

where SR_i = the ith stress range, n_i = the number of cycles for the ith stress range, and N_{tot} = the total number of cycles for all stress ranges [Miner 1945].

Also using Miner's Rule, Johnson (2011) adjusted these results for a smaller actuator, and ran 2,400,000 cycles at 13.0 ksi (89.6 MPa). The current study follows this loading program, and the loads were designed to cause stresses of approximately 13.0 ksi (89.6 MPa) in the internal stirrups.

Prior to beginning fatigue tests, the beams were precracked to a load of 210 kip (934 kN) under three point bending. A schematic of the freezer and fatigue setup is shown in Figure 3.18, while Figure 3.19 shows one of the specimens in the freezer/fatigue setup. Both specimens were subjected to 2.4 million cycles, at a rate of 2.0 Hz. The load range was 60 kip to 110 kip (267-489 kN). For specimen IT6.18.12.E1.FTG, this corresponded to 13.2%- 24.3% of the failure load. For specimen IT6.18.12.E2.FTG, this corresponded to 16.1%- 29.6% of the failure load.

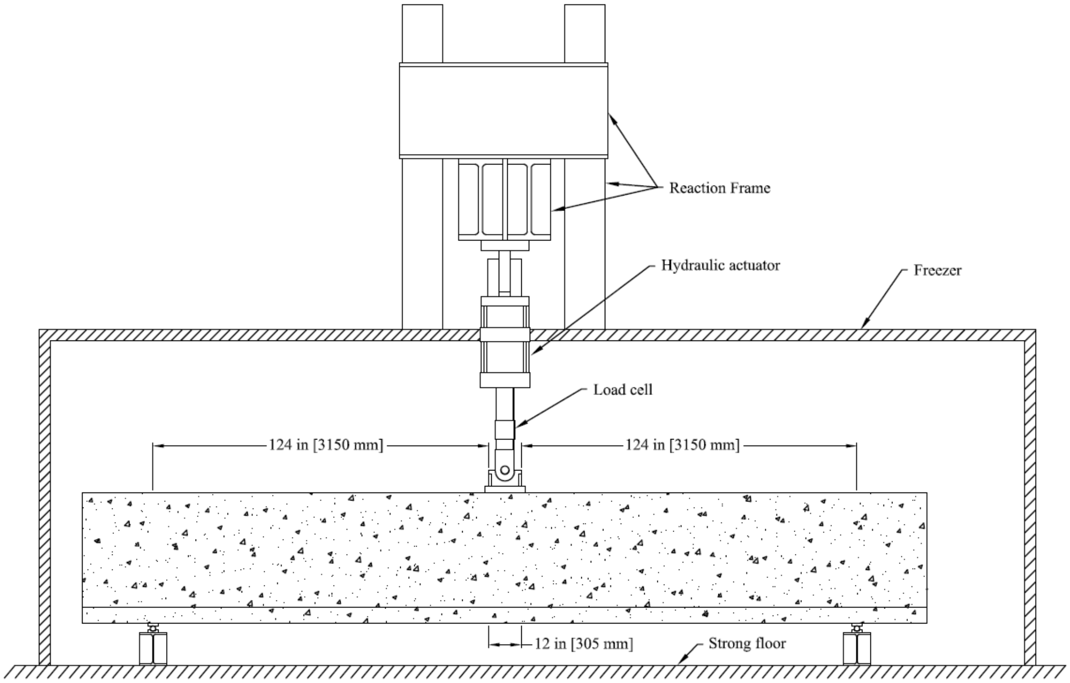

Figure 3.18: Freezer and fatigue schematic


Figure 3.19: Specimen in freezer

The fatigue tests were stopped periodically and static tests were conducted to assess any changes in response over the fatigue loading regime. Midspan, support, and diagonal sensors were applied to the specimen, and the beam was loaded to 210 kip (934 kN) at a rate of 4 kip/s (17.8 kN/s). Table 3.5 lists the cycle count at which these tests were done for each specimen.

Table 3.5: Fatigue Testing Intervals

Test number	IT6.18.12.E1.FTG	IT6.18.12.E2.FTG
1	0	0
2	213,000	207,000
3	424,000	510,000
4	721,000	833,000
5	1,083,000	1,155,000
6	1,578,000	1,800,000
7	2,400,000	2,400,000

3.10 FREEZE-THAW TEST PROCEDURE

While being fatigued, specimens IT6.18.12.E1.FTG and IT6.18.12.E2.FTG were also subjected to approximately 120 freeze-thaw cycles. The ambient temperature varied from approximately -6°C to 8°C, with ramp times of 30 minutes and soak times of 1 hour. The beam was surface saturated with water once per day (every eight cycles) by spraying it during a thaw cycle. This was used to represent in-situ conditions, in which moisture is applied to the surface, rather than being fully saturated. Type T thermocouples were used to monitor the air temperature, and the concrete temperature at depths of 0.5 in. (13 mm), 1.5 in. (38 mm), and 3.0 in. (76 mm) from the surface. They were monitored regularly to ensure the concrete core stayed near 0°C. Typical thermocouple readings are shown in Figure 3.20. Two or three sensors are shown for each depth. As expected, decreasing temperature variation was observed with increasing sensor depth. The 0.5 in. sensors (the blue lines) were installed at the depth of the NSM grooves, and clearly indicate that freeze-thaw cycling is taking place at this depth.

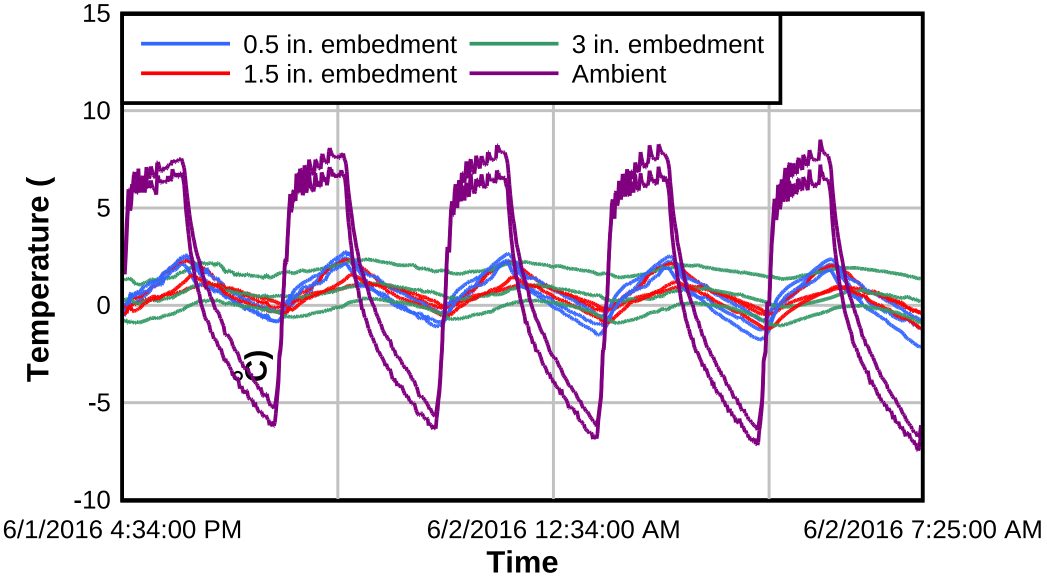

Figure 3.20: Freezer temperature data

This test program was based on previous research by Higgins *et al.* (2009), who used heat transfer analysis to calculate freeze-thaw cycles at the concrete surface based on air temperature records from four locations in Oregon. The results are listed in Table 3.6.

Table 3.6: Freeze-Thaw Cycles for Representative Regions in Oregon [Higgins *et al.* 2009]

Location	Freeze-Thaw Cycles	Period of Temperature Record (Years)	Freeze-Thaw Frequency (Cycles/Year)
Tillamook (Coast)	8	11	0.73
Stayton (Valley)	45	12	3.75
Tumalo Ridge (Central)	243	6	40.5
Sage Hen (Eastern)	868	22	39.5

Both wet and dry freezing cycles were included in this table. Goebel (2011), however, showed that dry freeze thaw cycles do not cause significant deterioration in the concrete or epoxy. The Valley and Central regions were selected for further study, to determine the percentage of freeze-thaw cycles that occurred under wet conditions, which would lead to deterioration. Ten years of historical weather data were obtained for Salem, OR and Redmond, OR (Weather Underground, 2006-2015). A freeze-thaw cycle was counted if the following conditions were met: The daily high was above 32°F (0°C), the daily low was below 32°F (0°C), and the average daily temperature was between 28°F and 36°F (-2.2°C and 2.2°C). The final condition is necessary, since the core temperature of the concrete must be low if freeze-thaw cycles at the surface are to occur. The concrete was considered to be wet if at least 0.1 in. (2.5 mm) of precipitation was recorded over the preceding 48 hours. This showed that 12.9% of freeze-thaw cycles in Redmond had moisture present, while 27.7% of freeze-thaw cycles in Salem had moisture present. Thus 120 wet freeze-thaw cycles were used in this test program, which represent approximately 23 years in the central region and 116 years in the valley region.

3.11 BOND TESTS

Three bond tests were conducted for each epoxy in order to determine if the 1/4 in. (6.4 mm) titanium alloy bars can be relied on to reach their yield strength. The test setup and results from these tests are reported in Vavra (2016).

4.0 EXPERIMENTAL RESULTS

The experimental results for each specimen are reported in this section. Table 4.1 lists the applied shear (V_{Act}) and midspan displacement at failure, as well as the calculated dead load shear acting on the failed section (V_{DL}). The dead load contribution to shear was calculated as the weight of the concrete in between midspan and the main diagonal crack.

Table 4.1: Summary of Test Results

Specimen	V_{Act} kip [kN]	V_{DL} kip [kN]	V_{tot} kip [kN]	Midspan Displacement in. (mm)
T5.24.12.E1	195.0 [867.4]	0.0 [0.0]	195.0 [867.4]	2.18 [55.4]
T5.24.12S.E1*	197.0 [876.3]	3.5 [15.7]	200.5 [892]	1.03 [26.2]
IT6.18.18.E1	215.2 [957.3]	5.2 [23.1]	220.4 [980.4]	0.96 [24.4]
IT6.18.12.E1	223.5 [994.2]	4.3 [19.2]	227.8 [1013.4]	0.92 [23.4]
IT6.18.12.E1.FTG	226.3 [1006.6]	4.9 [21.8]	231.2 [1028.4]	0.90 [22.9]
IT6.18.12.E2	203.9 [907.0]	4.3 [19.1]	208.2 [926.1]	0.91 [23.1]
IT6.18.12.E2.FTG	185.7 [826.0]	3.8 [16.7]	189.5 [842.7]	0.77 [19.6]

4.1 GLOBAL BEHAVIOR

The load-displacement curves for each specimen are shown in Figures 4.1 and 4.2. Control specimens taken from Higgins *et al.* (2005) are shown as well. For all specimens, a significant increase in capacity was observed, while the deflection at failure remained similar. Specimen T5.24.12.E1 failed in flexure, and was thus able to reach a midspan deflection of 2.18 in. (55.4 mm), more than doubling the deflection of the control specimen, which failed in diagonal-tension. Specimen IT6.18.12.E2.FTG failed at a relatively lower load and deflection due to the damage done to the epoxy in the fatigue and freeze-thaw test.

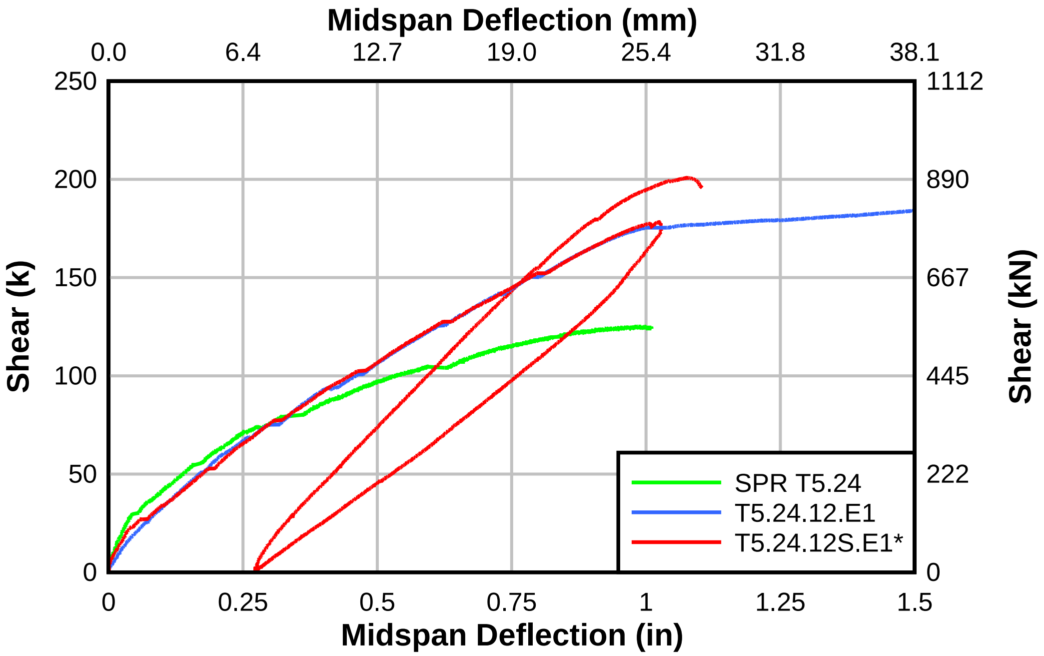

Figure 4.1: T beam load-deflection backbone curves

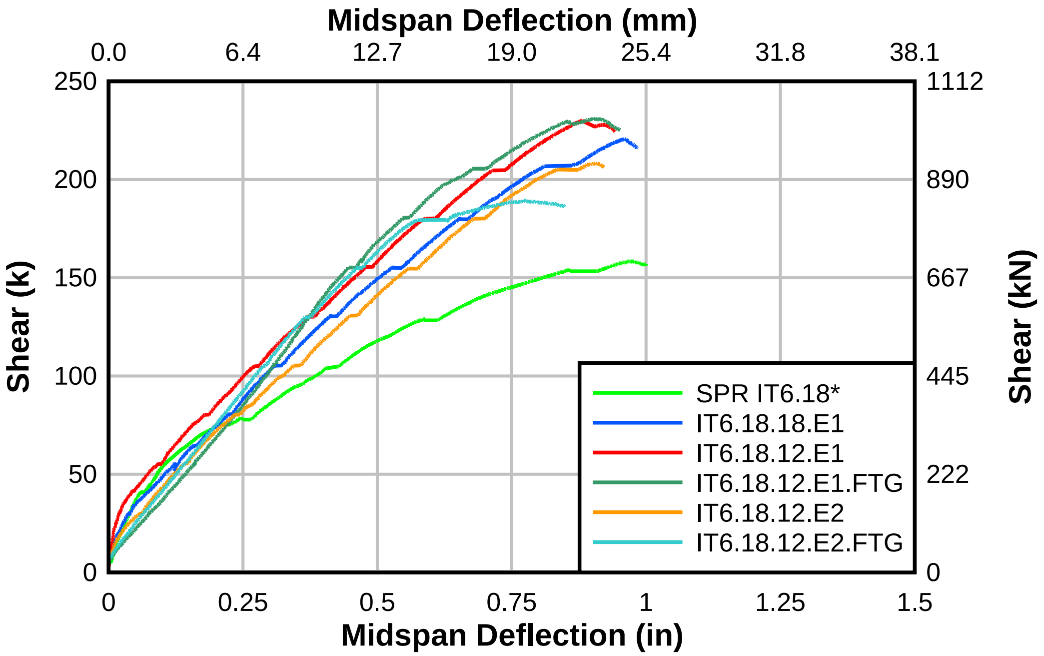

Figure 4.2: IT beam load-deflection backbone curves

In the following sections, detailed descriptions of each test are presented.

4.2 **SPECIMEN T5.24.12.E1**

Specimen T6.18.12.E1 did not achieve a diagonal-tension failure. Plastic deformation initiated at a load of 353 kip (1570 kN), corresponding to a midspan deflection of 1.06 in. (26.9 mm). The specimen softened but continued to carry additional load, until it failed at a load of 390 kip (1735 kN), with a deflection of 2.18 in. (55.4 mm). The failure mode was crushing of the compression block. Significant chevron cracking in the epoxy was observed on the back side of the beam with 7/16 in. (11.1 mm) deep grooves, while the front side with 9/16 in. (14.3 mm) deep grooves displayed better crack control, with more feathering of the cracks in the concrete around the NSM titanium alloy bars.

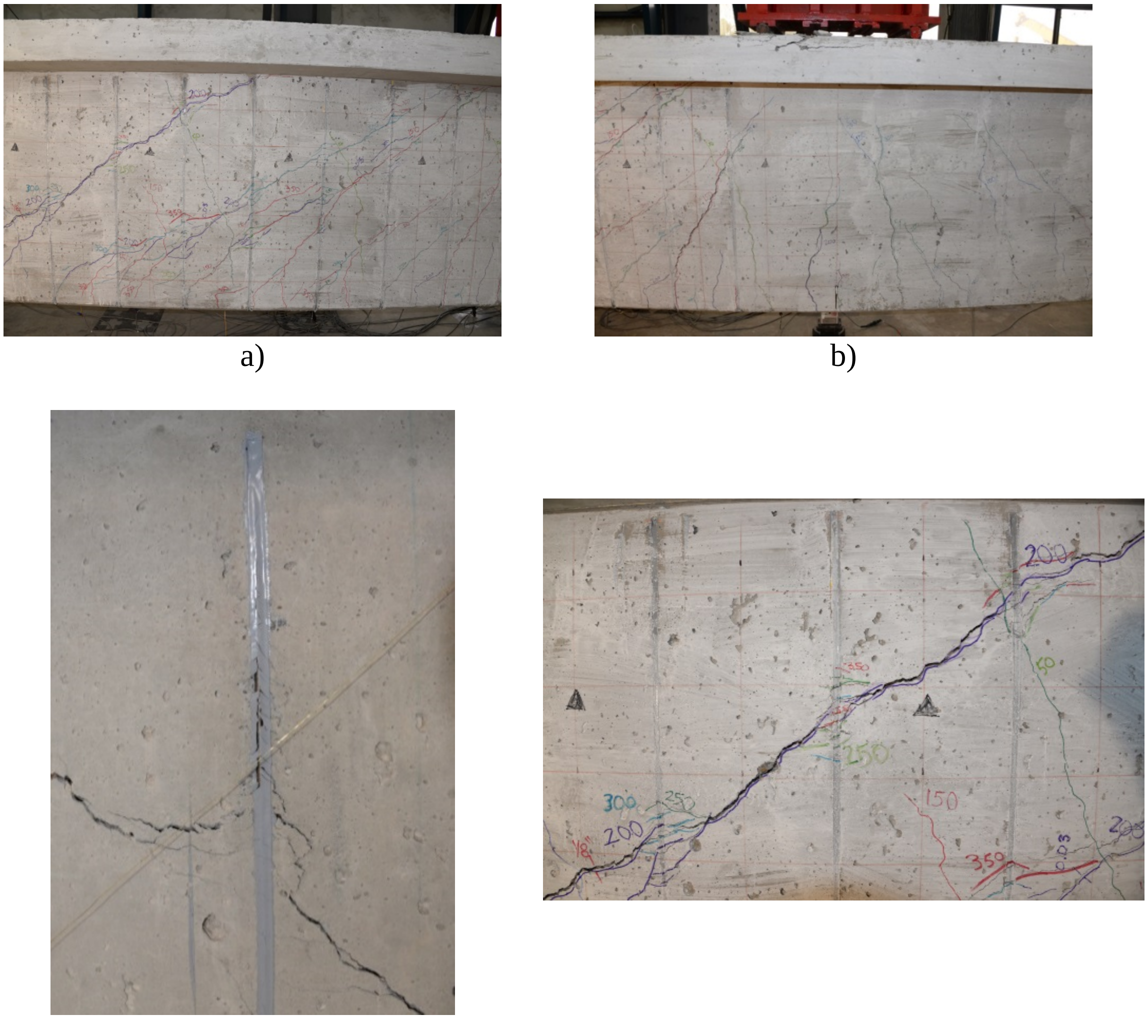

a) b)

c) d)

Figure 4.3: Specimen T5.24.12.E1 at failure(a) Diagonal cracking, (b) Flexural failure, (c) Chevron cracking, (d) Crack feathering

4.3 SPECIMEN T5.24.12S.E1*

Specimen T5.24.12S.E1* only differed from specimen T6.18.12.E1 in that it was retrofitted with offset single-leg stirrups instead of double-leg stirrups. The single leg stirrups did not have any quantifiable effect on the stiffness or strength of the specimen. The load-displacement curve was nearly identical to specimen T5.24.12.E1, and it began to show plastic deformation at a load of 350 kip (1557 kN), corresponding to a deflection of 1.03 in (26.2 mm). At this point, the decision was made to reduce the span from 288 in. (7315 mm) to 260 in. (6604 mm) to induce a diagonal-tension failure. A shear-compression failure was achieved at a load of 395 kip (1757 kN) and a deflection of 1.08 in. (27.4 mm). The main diagonal crack crossed three (3) NSM titanium alloy bars, labeled T4 – T6, all of which ruptured at the diagonal crack at failure. The crack passed through the plane of the hooks of stirrup T7, but the hooks did not pull out. The 180 degree hooks, unique to the single leg stirrups, pried the web apart on the tension side, causing significant cracking not observed in any of the other tests.

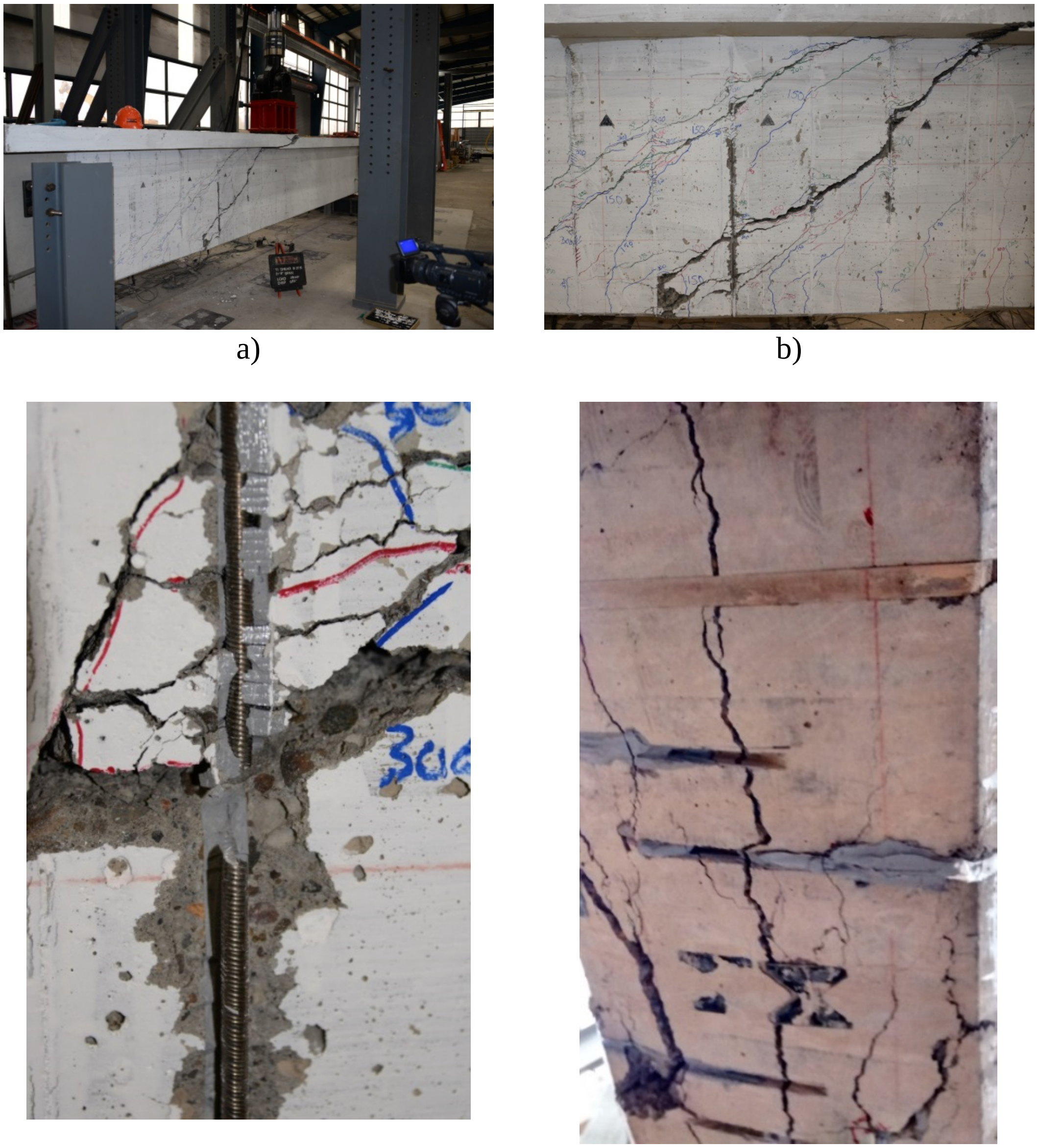

a) b)

c) d)

Figure 4.4: Specimen T5.24.12S.E1* at failure (a) Specimen at failure, (b) Detail of main diagonal crack, (c) T4 ruptured at failure, (d) Web cracking viewed from beneath the specimen

4.4 SPECIMEN IT6.18.18.E1

Specimen IT6.18.18.E1 failed at an applied load of 432 kip (1922 kN), with a midspan deflection of 0.96 in. (24.4 mm). The failure mode was shear-compression. Shortly after reaching peak load, the main diagonal crack significantly widened, and the steel and titanium alloy stirrups ruptured over the crack. The crack crossed four (4) NSM titanium alloy bars, labeled T1 – T4, beginning from the bottom of the crack. After peak load the hooks on both sides of stirrup T1 pulled out about 0.5 in. (12.7mm), as the main crack passed directly through the plane of the hooks. Stirrup T2 was debonded along most of its length at peak load. After peak load, the epoxy cover and surrounding concrete were lost along the length of the stirrup, after which one of the stirrup legs ruptured, while the hook on the other side pulled out about 0.5 in. (12.7 mm). Stirrups T3 and T4 also lost their epoxy cover and surrounding concrete after peak load, before rupturing across the main crack on both sides. Specimen IT6.18.18.E1 was the only specimen for which hook pullout or significant epoxy cover loss were observed, likely because the NSM groove depth was only 3/8 in. (9.5 mm).

a) b)

c) d)

Figure 4.5: Specimen IT6.18.18.E1 at failure (a) Specimen at failure, (b) Detail of main diagonal crack, (c) T3 ruptured at failure, (d) T2 chevron cracking

4.5 **SPECIMEN IT6.18.12.E1**

Specimen IT6.18.12.E1 failed at an applied load of 447 kip (1988 kN), corresponding to a midspan deflection of 0.92 in. (23.4 mm). The failure mode was shear-compression. On the previous load step, the specimen reached a load of 451 kip (2006 kN), at a deflection of 0.88 in. (22.4 mm). On the final load step, the specimen failed due to the increased deflection before it reached this load level. Had the loading been continued from the previous load step, it likely would have failed near 457 kip (2033 kN). Two diagonal cracks opened significantly at failure. No major crack propagated through the bottom flange. The cracks crossed six (6) NSM titanium alloy bars, labeled T2 – T7. The crack passed directly through the plane of the hooks on stirrup T2, causing one of the hooks to pull out slightly. Stirrups T3 and T4 ruptured over the higher crack, while stirrups T5 and T6 ruptured over the lower crack. Stirrup T7, located 7.0 in. (178 mm) away from edge of the loading point, did not rupture or lose epoxy cover. After peak load, minor epoxy cover loss was observed. Significant feathering of the cracks was observed where the diagonal crack crossed the titanium alloy bars. Chevron cracking was not observed, likely since the epoxy cover was sufficiently large.

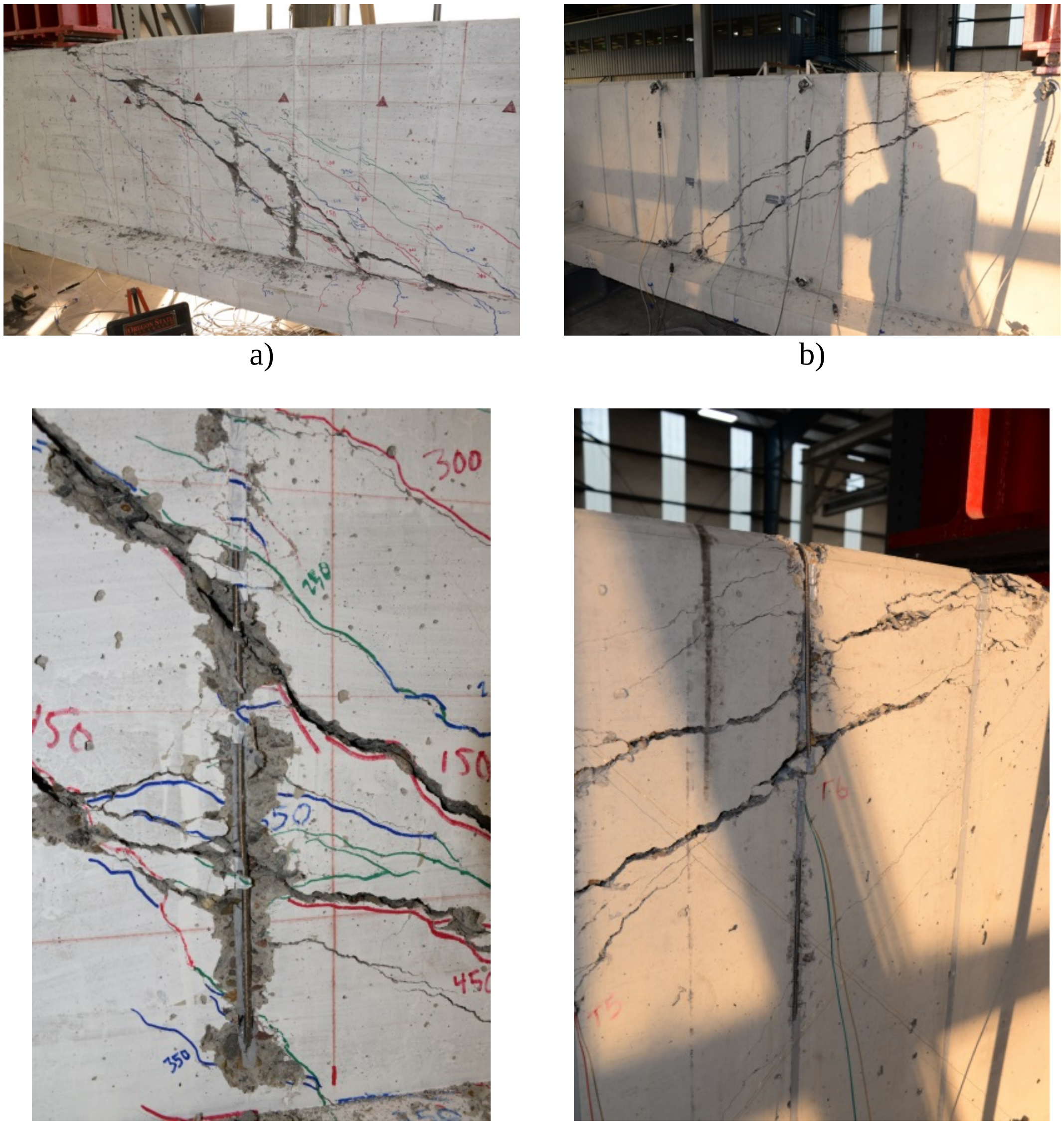

a) b)

c) d)

Figure 4.6: Specimen IT6.18.12.E1 at failure (a) Diagonal crack on front side, (b) Diagonal crack on back side, (c) T3 ruptured at failure, (d) T6 on back side

4.6 SPECIMEN IT6.18.12.E1.FTG

Prior to failure testing, specimen IT6.18.12.E1.FTG was loaded to 210 kips and then subjected to 2,400,000 cycles of fatigue and 120 freeze-thaw cycles. Efflorescence and cracking of the epoxy near the diagonal cracks was observed, as well as some minor raveling along the diagonal cracks. Figure 4.7 shows the damage resulting from the fatigue and freeze thaw cycles. The cracks marked in green marker developed during the initial loading to 210 kip (934 kN), while the other cracking developed during the cyclic testing.

a) b)

Figure 4.7: Specimen IT6.18.12.E1.FTG freeze-thaw and fatigue damage (a) Efflorescence and cracking at titanium alloy bar hook, (b) Efflorescence and cracking of the epoxy

The specimen failed at an applied load of 453 kip (2013 kN), corresponding to a midspan deflection of 0.90 in. (22.9 mm). These numbers correspond nearly exactly with specimen IT6.18.12.E1, suggesting that the fatigue and freeze thaw cycles had no measureable effect on the strength or stiffness of the specimen. It should be noted, however, that since this specimen had a higher concrete compressive strength, any decreases in strength may have been offset by the higher concrete strength. R2K predicts a difference in shear carrying capacity of 9.2 kip (40.9 kN), while the experimental results only differed by 3.4 kip (15.1 kN). This means that the freeze-thaw and fatigue cycles may have caused the beam to lose up to 5.8 kip (25.8 kN) of shear carrying capacity.

After peak load, titanium alloy stirrups T3, T4, and T5 ruptured over the main crack on both sides. Significant damage due to creep occurred after peak load, since the actuator was not immediately shut off. Figure 4.8 (a) and (b) show the damage at the end of the test. Figure 4.8 (c) is a screenshot from a video, and shows the damage immediately after the crack widened. Like the previous tests, good crack control and significant feathering were observed. Figure 4.8 (d) shows crack feathering at titanium alloy bar T6. No significant epoxy cover loss was observed prior to failure, and none of the titanium alloy bar hooks pulled out.

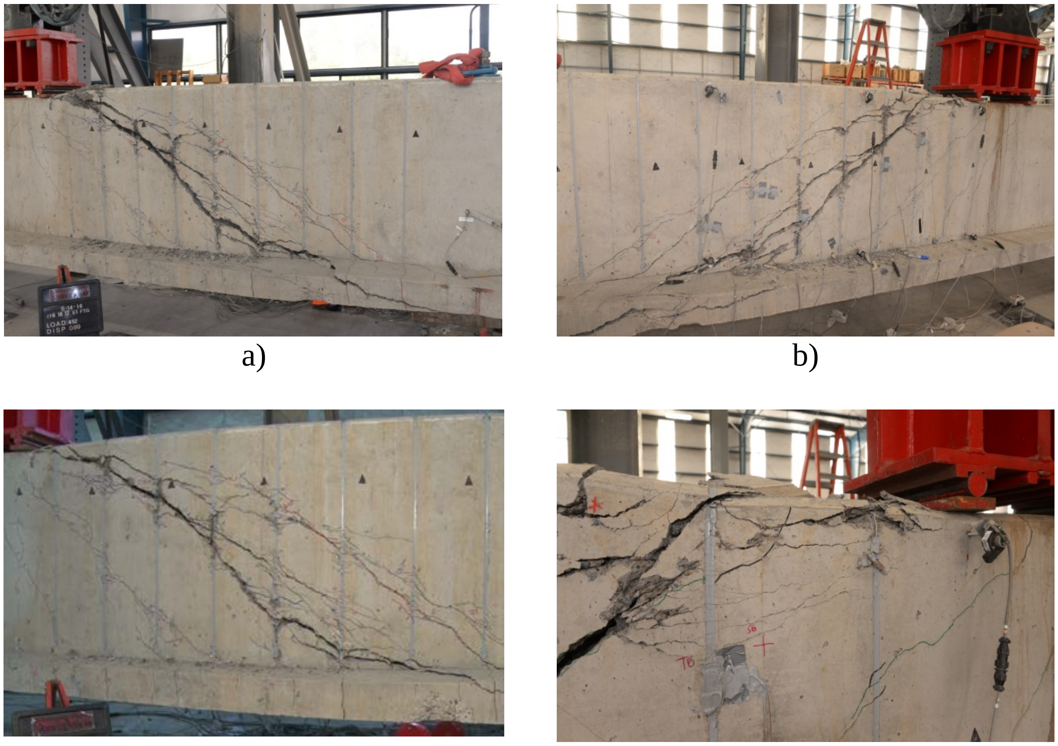

a) b)

c) d)

Figure 4.8: Specimen IT6.18.12.E1.FTG at failure (a) Front side diagonal crack at end of test, (b) Back side diagonal crack at end of test, (c) Video screenshot of front diagonal crack immediately after failure, (d) Crack feathering at titanium alloy bar T6

4.7 **SPECIMEN IT6.18.12.E2**

Specimen IT6.18.12.E2 had the same steel and titanium alloy reinforcement as specimen IT6.18.12.E1, but epoxy E2 was used when strengthening it. This specimen failed at an applied load of 408 kip (1815 kN), corresponding to a midspan deflection of 0.91 in. (23.1 mm). Stirrups T3 and T5 ruptured on the back side after peak load. None of the other stirrups ruptured. Stirrup T2 debonded over most of its length on the front side at a load of approximately 300 kip (1334 kN). Stirrup T4 debonded along most of its length below the crack on the front side at a load of approximately 350 kip (1557 kN). No hook pullout was observed at failure.

This specimen showed a decrease in strength and stiffness when compared with specimen IT6.18.12.E1. It developed fewer large cracks, with wider spacings between them. Where crossing a titanium alloy bar, the cracks tended to feather at steeper angles, since this epoxy requires a longer active bond length. The longer active bond lengths allow for wider cracks at lower loads. However, the decrease in strength is also largely due to the weaker concrete and smaller titanium alloy stirrups used for the E2 specimen. R2K predicts a difference in shear carrying capacity of 12.5 kip (55.6 kN), accounting for 60-70% of the strength decrease.

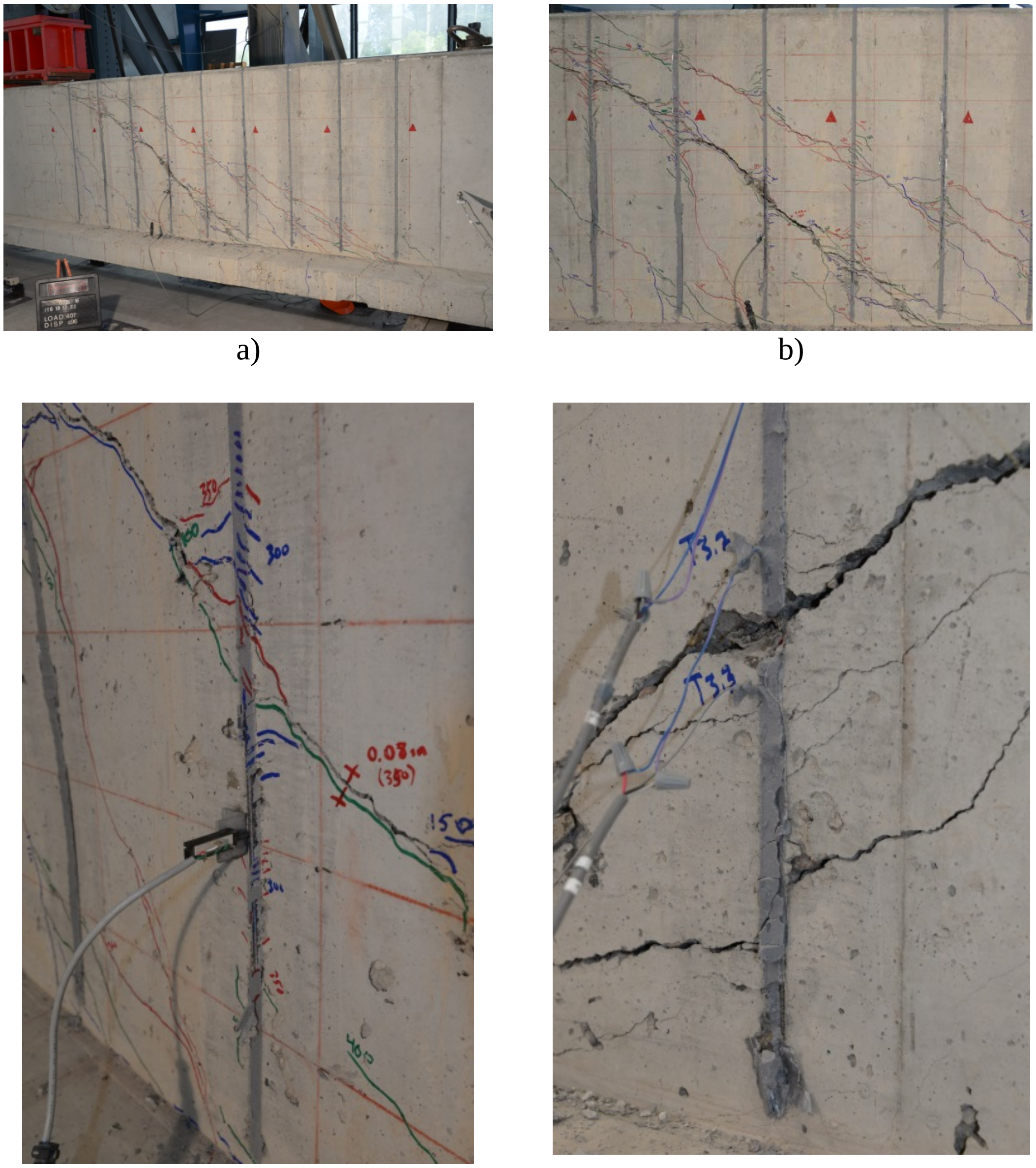

a) b)

c) d)

Figure 4.9: Specimen IT6.18.12.E2 at failure (a) Specimen at failure, (b) Detail of diagonal crack, (c) T4 feathering and epoxy cracking, (d) T3 ruptured at failure

4.8 SPECIMEN IT6.18.12.E2.FTG

Prior to failure testing, specimen IT6.18.12.E2.FTG was loaded to 210 kips and then subjected to 2,400,000 cycles of fatigue and 120 freeze-thaw cycles. This was the same test program used for specimen IT6.18.12.E1.FTG, and the resulting damage was similar. However, this specimen developed significantly more crack feathering at the titanium alloy bar locations during the fatigue and freeze thaw cycles, as illustrated in Figure 4.10. The black lines indicate cracks that developed during the fatigue and freeze-thaw testing.

a) b)

Figure 4.10: Specimen IT6.18.12.E2.FTG freeze-thaw and fatigue damage (a) Epoxy cracking, (b) Crack feathering

This specimen failed at an applied load of 371 kip (1650 kN), corresponding to a midspan deflection of 0.77 in. This marked a significant decrease in strength when compared with the other specimens, meaning the fatigue and freeze thaw cycles had a significant effect on the strength of this specimen. On the front side of the beam, stirrups T4 and T6 fully debonded at failure. Stirrup T4 ruptured. Stirrup T5 did not rupture or debond, even though it crossed a very wide crack. This indicates poor bond along the crack, which allows for very long active bond lengths. On the back side, stirrups T3, T4, and T5 all ruptured. No hook pullout was observed. This specimen developed significantly less crack feathering than the other specimens, likely due to reduced bond between the concrete and epoxy.

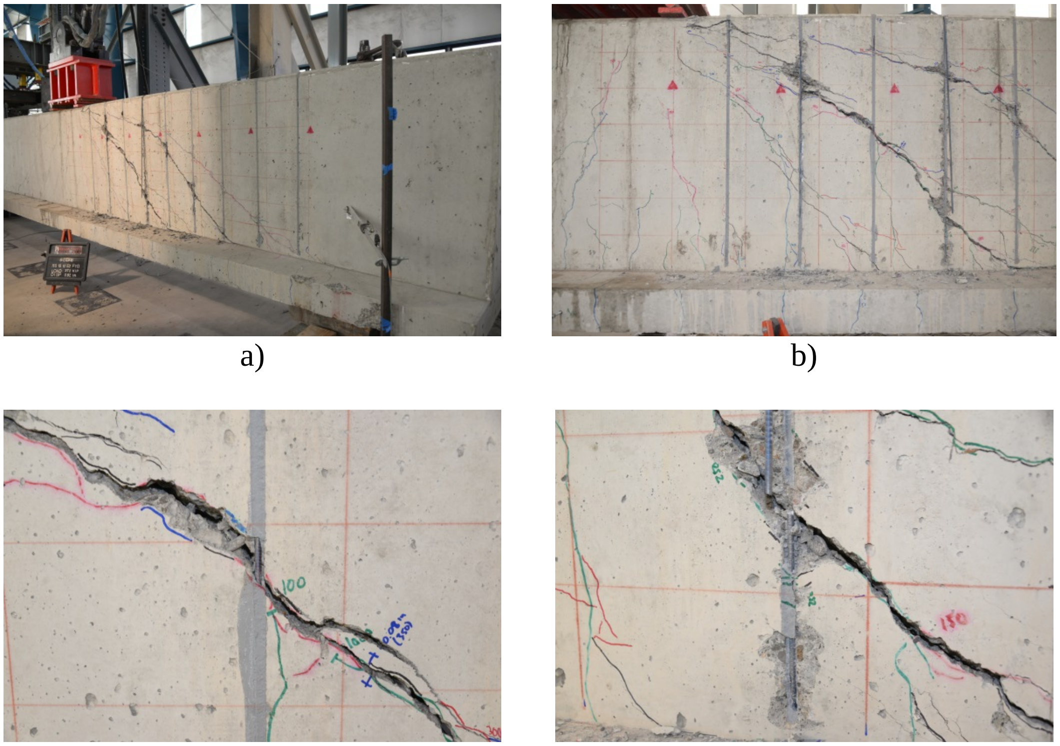

a) b)

c) d)

Figure 4.11: Specimen IT6.18.12.E2.FTG at failure (a) Specimen at failure, (b) Detail of diagonal crack, (c) No crack feathering, debonding, or rupture at T5 over main diagonal crack, (d) T4 ruptured at failure

4.9 SPECIMEN STRENGTH INCREASES

R2K was used to predict the capacity of each specimen ($V_{R2K\ Base}$) before application of the NSM titanium alloy bars. These predicted strengths were not adjusted using the bias calculated by Higgins *et al.* (2005). This was done so an independent bias could be calculated for the specimens in the present experimental program. The increase in shear capacity was calculated as the observed capacity including dead load (V_{exp}) minus the R2K base capacity. Table 4.2 shows the strength increases for each specimen over the unstrengthened R2K predicted base specimen.

Table 4.2: Strength Increases

Specimen	$V_{R2K\ Base}$ kip [kN]	V_{exp} kip [kN]	V_{incr} kip [kN]	V_{incr} %
T5.24.12.E1	134.5 [598.3]	195.0 [867.4]	60.5* [269.1]*	45.0
T5.24.12S.E1*	136.7 [608.1]	200.5 [892]	63.8 [283.9]	46.7
IT6.18.18.E1	157.3 [699.7]	220.4 [980.4]	63.1 [280.7]	40.1
IT6.18.12.E1	164.9 [733.5]	227.8 [1013.4]	62.9 [279.9]	38.2
IT6.18.12.E1.FTG	171.9 [764.6]	231.2 [1028.4]	59.3 [263.8]	34.5
IT6.18.12.E2	155.7 [692.6]	208.2 [926.1]	52.5 [233.5]	33.7
IT6.18.12.E2.FTG	160.6 [714.4]	189.5 [842.9]	28.9 [128.6]	18.0

* Indicates minimum contribution for flexural failure

4.10 CRACK MAPS AND INSTRUMENTATION

Crack maps of each specimen were created, and are shown in Figure 4.12 through Figure 4.18. These figures illustrate the extensive crack feathering exhibited by most of the specimens. Specimens IT6.18.18.E1 and IT6.18.12.E2.FTG were exceptions, as less cracking was observed with additional debonding of the epoxy along the bars.

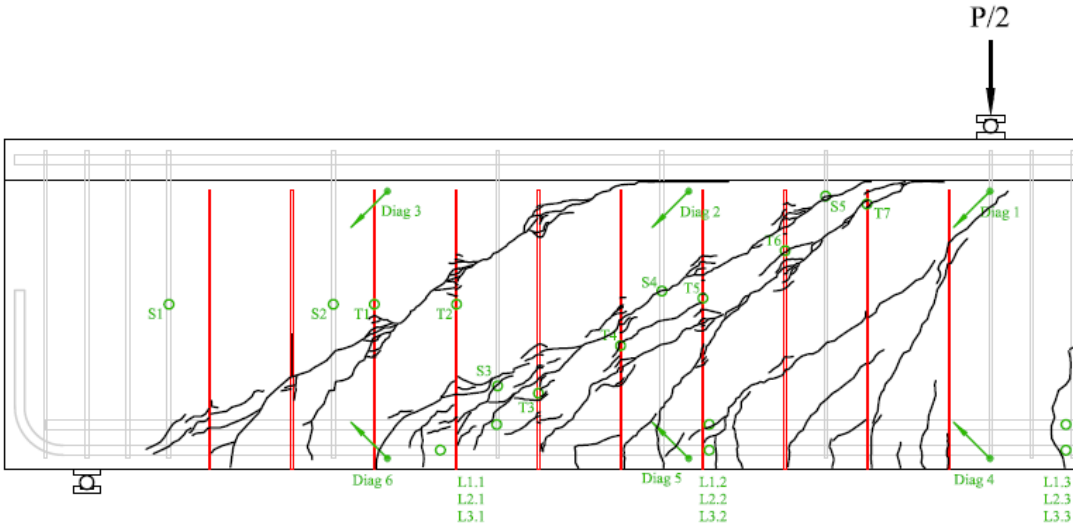

Figure 4.12: Specimen T5.24.12.E1 crack map

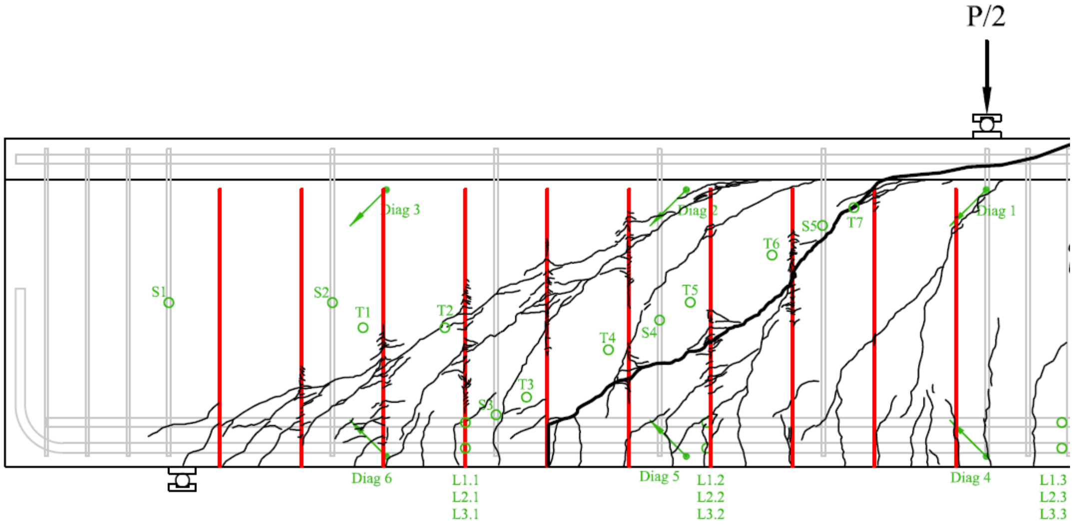

Figure 4.13: Specimen T5.24.12S.E1* crack map

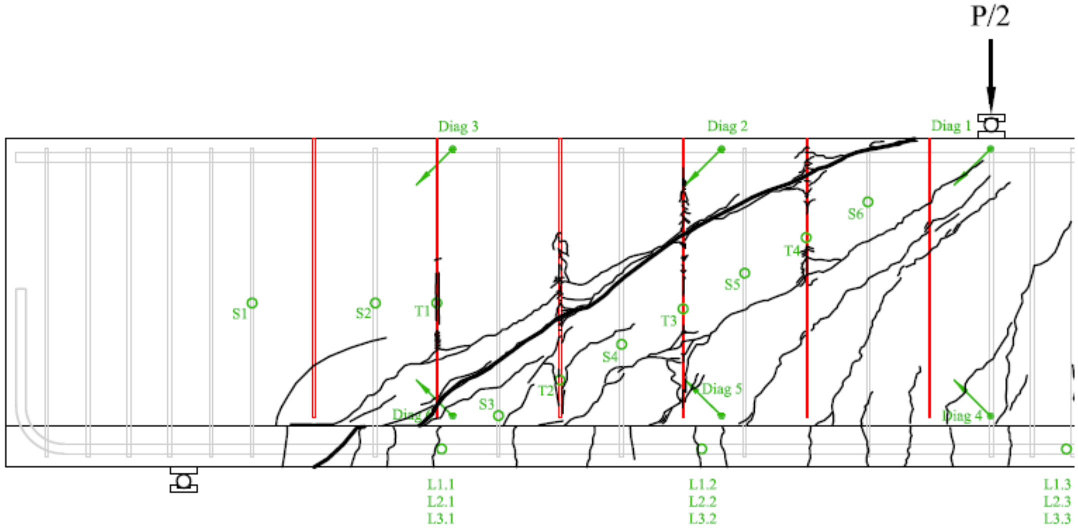

Figure 4.14: Specimen IT6.18.18.E1 crack map

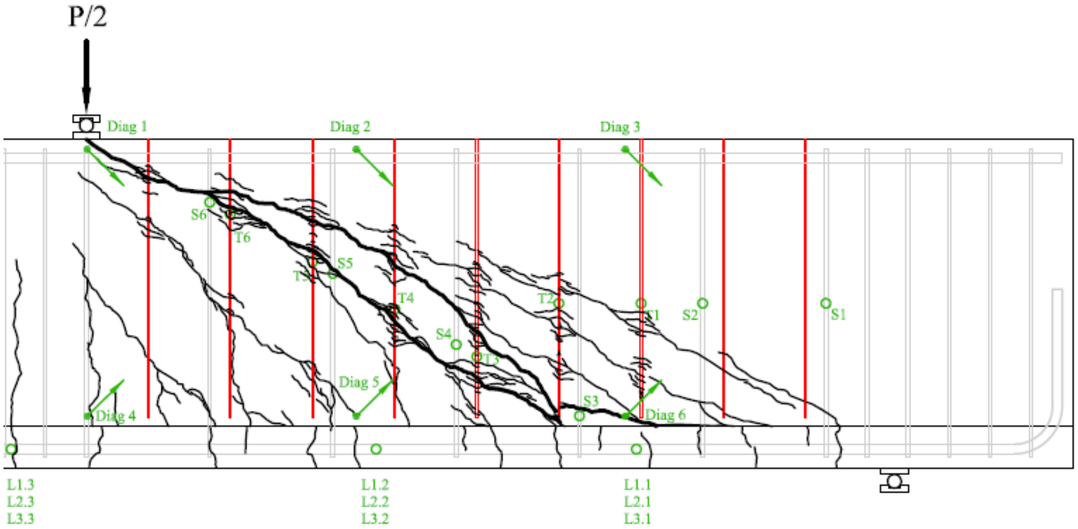

Figure 4.15: Specimen IT6.18.12.E1 crack map

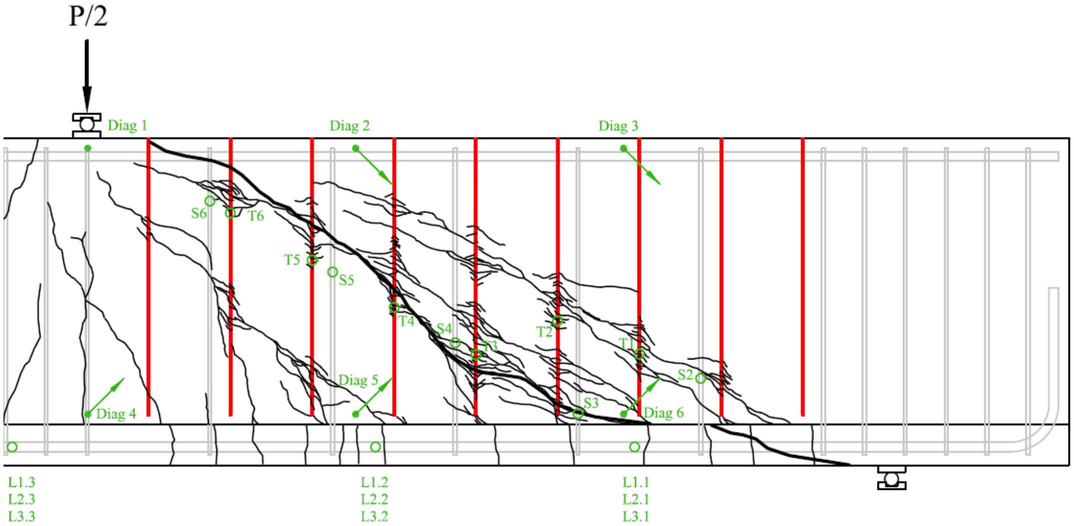

Figure 4.16: Specimen IT6.18.12.E1.FTG crack map

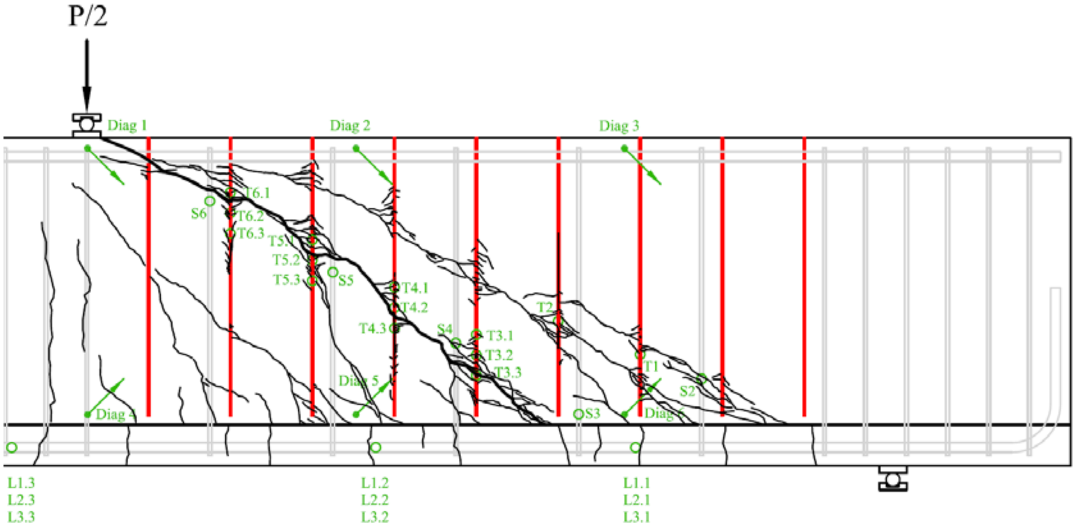

Figure 4.17: Specimen IT6.18.12.E2 crack map

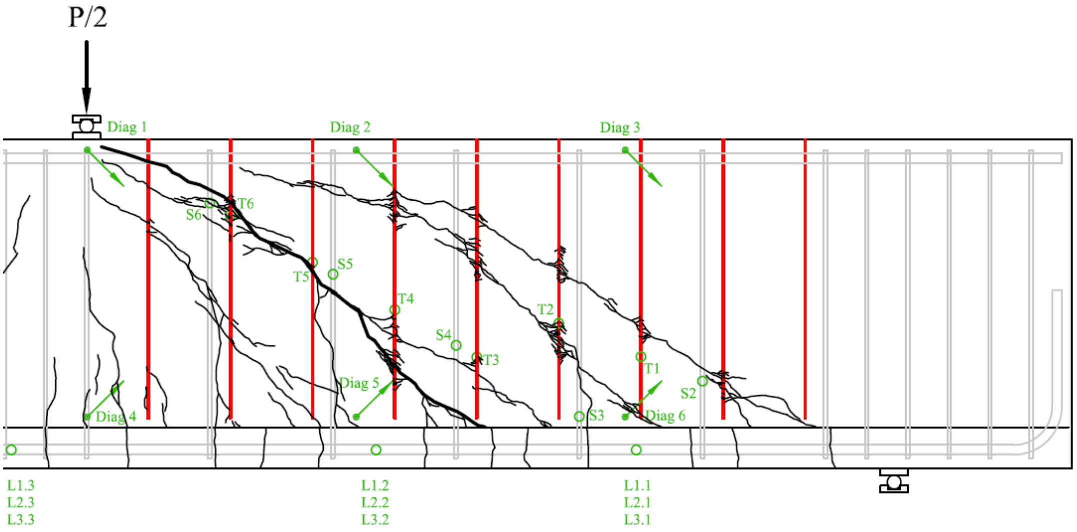

Figure 4.18: Specimen IT6.18.12.E2.FTG crack map

4.11 STRAINS IN STEEL AND TITANIUM ALLOY BARS

Strain gages were used to monitor the strains in the steel and titanium alloy bars. Because the crack locations could not be precisely known in advance, many of the strain gages were located away from the cracks and thus the measured strains are smaller than those that would be observed at the intersection of cracks. The results from undamaged strain gages within 7 in. (178 mm) of a crack are summarized in Tables 4.3 and 4.4 as the applied shear on the specimen when the strain was observed to reach the yield strain threshold. The locations of the strain gages on the specimens are shown on the crack maps in the preceding section.

Table 4.3: Internal Stirrup Strain Gage Results

Specimen	Strain gage	Dist. from crack in. [mm]	Shear at yield kip [kN]
T5.24.12.E1	S3	0.0 [0]	140 [623]
	S4	0.0 [0]	121 [538]
	S5	0.0 [0]	140 [623]
T5.24.12S.E1*	S3	2.1 [53]	191 [850]
	S4	5.0 [127]	180 [801]
	S5	1.9 [48]	116 [516]
IT6.18.18.E1	No working strain gages near crack		
IT6.18.12.E1	S3	0.9 [23]	178 [792]
	S4	3.3 [84]	154 [685]
	S5	0.5 [13]	105 [467]
IT6.18.12.E1.FTG	S2	2.3 [58]	110 [489]
	S3	0.0 [0]	128 [569]
	S4	5.0 [127]	110 [489]
	S5	4.5 [114]	No yield
	S6	2.2 [56]	202 [898]
IT6.18.12.E2	S3	6.6 [168]	172 [765]
	S4	2.9 [74]	83 [369]
	S5	2.7 [69]	140 [623]
IT6.18.12.E2	S2	1.8 [46]	105 [467]
	S3	6 [152]	No yield
	S4	3.3 [84]	179 [796]

Table 4.4: Titanium Strain Gage Results

Specimen	Strain gage	Dist. from crack in. [mm]	Shear at yield kip [kN]
T5.24.12.E1	T5	3.7 [94]	94 [418]
T5.24.12S.E1*	T2	0.2 [5]	161 [716]
IT6.18.18.E1	No working strain gages near crack		
IT6.18.12.E1	T1	4.0 [102]	207 [921]
	T3	3.1 [79]	205 [912]
	T6	0.0 [0]	112 [498]
IT6.18.12.E1.FTG	No working strain gages near crack		
IT6.18.12.E2	T1	1.6 [41]	204 [907]
	T2	0.7 [18]	190 [845]
	T3.1	3.0 [76]	201 [894]
	T3.2	0.0 [0]	169 [752]
	T3.3	3.0 [76]	205 [912]
	T4.1	0.5 [13]	No yield
	T4.2	2.5 [64]	147 [654]
	T4.3	5.5 [140]	169 [752]
	T5.2	3.4 [86]	200 [890]
	T5.3	6.5 [165]	203 [903]
	T6.1	0.7 [18]	207 [921]
	T6.2	3.7 [94]	203 [903]
	T6.3	6.7 [170]	205 [912]
IT6.18.18.E2.FTG	T1	6.0 [152]	No yield
	T2	3.5 [89]	186 [827]
	T4	3.3 [84]	184 [818]
	T5	6.5 [165]	180 [801]
	T6	0.0 [0]	78 [347]

As seen in these results, the titanium alloy bars tended to reach their yield strain after the internal steel stirrups reached yield. In addition, many of the TiABs near the controlling diagonal crack achieved yield before or at ultimate. This indicates that yielding of the TiABs may be used for predicting shear strength.

4.12 VERTICAL STRAIN ANALYSIS

4.12.1 Panel Strain

In order to supplement the strain gage results, average vertical strains were calculated over the three panels instrumented with diagonal sensors. The diagonal strains were converted into vertical and horizontal strains using Mohr's circle, following the procedure reported by Dawson *et al.* (2008). The backbone curves for the measured vertical strains in each specimen are shown in Figures 4.19-4.27. The vertical displacement was obtained by multiplying the vertical strain by the vertical dimension of the diagonal sensors. The vertical deformations in each panel at peak load are listed in Table 4.5. The vertical strains from the panel closest to the support (panel 3) were ignored, since they were typically small by comparison to panel zone 2 and 1. Note that for the fatigue/freeze thaw specimens, the panel shear and vertical deformations only include cracking that developed during the failure test.

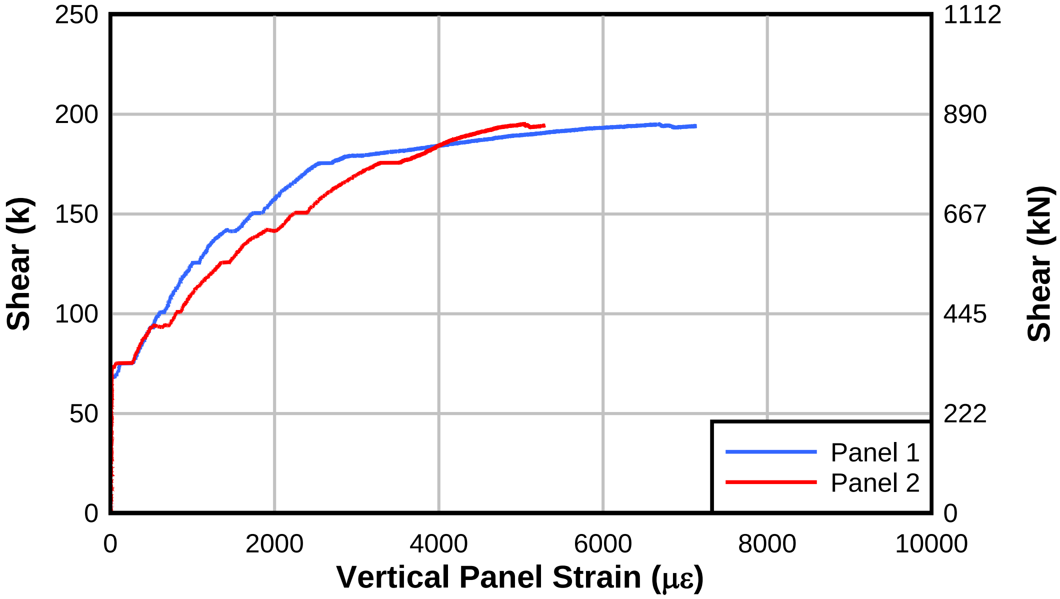

Figure 4.19: Specimen T5.24.12.E1 average panel vertical strain

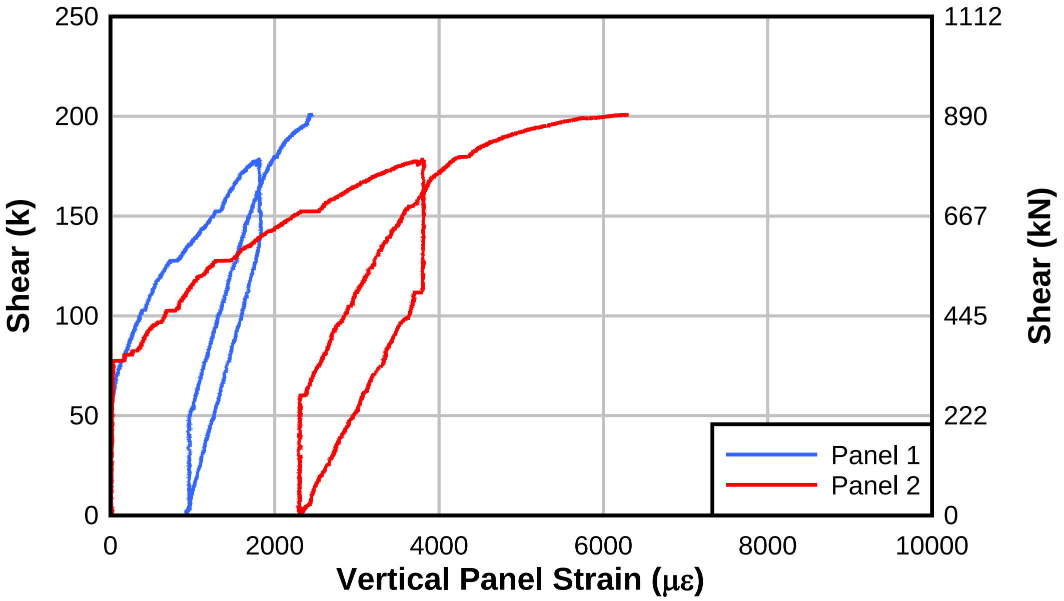

Figure 4.20: Specimen T5.24.12S.E1* average panel vertical strain

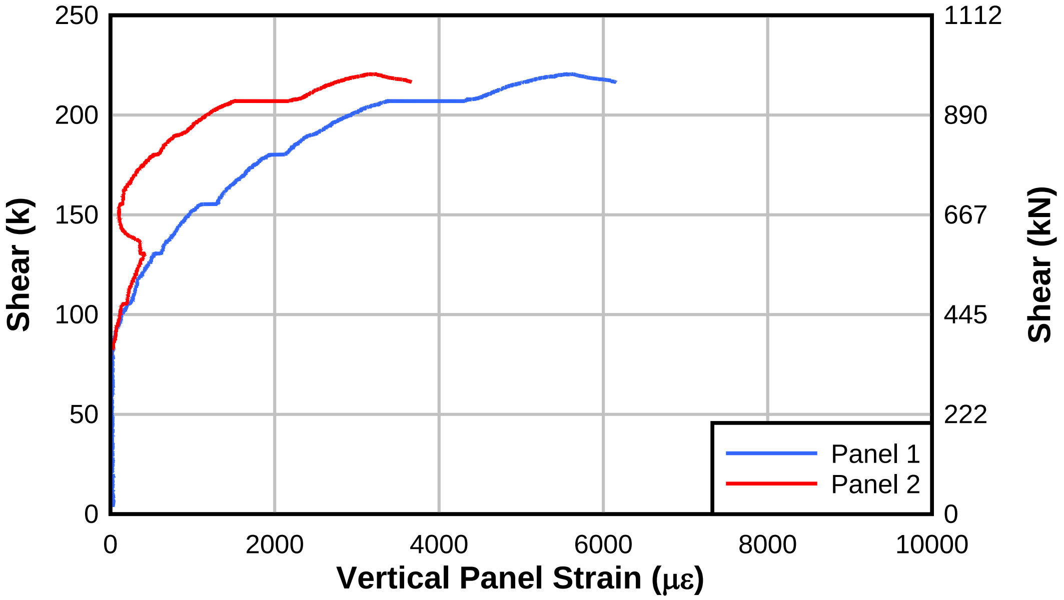

Figure 4.21: Specimen IT6.18.18.E1 average panel vertical strain

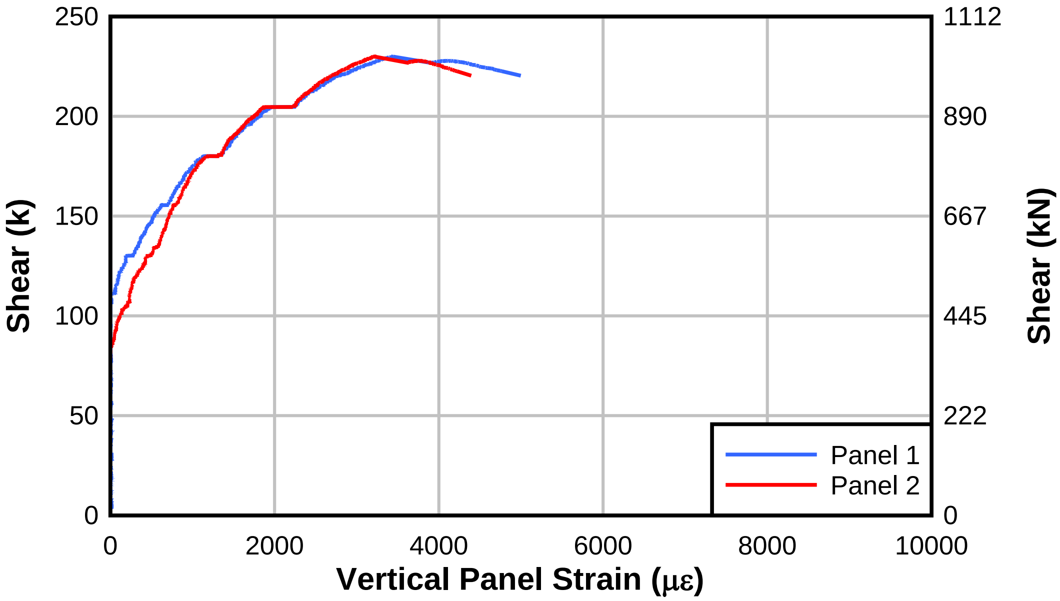

Figure 4.22: Specimen IT6.18.12.E1 average panel vertical strain

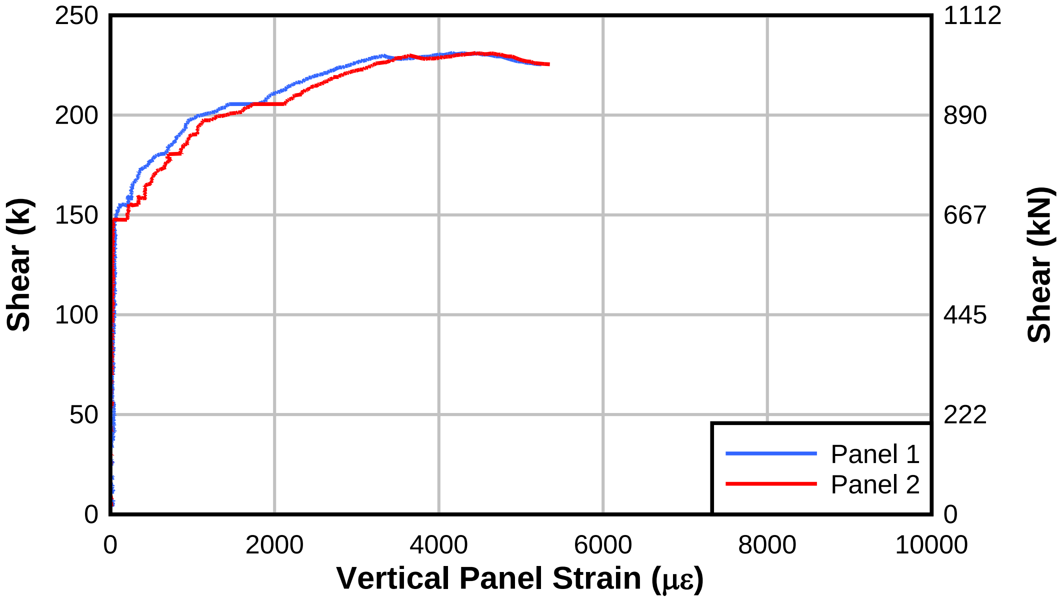

Figure 4.23: Specimen IT6.18.12.E1.FTG average panel vertical strain

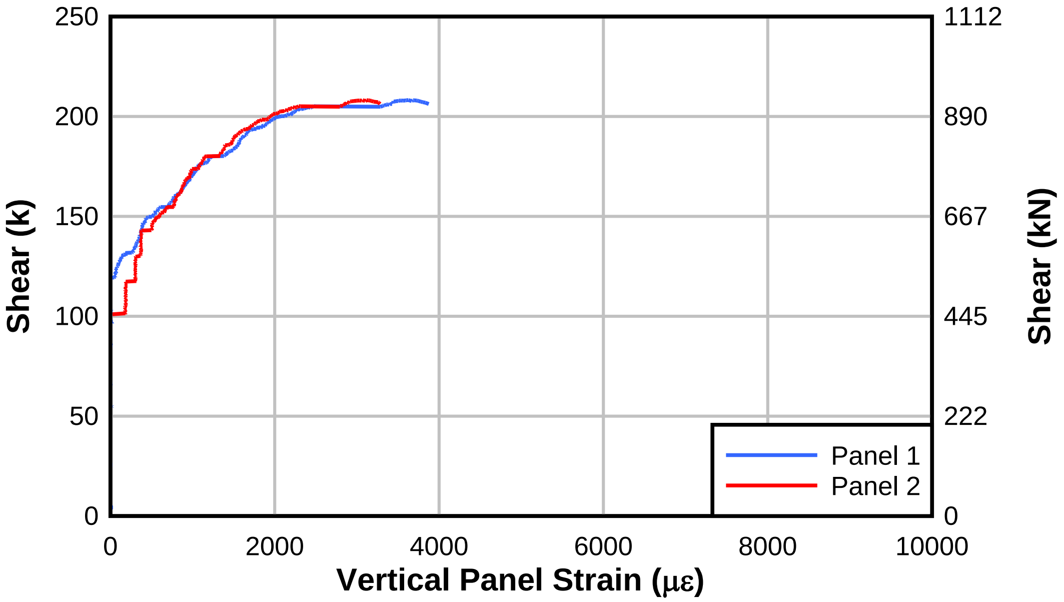

Figure 4.24: Specimen IT6.18.12.E2 average panel vertical strain

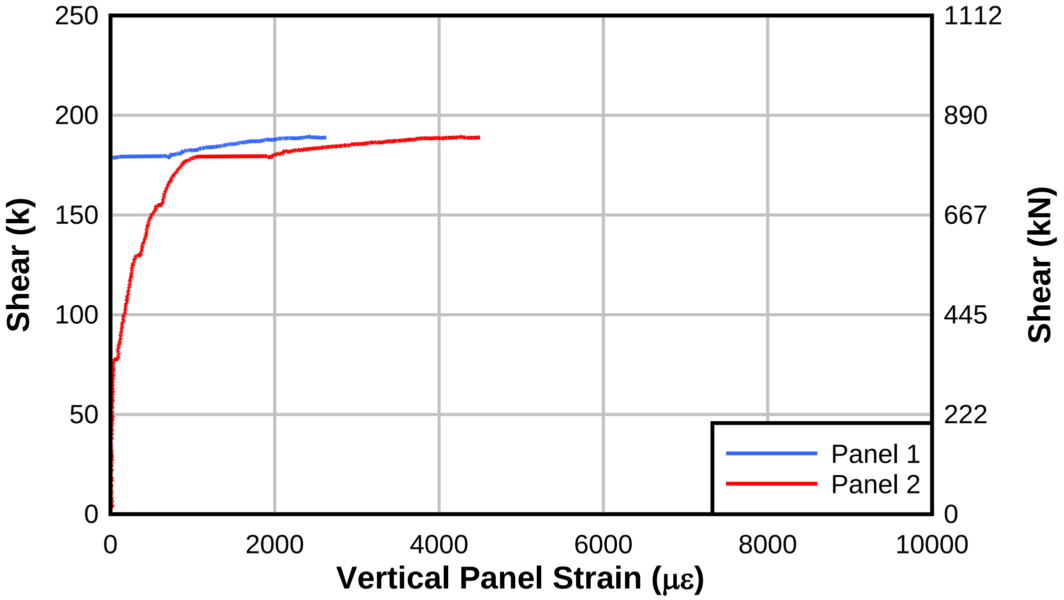

Figure 4.25: Specimen IT6.18.12.E2.FTG average panel vertical strain

Table 4.5: Average Panel Vertical Deformations

Specimen	Panel 1 in. [mm]	Panel 2 in. [mm]
T5.24.12.E1	0.25 [6.4]	0.20 [5.1]
T5.24.12S.E1*	0.10 [2.4]	0.25 [6.4]
IT6.18.18.E1	0.22 [5.6]	0.13 [3.2]
IT6.18.12.E1	0.16 [4.1]	0.15 [3.8]
IT6.18.12.E1.FTG	0.16 [4.1]	0.17 [4.3]
IT6.18.12.E2	0.14 [3.6]	0.12 [3]
IT6.18.12.E2.FTG	0.10 [2.5]	0.18 [4.6]

4.13 TITANIUM STRAIN FROM PANEL ZONE MEASUREMENTS

Using the calculated vertical deformations, the load causing the titanium alloy bars to yield was estimated. The vertical displacement was divided between the cracks crossing a panel based on their relative size at the load step prior to failure. This results in a crack width for every recorded load. To determine the strain in the titanium, it is first necessary to calculate the active bond length. ACI 440 gives the following equation for bond length, derived from force equilibrium:

$$\boldsymbol{l_{db} = \frac{d_b}{4\tau_b} f_{fd}} \qquad \text{ACI 440.2R-08 (13-3)} \quad [4.1]$$

where d_b is the bar diameter, τ_b is the average bond strength, and f_{fd} is the stress in the bar, taken as the yield strength of titanium. Based on tests recorded in Vavra (2016), the average bond strength was taken as 1614 psi (11.13 MPa) for the E1 epoxy, and 988 psi (6.81 MPa) for the E2 epoxy. The active bond length at yield can then be calculated. However, since closely spaced cracks can affect each other, the following method was developed to account for crack interaction.

If the vertical crack spacing is greater than $2l_{db}$ the cracks are assumed to be independent. The average and peak strains in the titanium can be calculated using Equations 5.2 and 5.3, based on a triangular strain distribution, where w_{cr} is the width of the crack.

$$\boldsymbol{\varepsilon_{avg} = \frac{w_{cr}}{2l_{db}}} \qquad [4.2]$$

$$\boldsymbol{\varepsilon_{peak} = 2\varepsilon_{avg}} \qquad [4.3]$$

If, on the other hand, the cracks are spaced closer than $2l_{db}$, interaction between the cracks must be accounted for. It should also be noted that the cracks may not be the same width. Thus a factor k_1 is introduced to define the smaller crack w_{cr2} in terms of the larger crack w_{cr1}. This factor ranges from 0 to 1.0.

$$\boldsymbol{k_1 = \frac{w_{cr2}}{w_{cr1}}} \qquad [4.4]$$

The average strain is then calculated using Equation 5.5, where s_{cr} is the vertical spacing between the cracks.

$$\boldsymbol{\varepsilon_{avg} = \frac{w_{cr1} + w_{cr2}}{l_{db}(k_1 + 1) + s_{cr}}} \qquad [4.5]$$

Since the two triangular strain distributions overlap, the average strain is greater than half the peak strain. Thus another factor k_2 is defined to convert to peak strain. This factor can be derived directly from the geometry of overlapping triangular strain distributions, and ranges from approximately 1.7 to 2.5.

$$\boldsymbol{k_2 = \frac{2l_{db} + k_1 s_{cr}}{l_{db} + k_1^2 s_{cr}\left(1 - \frac{s_{cr}}{4l_{db}}\right)}} \qquad [4.6]$$

The peak strain can then be calculated using Equation 5.7.

$$\boldsymbol{\varepsilon_{peak} = k_2\varepsilon_{avg}} \qquad [4.7]$$

Whichever method is used, the shear corresponding to the calculated titanium strain is taken as the shear at which the bar yields. Table 4.6 lists the calculated shear at which the titanium alloy bars yield for panels 1 and 2.

Table 4.6: Calculated Shear in Specimen at Which Titanium Alloy Bars Yield

Specimen	Panel 1 kip [kN]	Panel 2 kip [kN]
T5.24.12.E1	144 [641]	195 [867]
T5.24.12S.E1*	175 [778]	146 [649]
IT6.18.18.E1	217 [965]	207 [921]
IT6.18.12.E1	221 [983]	221 [983]
IT6.18.12.E1.FTG	229 [5816.6]	218 [970]
IT6.18.12.E2	No yield	207 [921]
IT6.18.12.E2.FTG	No yield	No yield

These results show the titanium alloy bars reaching yield in most cases just before failure. This provides additional confirmation that the titanium alloy bars yielded. Table 4.5 shows that the minimum vertical displacement at peak load is 0.10 in. (2.5 mm). Conservatively assuming this occurs over a single crack and solving Equation 5.2 for active bond length at yield results in an active bond length of 11 in. (280 mm), or 22 in. (560 mm) total. This means that the titanium alloy bar will reach yield if the total active bond length is less than 22 in. (560 mm). Using Equation 4.1, this requires an average bond strength of at least 400 psi (2760 MPa). All of the epoxies reviewed in Table 2.3 of the literature review meet this minimum requirement.

4.8 FATIGUE AND FREEZE-THAW EFFECTS

Figure 4.26 and Figure 4.27 show the internal steel stirrup strain ranges for each specimen. The target maximum strain range was 450 $\mu\varepsilon$, which was correlated to 50 years of equivalent damage. Since the strain gage locations were not directly on the diagonal cracks, the exact strain ranges could not be determined. However, the data indicate that the stirrups were indeed close the target stress range.

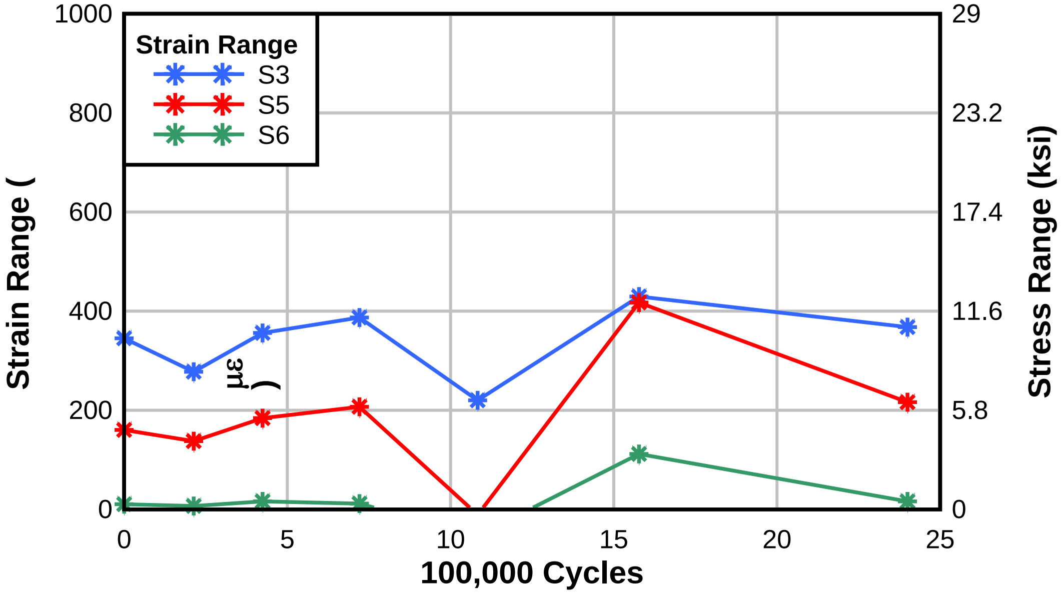

Figure 4.26: Specimen IT6.18.12.E1.FTG internal stirrup strain range

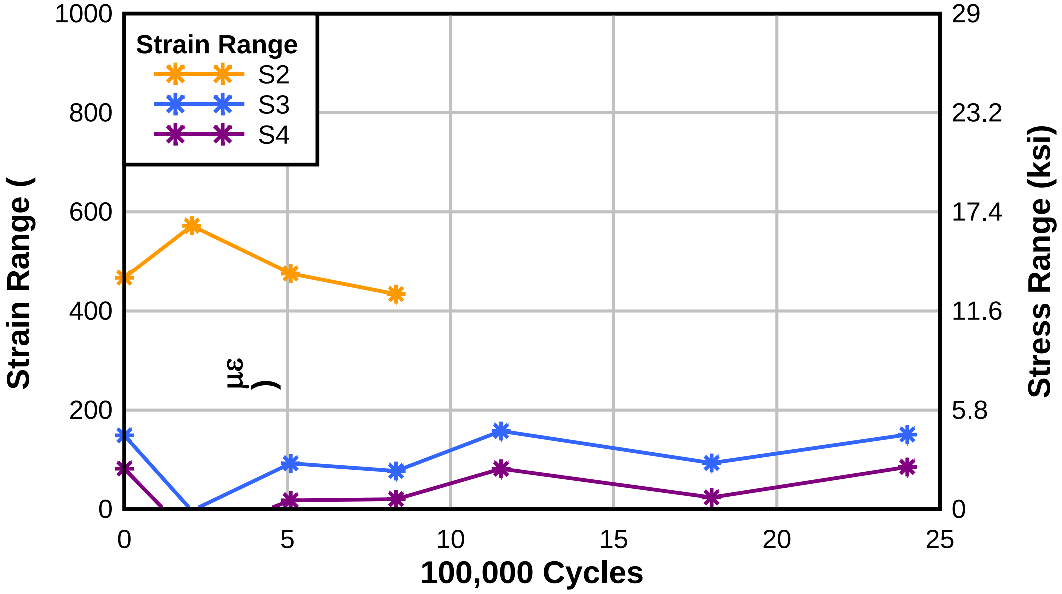

Figure 4.27: Specimen IT6.18.12.E2.FTG internal stirrup strain range

The fatigue and freeze-thaw cycles did not appear to alter the behavior and strength the E1 epoxy in specimen IT6.18.12.E1.FTG, since it failed at nearly the same load as an otherwise similar specimen IT6.18.12.E1. On the other hand, specimen IT6.18.12.E2.FTG showed a 9.0% reduction in strength compared with specimen IT6.18.12.E2. This implies that the E2 epoxy exhibited some strength reduction due to the imposed fatigue and/or freeze-thaw conditions.

The midspan deflection and panel deformations were measured periodically throughout the fatigue tests, but no clear conclusions could be drawn from this data. This is due, in part, to the fact that the sensors had to be removed to prevent damage during the freeze-thaw cycles. Thus cumulative deformations were not captured in these measurements. The data is included, however, in Appendix A. No significant changes were observed in the displacement amplitudes or strain ranges of the rebar or titanium alloy bars during the fatigue tests.

5.0 COMPARATIVE ANALYSIS

In order to develop analysis and design approaches for shear strengthening using titanium alloy bars, the results from the experimental program were compared with predictions using R2K, and the ACI and AASHTO-LRFD design codes. The following sections summarize these results.

5.1 RESPONSE 2000

Models of each specimen were developed in R2K to predict the capacity. R2K is a sectional analysis program, so the user must determine the section of interest to conduct the analysis. The critical section was assumed to be d_v away from the edge of the load plate. Figure 5.1 shows the R2K model of the IT6.18.12.E1 specimen. The measured material properties for the concrete, steel, and titanium in each specimen were used in the models. The predicted and experimental results are listed in Table 5.1.

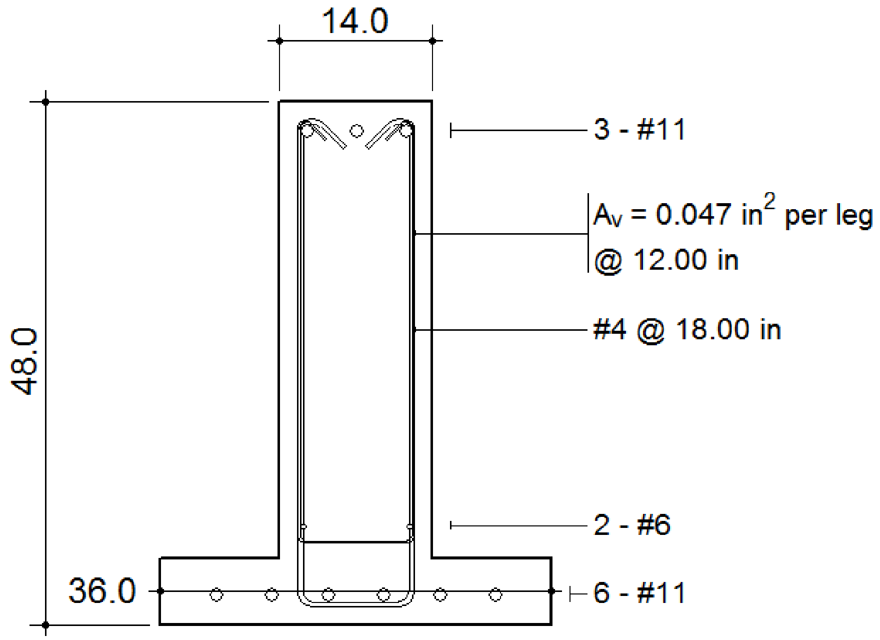

Figure 5.1: R2K beam model

Table 5.1: R2K Prediction Bias

Specimen	$V_{R2k\ Ti}$ kip [kN]	V_{exp} kip [kN]	$V_{exp}/V_{R2k\ Ti}$
T5.24.12.E1	177.4 [789.1]	195.0 [867.4]	1.10
T5.24.12S.E1*	187.0 [831.8]	200.5 [892]	1.07
IT6.18.18.E1	190.7 [848.3]	220.4 [980.4]	1.16
IT6.18.12.E1	204.1 [907.9]	227.8 [1013.4]	1.12
IT6.18.12.E1.FTG	213.3 [948.8]	231.2 [1028.4]	1.08
IT6.18.12.E2	191.6 [852.3]	208.2 [926.1]	1.09
IT6.18.12.E2.FTG	198.4 [882.5]	189.5 [842.9]	0.96
All specimens		Avg Bias COV (%)	1.08 5.31
No environmental		Avg Bias COV (%)	1.11 2.60
E1 specimens		Avg Bias COV (%)	1.11 2.64
E1 (no environmental)		Avg Bias COV (%)	1.11 2.72
E2 specimens		Avg Bias COV (%)	1.02 N/A

For all but the last specimen, the R2K predictions were conservative. For comparison, Higgins *et al.* (2005) found that the average experimental to R2K ratio was 0.98, with a COV of 6.7%. Based on these findings, the specimens in this study are more than one standard deviation higher than the mean. These results closely correspond to those reported by Johnson (2011), who tested similar beams strengthened with NSM CFRP strips, and reported an average R2K bias of 1.16. Johnson attributed the bias to higher effective CFRP stresses than used in the model. Since the strength of the titanium alloy bars is known precisely, this explanation is not valid for the current study. Instead, the underprediction is attributed to the fact that for all specimens, the crack angle was less than 45 degrees, and thus the M/V ratio used in the R2K models was higher than that which occurs at the failure location. Thus, use of the critical section located dv from the loading plate is expected to produce conservative outcomes.

5.2 ACI 318 AND ACI 440 PREDICTED STRENGTH

The shear provisions of the ACI 318 code are based on the principal of superposition, in which the shear contributions of the concrete and the steel stirrups are combined. The assumed diagonal crack angle in the model is 45° and the steel is assumed to be at yield at member strength. The nominal shear strength is calculated as:

$$\boldsymbol{V_n = V_c + V_s} \qquad \text{ACI 318-11 (11-2) [5.1]}$$

where V_c is the concrete contribution to shear strength and V_s is the steel contribution to shear strength. For members with no axial load, the concrete contribution to shear strength V_c may be calculated as:

$$\boldsymbol{V_c = 2\lambda\sqrt{f'_c}b_w d} \qquad \text{ACI 318-11 (11-3) [5.2]}$$

where λ is a lightweight concrete reduction factor, f'_c (psi) is the concrete compressive strength, b_w is the width of the web, and d is the beam depth. Alternatively, a more detailed expression including the shear-moment ratio may be used: In this equation, ρ_w is the ratio between the tensile steel reinforcement and the web cross-sectional area.

$$\boldsymbol{V_c = \left(1.9\lambda\sqrt{f'_c} + 2500\rho_w \frac{V_u d}{M_u}\right) b_w d} \qquad \text{ACI 318-11 (11-5) [5.3]}$$

where ρ_w is the ratio between the area of the tensile steel reinforcement and the web cross-sectional area, and V_u and M_u are the shear and moment corresponding to the section under consideration. For these calculations, the section was assumed to be d_v away from the edge of the loading plate, where d_v is the effective shear depth taken from AASHTO-LRFD. The steel contribution to shear is calculated as:

$$V_s = \frac{A_v f_{yt} d}{s} \qquad \text{ACI 318-11 (11-15) [5.4]}$$

where A_v is the cross sectional area of the transverse reinforcing, f_{yt} is the yield strength of the transverse reinforcing, d is the beam depth, and s is the stirrup spacing.

ACI 440 builds on the provisions of ACI 318 and includes an additional term for the FRP contribution to shear:

$$\boldsymbol{\phi V_n = \phi\left(V_c + V_s + \psi_f V_f\right)} \qquad \text{ACI 440.2R-08 (11-2) [5.5]}$$

where the reduction factor ψ_f is 0.85 for partially wrapped members, and 0.95 for fully wrapped members. The FRP contribution to shear is calculated as:

$$\boldsymbol{V_f = \frac{A_{fv} f_{fe}(\sin\alpha + \cos\alpha) d_{fv}}{s_f}} \qquad \text{ACI 440.2R-08 (11-3) [5.6]}$$

where A_{fv} is the cross sectional area of the FRP bar, d_{fv} is the beam depth, s_f is the FRP bar spacing, and α is the angle of orientation of the FRP bars. f_{fe} is the nominal tensile stress in the FRP reinforcement at failure, calculated as the maximum achievable strain times the modulus of elasticity. The code limits the strain allowed in the FRP reinforcement to 4000 με.

Using the shear strength equations from ACI 318 and 440, with Equation 6.3 being used to calculate V_c, the strength of each specimen was predicted. Since the experimental data showed that the titanium alloy bars reach their yield strength, the 4000 με limit was disregarded, and f_{fe} was taken as the yield strength of the titanium alloy bars. Section 5.7 discusses this decision in more detail. For comparison with the other methods, the FRP reduction factor was taken as 1.0. The reduction factor is addressed in detail in Section 5.13. The ACI predictions compared with experimental results are shown in Table 5.2.

Table 5.2: ACI 318 and 440 prediction bias

Specimen	$V_{318+440}$ kip [kN]	V_{exp} kip [kN]	$V_{exp}/V_{318+440}$
T5.24.12.E1	171.2 [761.6]	195.0 [867.4]	1.14
T5.24.12S.E1*	177.9 [791.5]	200.5 [892]	1.13
IT6.18.18.E1	174.5 [776.3]	220.4 [980.4]	1.26
IT6.18.12.E1	197.7 [879.4]	227.8 [1013.4]	1.15
IT6.18.12.E1.FTG	202.9 [902.4]	231.2 [1028.4]	1.14
IT6.18.12.E2	189.0 [840.9]	208.2 [926.1]	1.10
IT6.18.12.E2.FTG	192.3 [855.3]	189.5 [842.9]	0.99
All specimens		Avg Bias COV (%)	1.13 6.69
No environmental		Avg Bias COV (%)	1.16 4.83
E1 specimens		Avg Bias COV (%)	1.16 4.30
E1 (no environmental)		Avg Bias COV (%)	1.17 4.63
E2 specimens		Avg Bias COV (%)	1.04 N/A

These results demonstrate that the ACI equations conservatively predict the strength of the specimens, and may be used for designing shear strengthening using titanium alloy bars.

5.6.1 AASHTO-LRFD Predicted Strength

The AASHTO-LRFD shear provisions are based on the Modified Compression Field Theory (MCFT). Like the ACI approach, it is based on the superposition of concrete and steel contributions to shear strength. However, it also takes into account the angle of inclination of the shear stresses and the strain in the longitudinal reinforcement. This method generally produces more accurate results. The shear strength is taken as the sum of the shear strength of the concrete and the shear strength of the stirrups. These values are calculated as follows:

$$\boldsymbol{V_c = 0.0316\beta\sqrt{f'_c}b_v d_v} \qquad \text{AASHTO LRFD 2012 (5.8.3.3-3)} \quad [5.7]$$

$$\boldsymbol{V_s = \frac{A_v f_y d_v(\cot\theta + \cot\alpha)\sin\alpha}{s}} \qquad \text{AASHTO LRFD 2012 (5.8.3.3-4)} \quad [5.8]$$

where b_v is the width of the web, d_v is the effective shear depth, A_v is the cross-sectional area of the transverse reinforcing, f_y is the yield strength of the transverse reinforcing, s is the stirrup spacing, and f'_c (ksi) is the concrete compressive strength. The angle α is the angle of inclination of the stirrups, β is a factor indicating the ability of diagonally cracked concrete to transmit tension and shear, and the angle θ is the angle of inclination of the diagonal compressive stresses. These values are dependent on the strain in the longitudinal tension reinforcement, and are calculated as:

$$\boldsymbol{\beta = \frac{4.8}{1 + 750\varepsilon_s}} \qquad \text{AASHTO LRFD 2012 (5.8.3.4.2-1)} \quad [5.9]$$

$$\boldsymbol{\theta = 29 + 3500\varepsilon_s} \qquad \text{AASHTO LRFD 2012 (5.8.3.4.2-3)} \quad [5.10]$$

where ε_s is the strain in the longitudinal tension reinforcement. In order to solve these equations, it is first necessary to assume a starting value of strain in the longitudinal reinforcement. Using this value, the shear strength can then be calculated. Using the *M/V* ratio of the section being considered, the moment at the section can be calculated. Finally, the strain in the tensile reinforcement can be estimated as:

$$\boldsymbol{\varepsilon_s} = \frac{\left(\frac{|\boldsymbol{M_u}|}{\boldsymbol{d_v}} + \mathbf{0.5}\boldsymbol{N_u} + \left|\boldsymbol{V_u} - \boldsymbol{V_p}\right| - \boldsymbol{A_{ps}f_{po}}\right)}{\boldsymbol{E_sA_s} + \boldsymbol{E_pA_{ps}}}$$

AASHTO LRFD 2012 (5.8.3.4.2-4) [5.11]

When the prestressing and axial force terms are removed, this equation simplifies significantly:

$$\boldsymbol{\varepsilon_s} = \frac{\frac{|\boldsymbol{M_u}|}{\boldsymbol{d_v}} + |\boldsymbol{V_u}|}{\boldsymbol{E_sA_s}} \qquad [5.12]$$

In this equation, E_s and A_s are the modulus of elasticity and cross sectional area, respectively, of the longitudinal tension steel. The calculated strain is then compared to the assumed strain, and iterated until convergence is reached.

The titanium alloy bar contribution to shear strength was calculated based on Equation 6.8. Since only vertical bars were used in this study, the titanium alloy bar contribution is calculated as:

$$\boldsymbol{V_{ti}} = \frac{\boldsymbol{A_{vti}f_{yti}d_v}\,\mathbf{cot}\,\boldsymbol{\theta}}{\boldsymbol{s_{ti}}} \qquad [5.13]$$

where A_{vti} is the cross sectional area of the titanium alloy bars, f_{yti} is the yield strength of the titanium alloy bars, and s_{ti} is the spacing of the titanium alloy bars. The shear strength of each specimen was calculated using the AASHTO-LRFD method, and the AASHTO-LRFD predicted strengths are compared with the experimental results in Table 5.3.

Table 5.3: AASHTO-LRFD Prediction Bias

Specimen	V_{AASHTO} kip [kN]	V_{exp} kip [kN]	V_{exp}/V_{AASHTO}
T5.24.12.E1	163.1 [725.4]	195.0 [867.4]	1.20
T5.24.12S.E1*	172.8 [768.8]	200.5 [892]	1.16
IT6.18.18.E1	176.6 [785.4]	220.4 [980.4]	1.25
IT6.18.12.E1	195.6 [870.1]	227.8 [1013.4]	1.16
IT6.18.12.E1.FTG	198.9 [884.6]	231.2 [1028.4]	1.16
IT6.18.12.E2	189.5 [842.8]	208.2 [926.1]	1.10
IT6.18.12.E2.FTG	191.6 [852.1]	189.5 [842.9]	0.99
All specimens		Avg Bias COV (%)	1.15 6.64
No environmental		Avg Bias COV (%)	1.17 4.16
E1 specimens		Avg Bias COV (%)	1.19 2.83
E1 (no environmental)		Avg Bias COV (%)	1.19 2.95
E2 specimens		Avg Bias COV (%)	1.04 N/A

These results demonstrate that the AASHTO-LRFD approach conservatively predicted the strength of the specimens, and may be used for design of shear strengthening using titanium alloy bars.

5.4SHEAR STRENGTHENING STRAIN LIMITS

The yield strain of the titanium alloy bars used in this study is approximately 9000 με. Previous research has suggested that FRP shear strengthening applications be limited to 4000 με. This section provides an overview of how this recommendation was developed, and the extent to which it is applicable.

Khalifa *et al.* (1998) tested a series of small scale beams strengthened with CFRP sheets. Based on their findings, they recommended that for design the strain in the CFRP be limited to between 4000 με and 5000 με, in order to maintain the shear integrity of the concrete. Building on this research, Nanni *et al.* (2004) developed design equations for NSM CFRP strips. The authors utilized the same 4000 με limit, citing concerns that large shear cracks could compromise aggregate interlock.

ACI 440.2R-08 does not have specific design recommendations for NSM shear strengthening systems. Design recommendations are for CFRP sheet systems. However, the same 4000 με limit is present, and the code states that "higher strains should not be used for FRP shear-strengthening applications." The code cites testing by Priestley *et al.* (1996), and experience. Priestley *et al.* (1996) tested concrete columns strengthened with CFRP jackets.

For most CFRP materials this limit does not present a problem, since it happens to coincide with the limits imposed by epoxy strength. A CFRP bar with a modulus of 20,000 ksi (138 GPa), for instance, would be limited to a stress of 80 ksi. Johnson (2011) reviewed the CFRP stresses from 14 studies and reported an average stress of 64 ksi (441 MPa) at failure, meaning for most materials the 4000 με limit will not apply. This is likely the reason it has not yet come under closer scrutiny.

The goal of the strain limit is to limit crack widths. However, in addition to crack width, strain is also a function of bond strength and CFRP diameter or size. The tests from which the 4000 με limit was derived all used CFRP sheets, and thus may not be applicable to NSM systems. Future codes should move towards performance-based criteria to avoid issues that arise from using different methods and materials. However, more research is likely needed to determine acceptable crack widths.

For each specimen in this study, the titanium alloy bars reached their yield strain of 9000 με before shear strength was achieved. This was likely due to the better bond performance of NSM systems and of the epoxy bond to the titanium bars due to the surface treatment of the bars. These results indicate that the 4000 με limit may not be applicable to NSM systems generally, and particularly for the titanium alloy bars with hooked anchorages used in this study.

5.5 EPOXY COMPARISON

The test results showed that specimens strengthened using epoxy E1 achieved higher capacities than those strengthened with epoxy E2. This was particularly evident when long term durability was considered. There were no major issues working with epoxy E1. It had a sufficiently long pot life, and has a good wet consistency for gripping the concrete and the deformations in the titanium alloy bars. Just as Johnson (2011) found, it showed no strength reduction after exposure to fatigue and freeze thaw cycles.

Specimens with epoxy E2 exhibited lower strength and deformation capacity. There were several characteristics that lead to this outcome. First, it had a short pot life, meaning it was already starting to set when the titanium alloy bar was placed. Second, it had a granular consistency and was very stiff, raising concerns that it may not fill the bar deformations as easily. Finally, it did not wet the concrete surfaces well. Movement of the titanium alloy bar after its placement in the groove was observed to create voids around the bars, as illustrated in Figure 5.2. These voids were identified after testing specimen IT6.18.12.E2.FTG. Movement of the titanium alloy bar is necessary to get the hooks in the holes. The poor wetting of the concrete surface would also present a problem for overhead installations.

Figure 5.2: Epoxy E2 voids

The specimen with epoxy E2 that was not exposed to environmental durability testing produced strengths similar to specimens with epoxy E1, meaning variations in epoxies and installation methods can be accommodated. On the other hand, epoxy E2 showed reduced strength after being subjected to fatigue and freeze-thaw cycles. Selection of epoxy type is important when considering long-term durability and additional studies are warranted to ensure long-term durability of the selected epoxy system.

5.6 STRAIN COMPATIBILITY

The strain in the titanium and steel stirrups was not expected to be compatible, since the bar diameters and bonding mechanisms are different. Active bond length is directly proportional to bar diameter, and thus, assuming bond strength is constant, the active bond length of the 1/4 in. (6.3 mm) titanium alloy bars should be half the bond length of the 1/2 in. (12.7 mm) steel bars. This in turn means the strain in the titanium would be twice as high. In reality, the bond strength varies significantly and tends to be stronger for the titanium-epoxy bond, particularly for the E1 epoxy specimens. The E1 epoxy has a bond strength that is two to three times higher than the concrete-steel bond strength, and thus the strain can be four to six times as high.

Measuring the differences in strain in steel and titanium stirrups was often difficult, since the strain gages were not directly on the crack or located coincidently. However, three cases were found in which the steel and titanium alloy stirrups were sufficiently close together, and the strain gages were near the diagonal crack. These are shown in Figures 5.3 through 5.5. Figure 5.3 shows the titanium alloy bar gaining strain at a much higher rate than the adjacent steel stirrup. In this case, there was no interaction from nearby cracks, and the strain gages were roughly equidistant from the main crack, illustrating that the titanium alloy bar strain can be much higher than the steel strain. Figures 5.4 and 5.5 were taken from specimens using the E2 epoxy, and show the titanium alloy bars gaining strain at lower rates relative to the steel. Also note that the lack of crack feathering seen in the crack map of Figure 5.5 indicates reduced epoxy bond.

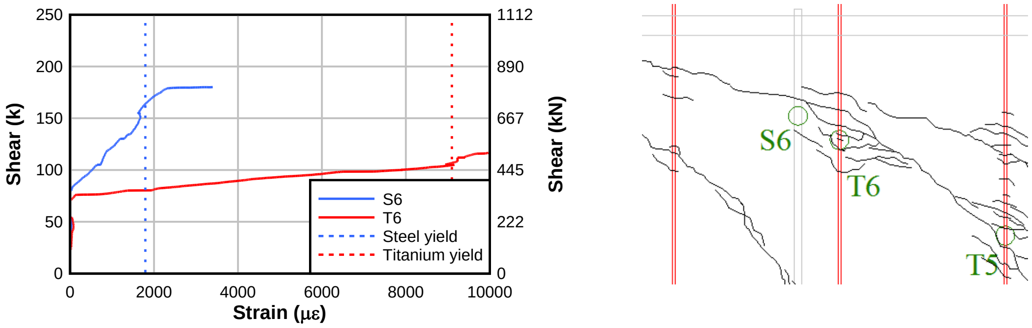

Figure 5.3: Specimen IT6.18.12.E1 strain compatibility S6-T6

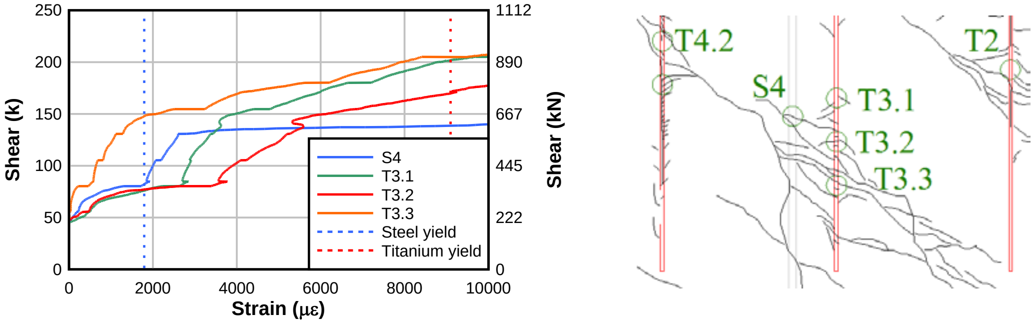

Figure 5.4: Specimen IT6.18.12.E2 strain compatibility S4-T3

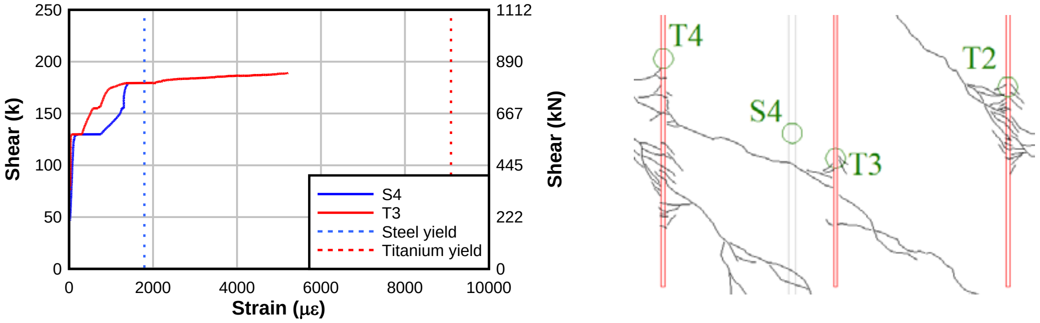

Figure 5.5: Specimen IT6.18.12.E2.FTG strain compatibility S4-T3 (backbone curves shown for clarity)

5.7 SERVICE-LEVEL PERFORMANCE

R2K was used to estimate service-level changes in performance. This was taken as the shear at which the internal steel stirrup stress achieved 20 ksi (138 MPa), which represents the onset of fatigue damage for conventional reinforcing steel stirrups. R2K reports a combined stirrup stress, but as discussed in Section 5.9, the strain in the titanium will be twice the strain in the steel even while the modulus of elasticity is about half that of steel which results in stresses that will be about the same in both the steel and titanium. This is especially true for the R2K analyses, since it does not directly account for bond stresses. The results of this analysis are shown in Table 5.4.

Table 5.4: Service Level Strength Increases

Specimen	$V_{Serv.Unstr}$ kip [kN]	$V_{Serv.Str}$ kip [kN]	$V_{Serv.Incr}$ %
T5.24.12.E1	68.4 [304.2]	74.5 [331.4]	8.9
T5.24.12S.E1*	74.3 [330.3]	80.3 [357.2]	8.1
IT6.18.18.E1	86.9 [386.5]	90.9 [404.5]	4.7
IT6.18.12.E1	90.3 [401.7]	96.5 [429.3]	6.9
IT6.18.12.E1.FTG	93.1 [414.2]	99.2 [441.3]	6.5
IT6.18.12.E2	87.0 [386.9]	92.9 [413.2]	6.8
IT6.18.12.E2.FTG	88.8 [394.8]	94.7 [421.1]	6.7

The calculated service-level shear capacity increases are fairly small, which makes sense, as very little supplemental material was added to the specimens to reduce the demand on the internal steel.

5.8 STIRRUP DEBONDING R2K ANALYSIS

R2K is based on the modified compression field theory (MCFT) for predicting shear response. This theory, modified an earlier compression field theory (CFT) by accounting for the tensile strength of concrete, which compression field theory ignored. In theory, debonding of the titanium and steel stirrups can be modeled by manually decreasing the tensile strength of the concrete, moving from MCFT to CFT. In order to capture the potential effects of stirrup debonding using R2K, the concrete tensile strength was gradually decreased toward zero for specimen IT6.18.12.E2.FTG, and the predicted strength was recorded. This specimen was chosen for analysis since it exhibited the most debonding. The results of this analysis are shown in Figure 5.6.

It is also possible to model just the titanium alloy bar debonding by manually decreasing the modulus of elasticity of the bars. This is shown in Figure 5.7. The same specimen (IT6.18.12.E2.FTG) was used for this analysis.

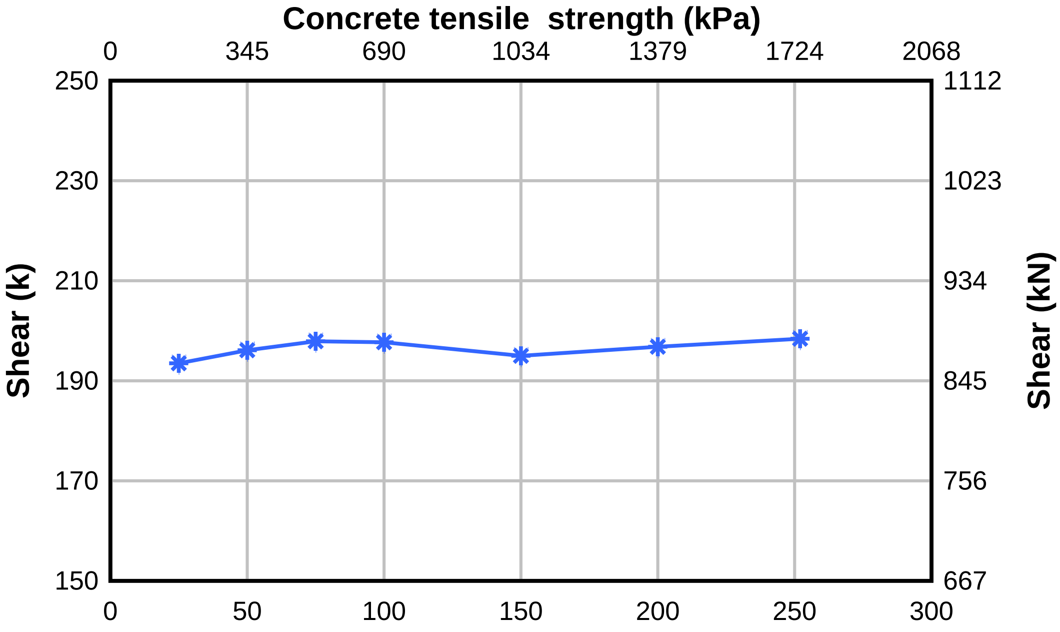

Figure 5.6: R2K debonding (default tensile strength: 252 psi)

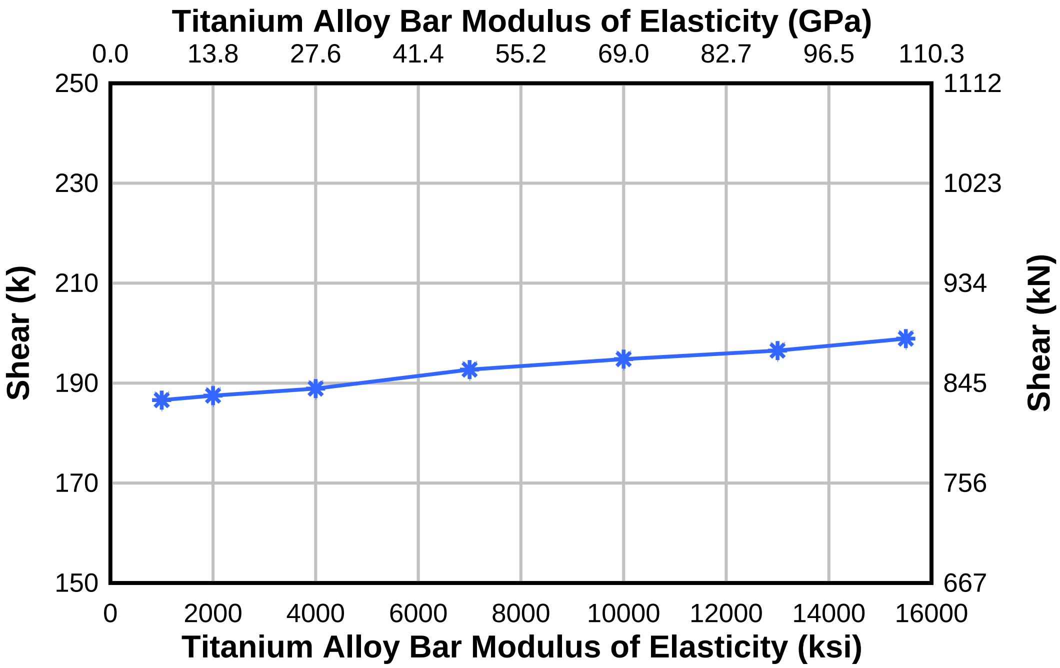

Figure 5.7: R2K debonding (default E = 15,500 ksi)

Results show a direct correlation between specimen capacity and the modulus of elasticity (stiffness of the bars), while the correlation between specimen capacity and concrete tensile strength was much weaker, although at very low tensile strengths, the capacity tends to diminish slightly and looks to be around 190 kips if the tensile strength is taken around zero (fully debonded stirrups). The capacity of specimen IT6.18.12.E2.FTG was 189.5 kip (842.9 kN). By decreasing the modulus of elasticity for the titanium alloy bars by about 1/3, it is possible to achieve predicted strengths closer to the experimentally observed results.

5.9 ACTUAL M/V RATIO R2K ANALYSIS

As mentioned previously, the M/V ratio used to predict the specimen capacity in R2K was calculated by assuming the critical section is taken at a point dv away from the edge of the loading plate. This is a reasonable and conservative assumption for design purposes, but it produced conservative results compared to the experimental results. In order to reflect the failure diagonal crack location passing at a section farther away than dv away from the edge of the loading plate in R2K, models were built for each specimen using the M/V ratio corresponding to the section where the failure diagonal crack actually crossed the tension steel. The results of this analysis are shown in Table 5.5.

Table 5.5: Actual M/V Ratio R2K Analysis

Specimen	M/V ft. [mm]	V_{exp} kip [kN]	V_{R2K} kip [kN]	$V_{exp}/V_{R2k\ Ti}$
T5.24.12.E1	4.08 [1245]	195.0 [867.4]	193.1 [859]	1.01
T5.24.12S.E1*	5.64 [1720]	200.5 [892]	195.7 [870.5]	1.02
IT6.18.18.E1	1.88 [574]	220.4 [980.4]	205 [911.9]	1.08
IT6.18.12.E1	3.00 [914]	227.8 [1013.4]	235.1 [1045.8]	0.97
IT6.18.12.E1.FTG	1.53 [465]	231.2 [1028.4]	234.8 [1044.4]	0.98
IT6.18.12.E2	2.87 [874]	208.2 [926.1]	222.5 [989.7]	0.94
IT6.18.12.E2.FTG	4.02 [1224]	189.5 [842.9]	235.2 [1046.2]	0.81
All specimens			Avg Bias COV (%)	0.97 8.15
No environmental			Avg Bias COV (%)	1.00 4.76
E1 specimens			Avg Bias COV (%)	1.01 3.63
E1 (no environmental)			Avg Bias COV (%)	1.02 3.72
E2 specimens			Avg Bias COV (%)	0.87 N/A

When the actual M/V ratios are used, the average bias associated with the R2K predictions becomes much closer to 1.0. This indicates that much of the bias shown in Table 5.1 can be attributed to using a conservative M/V ratio.

5.10 STRENGTH REDUCTION FACTORS

Using the results from the experimental tests, strength reduction factors were calculated for the R2K, ACI, and AASHTO-LRFD analysis methods. The factors were calibrated to give a 1 in 10,000 probability of understrength, which corresponds approximately to a β of 3.5 for most code calibrations. This is conservative, as the expected design life of the repair is expected to be only 20 years instead of 75 years as assumed for new designs. The AASHTO-LRFD and ACI reduction factors were based on ACI 440, in which there is a partial safety strength reduction factor ψ for the titanium in addition to the general strength reduction factor ϕ. The code specified values of ϕ were used, and ψ was modified as necessary to achieve the target reliability. Since R2K does not use superposition, a single reduction factor ϕ was calculated. The factors were calculated iteratively, decreasing from 1.0 until β was larger than 3.5.

Two sets of factors were developed. First, a set of factors was developed using only the E1 specimens. However, since these tests produced limited variability, no additional partial safety strength reduction factors were necessary to achieve a β of at least 3.5. Taking the critical section d_v away from the edge of the loading plate, R2K also can be used without factoring the results. Table 5.6 summarizes these results.

Table 5.6: Reduction Factors for E1 Epoxy Specimens

	φ	ψ	β
R2K	1.00	N/A	3.62
AASHTO	0.90	1.00	7.57
ACI	0.75	1.00	8.28

Second, a set of factors was developed using all of the tests, including both E1 and E2 specimens and the fatigue and freeze-thaw specimens. Table 5.7 summarizes these results.

Table 5.7: Reduction Factors for All Epoxies Including Long-Term Durability

	φ	ψ	β
R2K	0.88	N/A	3.50
AASHTO	0.90	0.80	3.50
ACI	0.75	1.00	5.02

Applying these factors to the R2K, AASHTO-LRFD, and ACI predictions for the weakest specimen, IT6.18.12.E2.FTG, results in overstrengths of 1.12, 1.12, and 1.31, respectively.

5.11 SUMMARY

The experimental results showed that superposition of the concrete, steel, and titanium contributions to shear strength is reasonable for design purposes. Thus the ACI and AASHTO-LRFD design methods may be used, simply adding an extra term for the titanium alloy bars:

$$\boldsymbol{V_n = V_c + V_s + V_{ti}} \qquad [5.14]$$

For ACI, the titanium contribution is calculated as:

$$\boldsymbol{V_{ti} = \frac{A_{ti} f_{yti} d}{s_{ti}}} \qquad [5.15]$$

No partial safety strength reduction factor is required for the titanium alloy bars using this approach. For a general epoxy, the factors do not change, but the reliability index reduces from 8.28 to 5.02

AASHTO-LRFD framework, the titanium contribution is calculated as:

$$\boldsymbol{V_{ti} = \psi \frac{A_{vti} f_{yti} d_v \cot\theta}{s_{ti}}} \qquad [5.16]$$

where, for a general epoxy, ψ is taken as 0.80, but may be taken as 1.0 for the E1 epoxy.

R2K may also be used to predict the strength of a NSM TiAB strengthened girder. If the E1 epoxy is used, no reduction is necessary. For a general epoxy, a reduction factor of 0.88 should be used. This could be conservatively rounded to 0.85 for simplification.

6.0 CONCLUSIONS

In this research program, seven (7) full-scale reinforced concrete girders strengthened in shear with titanium alloy bars were tested to failure. The specimens were designed to simulate 1950's era bridge girders in materials, proportions, and construction. Two specimens were subjected to simultaneous freeze-thaw and fatigue cycles before being tested to failure. Based on the experimental tests and analytical studies, the following conclusions are presented:

- NSM titanium alloy bars provided significant increases in the shear strength of the specimens when compared to similar unstrengthened specimens.

- For specimens that failed in diagonal-tension, the failure mode was shear-compression. This was followed by significant opening of the main diagonal crack, over which the titanium alloy stirrups tended to rupture.

- Based on strain gage and vertical deformation measurements, it was determined that both the internal steel stirrups and the titanium alloy stirrups crossing the main diagonal crack achieve their respective yield strengths prior to failure.

- Since the titanium alloy bar diameter is half the diameter of the internal steel stirrups and the epoxy bond between the titanium and concrete is efficient, the strain in the titanium alloy bars was observed to be least twice as high as the strain in an adjacent steel stirrup. This means that although the modulus of elasticity of the titanium alloy bars is about half the modulus of elasticity of steel, the stress in the titanium is at least equal to the stress in the internal stirrups when the materials are in the elastic range. For epoxy with high bond stiffness and strength, the stress in the titanium can be higher than the stress in the internal steel stirrups.

- Two specimens had groove depths varying from 3/8 in. (9.5 mm) to 9/16 in. (14.3 mm). The shallower grooves tended to develop chevron cracks in the epoxy, without cracking the surrounding concrete. The deeper grooves did not develop chevron cracks, instead initiating feathering cracks in the concrete. This allowed for shorter active bond lengths. Deeper grooves also make it easier to accommodate construction tolerances.

- Six of the seven specimens were strengthened with double leg titanium alloy bar stirrups. One specimen had single leg titanium alloy bar stirrups. The single leg specimen exhibited no noticeable difference in strength or stiffness compared to the similar double leg specimen. However, installation was more challenging for the single leg specimen, and the discontinuity across the stem from the hooks in the tension zone caused large longitudinal cracking not observed in other specimens. Double leg stirrups are recommended as they preclude these cracks, and also provide additional confinement of the compression zone for negative moment regions.

- Five specimens were strengthened using epoxy E1, while two were strengthened using epoxy E2. Specimens not subjected to fatigue and freeze thaw were able to achieve at least their predicted strength regardless of the epoxy used, although specimens strengthened with epoxy E1 achieved higher strengths.

- Two specimens were subjected to 120 freeze thaw cycles and 2,400,000 fatigue cycles simultaneously. The specimen strengthened with epoxy E1 showed no deterioration in strength or stiffness. The specimen strengthened with epoxy E2 showed a loss in strength, although the initial stiffness was similar. Care should be taken when selecting an epoxy to ensure adequate durability for the given application.

- To prevent loss of aggregate interlock, ACI 440 prescribes a maximum FRP strain of 4,000 $\mu\varepsilon$ based on research developed using FRP sheets. Since this limit was developed for FRP sheets, it may not be applicable to NSM systems. In the present study, the titanium alloy bars consistently reached their yield strain of approximately 9,000 $\mu\varepsilon$ prior to diagonal-tension failure of the specimens.

- Response 2000, AASHTO-LRFD, and ACI analysis procedures were shown to conservatively predict the specimen strengths. Using the available data, strength reduction factors were proposed that provide a 1/10,000 probability of understrength. These can be used for design purposes.

6.1 ADDITIONAL RESEARCH

Based on the test results, the following recommendations are made for future research:

Investigate the use of stainless steel as an alternative to titanium alloy bars. Stainless steel bars would have the advantage of being stiffer than titanium. However, the bar sizes would need to be larger or more bars would be required. Larger bar sizes would increase bond lengths. Also, the bond strength could be weaker due to the bar size and deformations, perhaps offsetting any gains from the higher stiffness. The groove depths would also need to be larger, increasing costs and increasing the risk of damaging the internal steel.

Further investigate the epoxy-titanium bond strength, using varying bond lengths and sufficiently large concrete sections to prevent failure in the concrete.

Test specimens under fatigue and freeze-thaw cycles separately, to determine the individual contributions to the reduction in bond strength for different epoxy types.

Test long term durability of alternative epoxies, to ensure adequate performance for applications including fatigue, freeze-thaw, and moisture exposure.

REFERENCES

American Association of State Highway Officials. *AASHTO LRFD Bridge Design Specifications, 6th edition*. AASHTO, Washington, D.C., 2012.

American Concrete Institute. ACI 440.2R-08: Guide for the Design and Construction of Externally Bonded FRP Systems for Strengthening Concrete Structures. In *ACI Manual of Concrete Practice*. Farmington Hills, Michigan, 2008.

American Concrete Institute. ACI 318-11: Building Code Requirements for Structural Concrete and Commentary," *ACI Manual of Concrete Practice*, Farmington Hills, Michigan, 2011.

Amneus, D. "Methods for strengthening flexural steel details in reinforced concrete bridge girders using a near-surface mounted retrofitting technique." Thesis, Oregon State University, 2014.

Asplund, S.O. Strengthening Bridge Slabs with Grouted Reinforcement. In ACI Journal, *Proceedings, Vol. 20 No. 4*, 1949, pp. 397-406.

Barker, L. *Flexural Anchorage Performance and Strengthening on Negative Moment Regions Using Near-Surface Mounted Retrofitting in Reinforced Concrete Bridge Girders.* Thesis, Oregon State University, 2014.

Barros, J.A O., and S.J.E. Dias. Near Surface Mounted CFRP Laminates for Shear Strengthening of Concrete Beams. In *Cement and Concrete Composites, Vol. 28 No. 3*, 2006, pp. 267-292.

Bentz, E.C. Response-2000: *Reinforced Concrete Sectional Analysis using Modified Compression Field Theory (Version 1.05)* [Computer Software]. University of Toronto, 2000.

Dawson, M. *Scale Effects on Reinforced Concrete Beams Strengthened for Shear with Discrete Externally Bonded Carbon Fiber-Reinforced Polymer U-Wraps*. Thesis, Oregon State University. 2008.

De Lorenzis, L., and A. Nanni. Shear Strengthening of Reinforced Concrete Beams with Near-Surface Mounted Fiber-Reinforced Polymer Rods. In *ACI Structural Journal, Vol. 98 No. 1*, 2001, pp. 60-68

De Lorenzis, L., and A. Nanni. Characterization of FRP Rods as Near-Surface Mounted Reinforcement. In *Journal of Composites for Construction, Vol. 5 No. 2,* 2001, 2001, pp. 114-121.

Fernandes, P., P. Silva, J. Sena-Cruz, M. Azenha, T. Teixeria, and J. Barros. Bond and Flexural Behaviour of a NSM CFRP Strengthening System Under Fatigue Loading. Presented at the 7th International Conference on FRP Composites in Civil Engineering, Vancouver, Canada, 2014.

Galal, K., and A. Mofidi. Shear Strengthening of RC T-Beams Using Mechanically Anchored Unbonded Dry Carbon Fiber Sheets. In *Journal of Performance of Constructed Facilities, Vol. 24*, 2010, pp. 31-39.

Goebel, J.H.. *Design and Environmental Performance of Near-Surface Mounted Carbon Fiber Reinforced Polymer Strips for Shear Strengthening Reinforced Concrete Bridge Girders*. Thesis, Oregon State University, 2011.

Hassan, T., and S. Rizkalla. Bond Mechanism of NSM FRP Bars for Flexural Strengthening of Concrete Structures. In *ACI Structural Journal, Vol. 101 No. 6*, 2004, pp. 830-839.

Higgins, C., T.H. Miller, D.V. Rosowsky, S.C. Yim, T. Potisuk, T.K. Daniels, B.S. Nicholas, M.J. Robelo, A. Lee, R.W. Forrest. *SPR 350 Assessment Methodology for Diagonally Cracked Reinforced Concrete Deck Girder*. Oregon Department of Transportation. Salem, Oregon, 2005.

Higgins, C., A. Lee, T. Potisuk, and T.K. Forrest. High-Cycle Fatigue of Diagonally Cracked RC Bridge Girders: Laboratory Tests. In *Journal of Bridge Engineering, Vol. 12 No. 2,* 2007, pp. 226-236.

Higgins, C., M.R. Dawson, M.M. Mitchell, G. Sopal, and A.E. Senturk. (2009) *SPR 652 OTREC-RR-09-09, Environmental Durability of Reinforced Concrete Deck Girders Strengthened for Shear with Surface-Bonded Carbon Fiber-Reinforced Polymer, Final Report*. Oregon Department of Transportation Salem, Oregon, May 2009.

"Historical Weather." *Weather Underground* , http://www.wunderground.com/history (May 12, 2016)

Jalali, M., M.K. Sharbatdar, J.F. Chen, and F.J. Alaee. Shear Strengthening of RC Beams Using Innovative Manually Made NSM FRP Bars. In *Construction and Building Materials, Vol. 36*, 2012, pp. 990-1000.

Johnson, B.A. Design and Fatigue Behavior of Near-Surface Mounted CFRP Bars for Shear Strengthening of RC Bridge Girders. Thesis, Oregon State University, 2011.

Khalifa, A., W.J. Gold, A. Nanni, M.I., and A.A. Contribution of Externally Bonded FRP to Shear Capacity of RC Flexural Members. In *Journal of Composites for Construction,* Vol. 2 No. 4, 1998, pp. 195-202.

Khalifa, A. and A. Nanni. Improving Shear Capacity of Existing RC T-Section Beams Using CFRP Composites. In *Cement and Concrete Composites*, Vol. 22, 2000, pp. 165-174.

Miner, M.A. Cumulative Damage in Fatigue. In *ASME Transportation Journal Applied Mechanics*, Vol. 12 No. 3, 1945, pp. 159-164

Mitchell, P.A. *Freeze-Thaw and Sustained Load Durability of Near Surface Mounted FRP Strengthened Concrete*. Thesis, Queen's University, 2010.

Nanni, A., M. Di Ludovico, R. Parretti. Shear Strengthening of a PC Bridge Girder with NSM CFRP Rectangular Bars. In *Advances in Structural Engineering*, Vol. 7 No. 4, 2004, pp. 297-309.

Priestley, M.J N., F. Seible, and G.M. Calvi. *Seismic Design and Retrofit of Bridges*. John Wiley & Sons, 1996.

Rahal, K.N., and H.A. Rumaih. Tests on Reinforced Concrete Beams Strengthened in Shear Using Near Surface Mounted CFRP and Steel Bars. In *Engineering Structures*, Vol. 33, 2011, pp. 53-62.

Sena-Cruz, J., and J.A.O. Barros. Modeling of Bond Between Near-Surface Mounted CFRP Laminate Strips and Concrete. In *Journal of Composites for Construction*, Vol. 8 No. 6, 2004, pp. 519-527.

Sharaky, I.A., L. Torres, M. Baena, and C. Mias. An Experimental Study of Different Factors Affecting the Bond of NSM FRP Bars in Concrete. In *Composite Structures,* Vol. 99, 2013, pp. 350-365.

Soliman, S.M., E. El-Salakway, and B. Benmokrane. Bond Performance of Near-Surface Mounted FRP Bars. In *Journal of Composites for Construction*, Vol. 15, 2011, pp. 103-111

Vavra, E. *Application of Titanium Alloy Bars for Strengthening Reinforced Concrete Bridge Girders in Flexure*. Thesis, Oregon State University, 2016.

Wahab, N., K.A. Soudki, and T. Topper. Bond of Carbon Fibre Reinforced Polymer Rods to Concrete in Near Surface Mounted Application Under Fatigue Loading. Presented at 2nd Canadian Conference on Effective Design of Structures, McMaster University, Hamilton, Ont., Canada, 2008, pp. 195-204

APPENDIX A

A.0 EXPERIMENTAL DATA

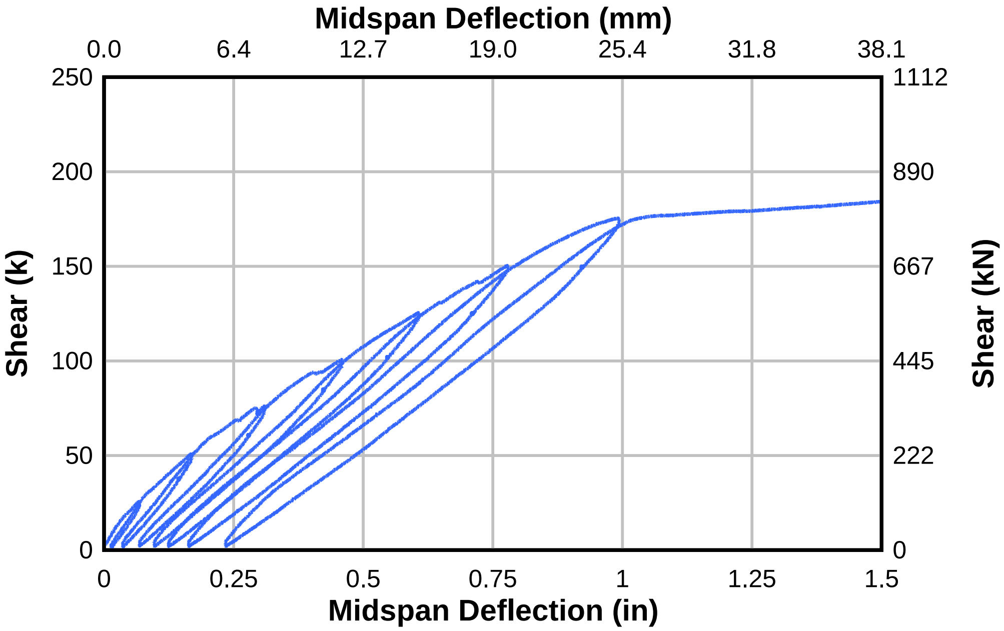

Figure A.1: Specimen T5.24.12.E1 midspan deflection

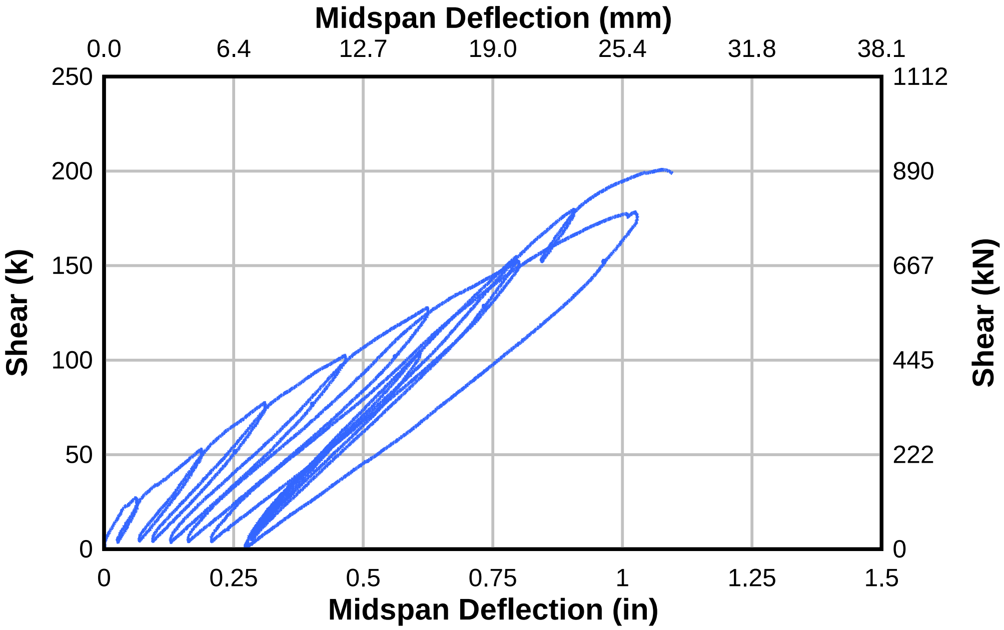

Figure A.2: Specimen T5.24.12S.E1* midspan deflection

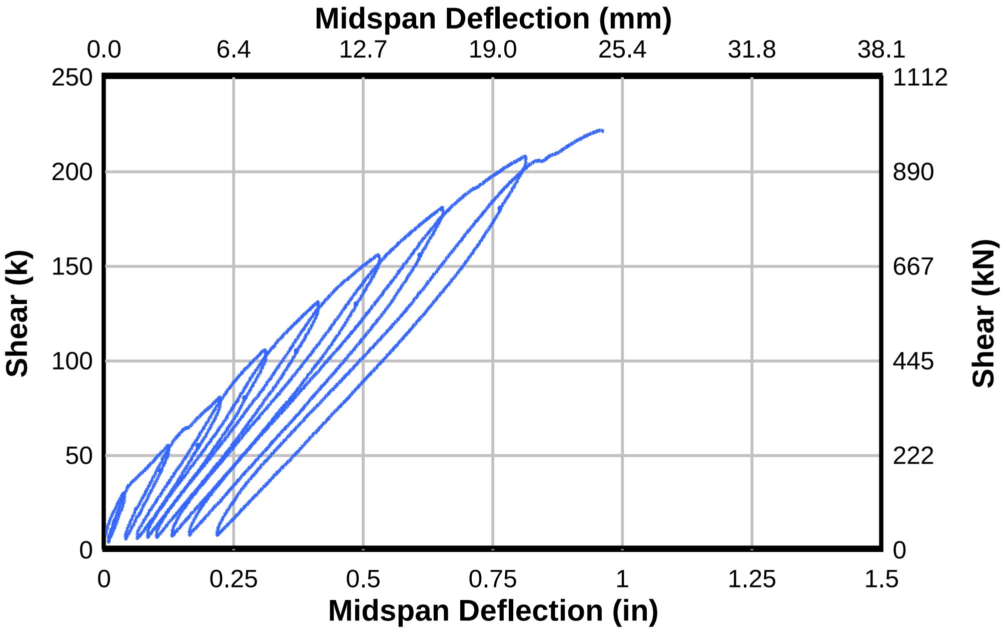

Figure A.3: Specimen IT6.18.18.E1 midspan deflection

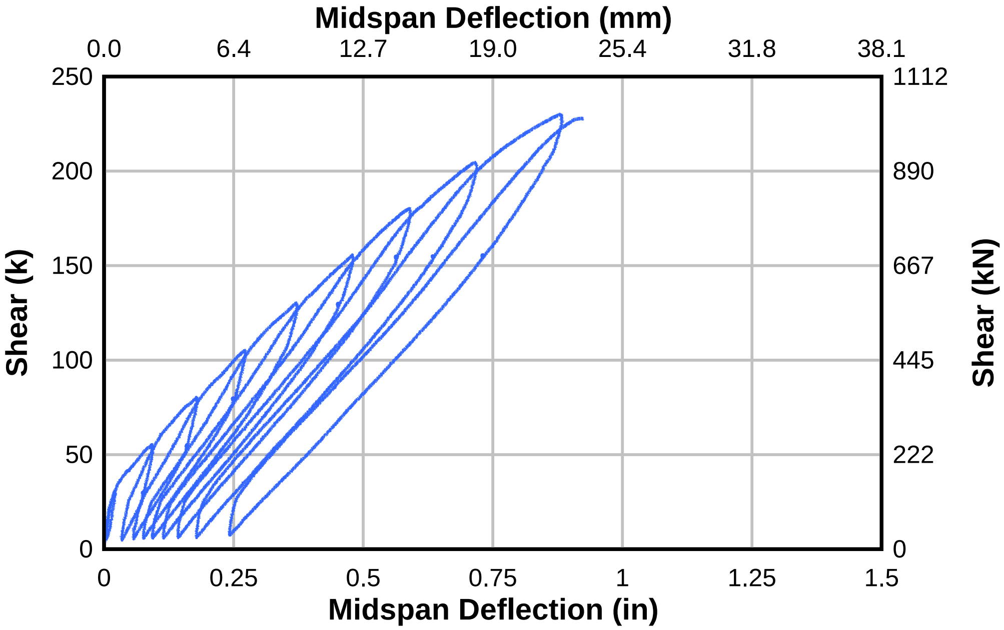

Figure A.4: Specimen IT6.18.12.E1 midspan deflection

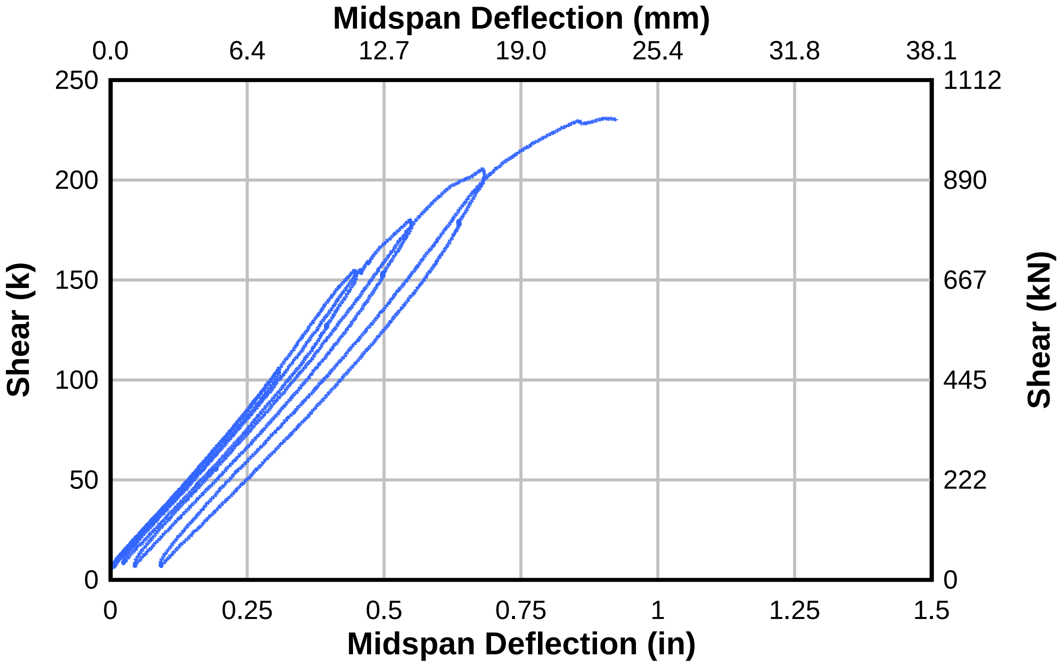

Figure A.5: Specimen IT6.18.12.E1.FTG midspan deflection

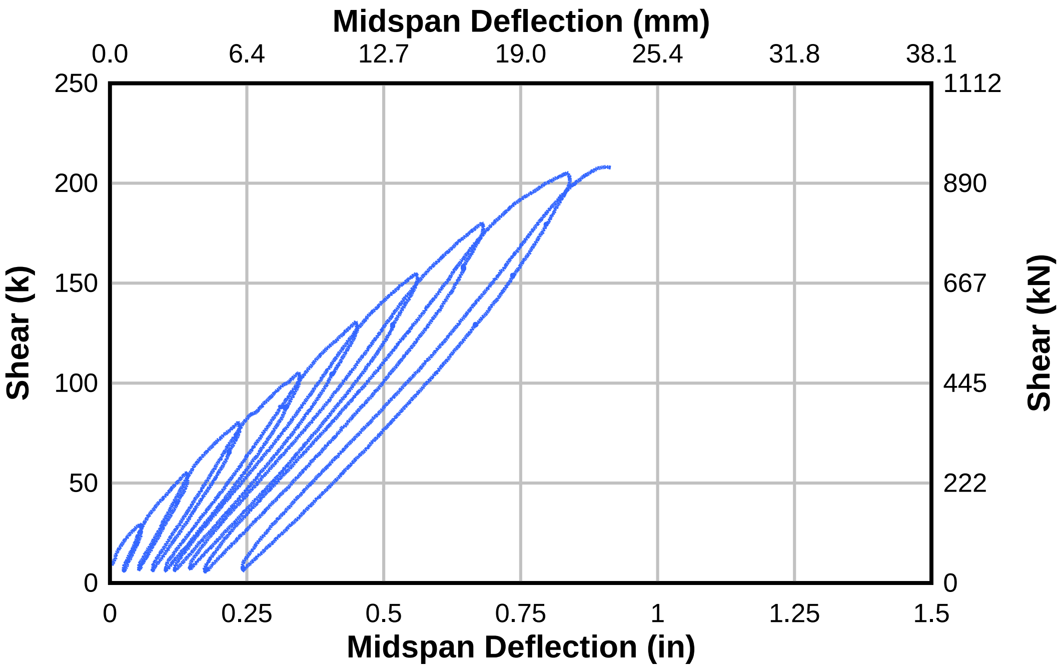

Figure A.6: Specimen IT6.18.12.E2 midspan deflection

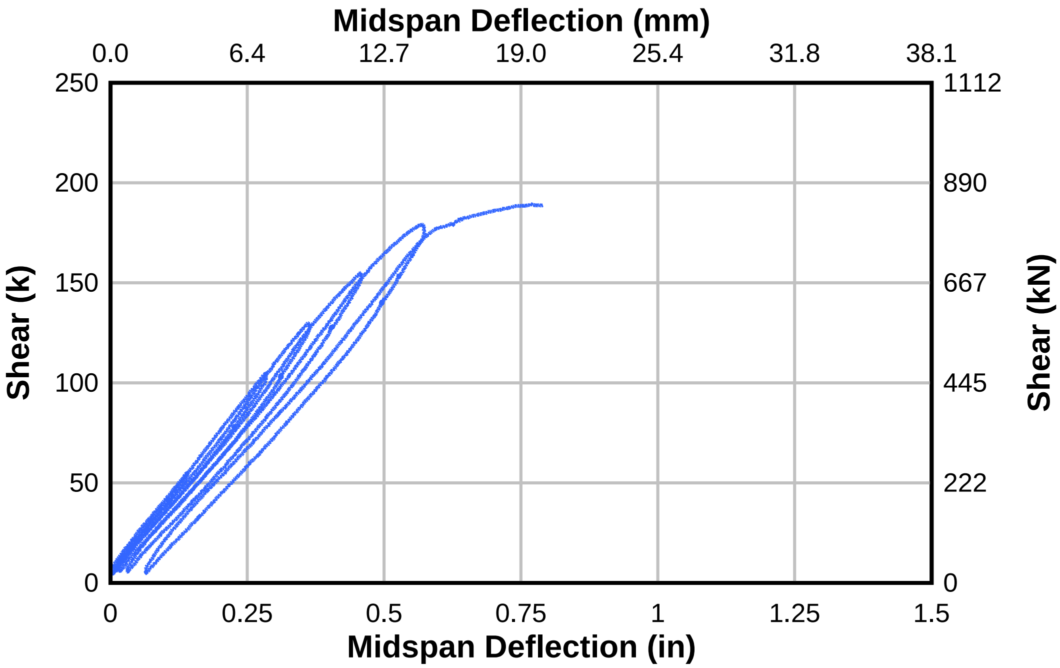

Figure A.7: Specimen IT6.18.12.E2.FTG midspan deflection

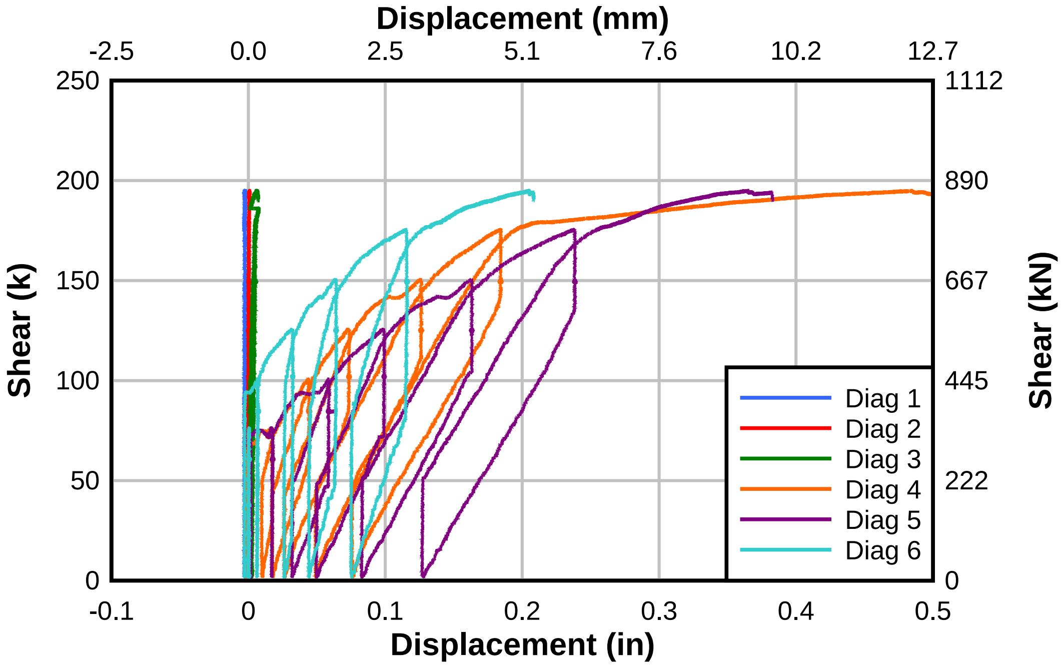

Figure A.8: Specimen T5.24.12.E1 diagonal sensor displacement

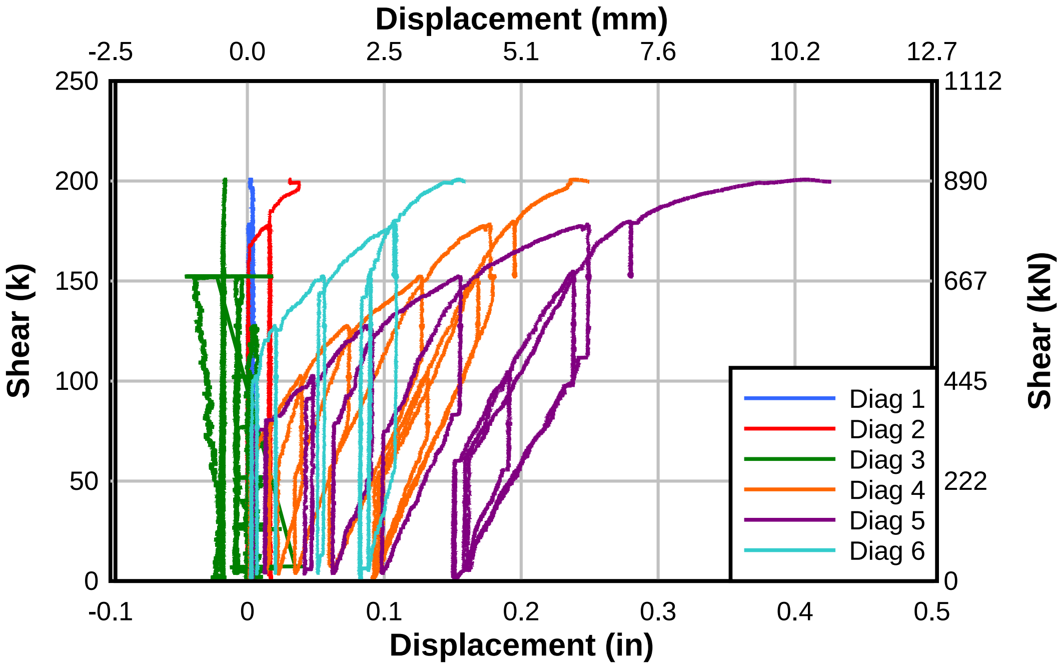

Figure A.9: Specimen T5.24.12S.E1* diagonal sensor displacement

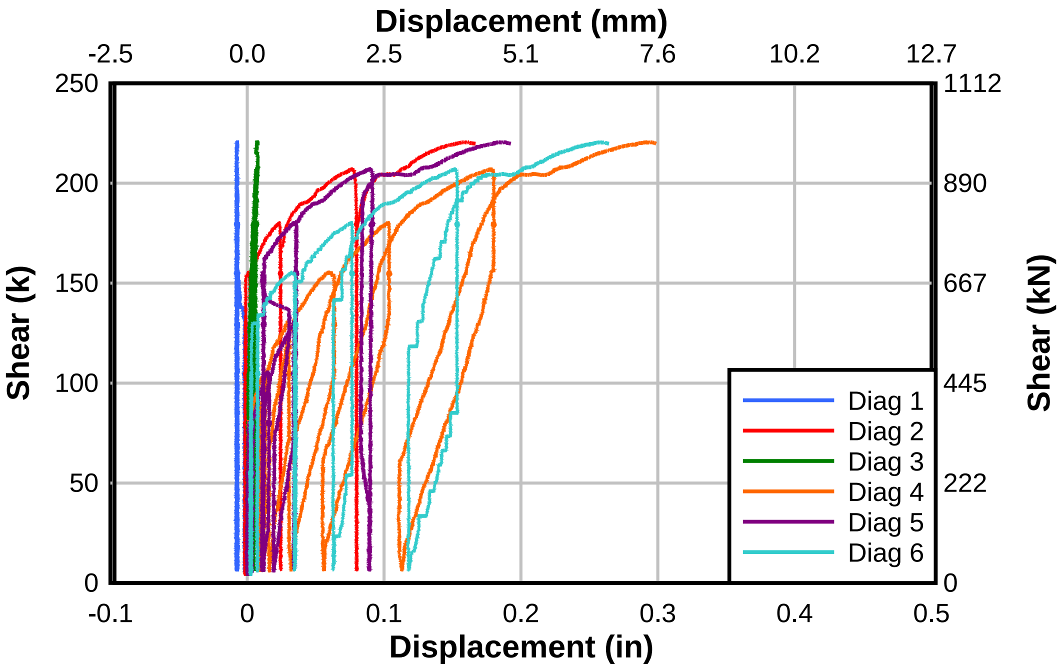

Figure A.10: Specimen IT6.18.18.E1 diagonal sensor displacement

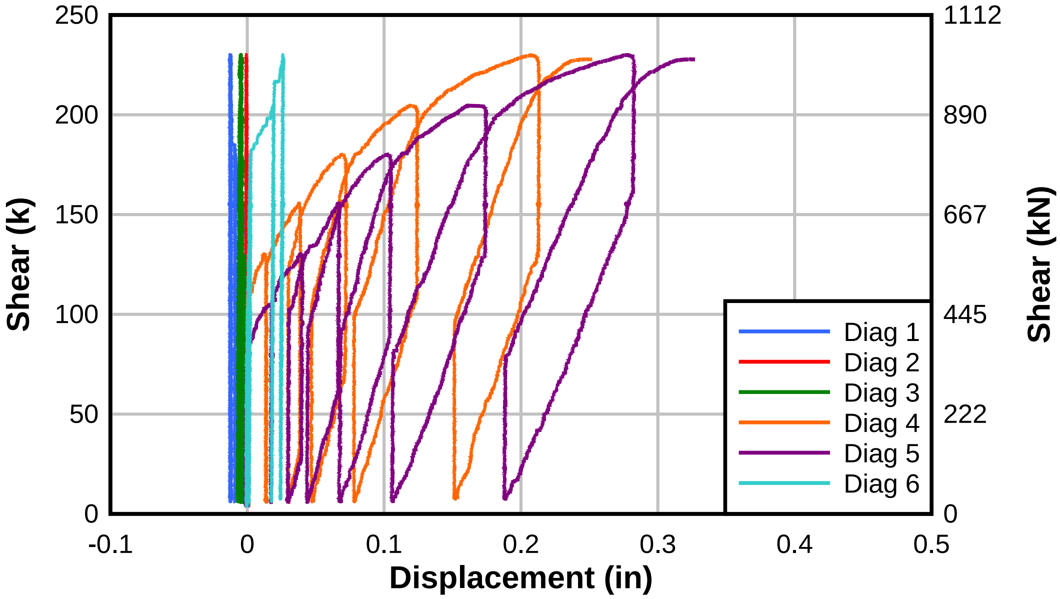

Figure A.11: Specimen IT6.18.12.E1 diagonal sensor displacement

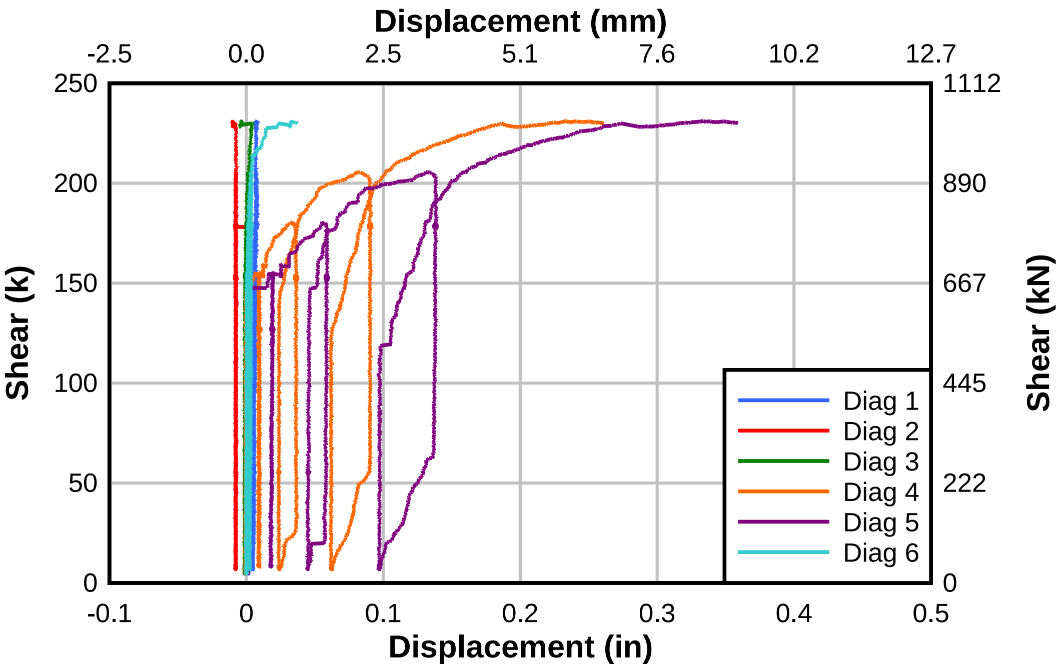

Figure A.12: Specimen IT6.18.12.E1.FTG diagonal sensor displacement

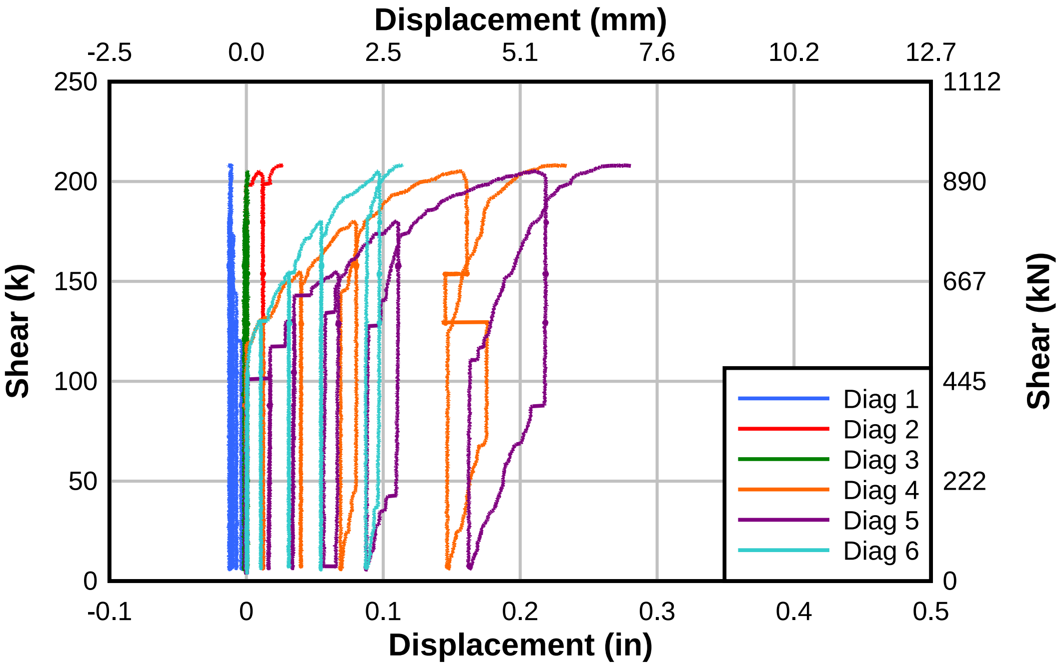

Figure A.13: Specimen IT6.18.12.E2 diagonal sensor displacement

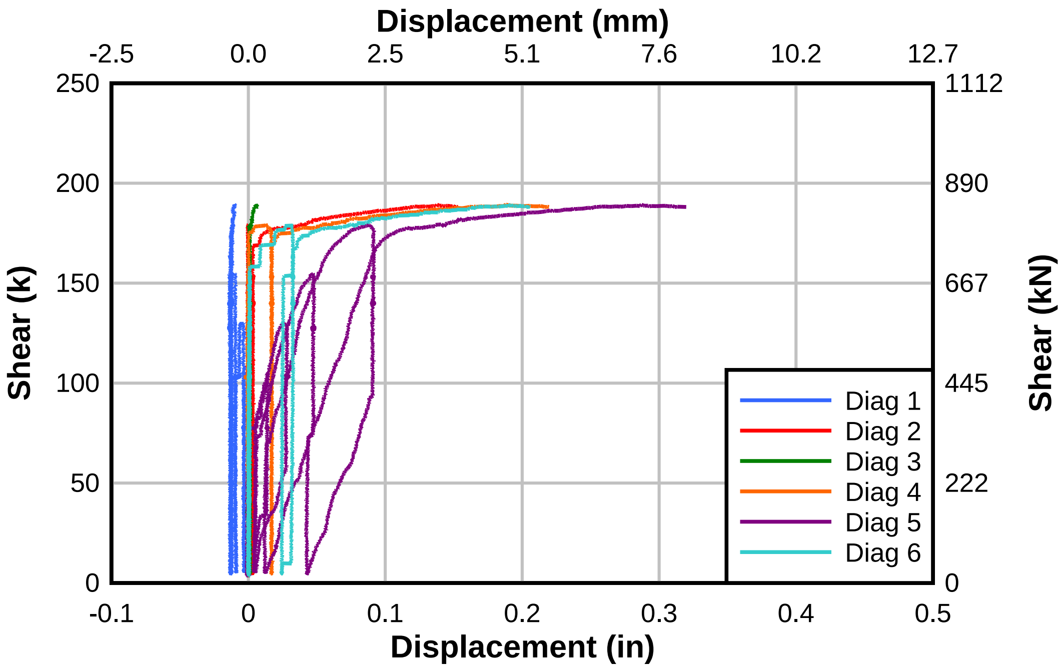

Figure A.14: Specimen IT6.18.12.E2.FTG diagonal sensor displacement

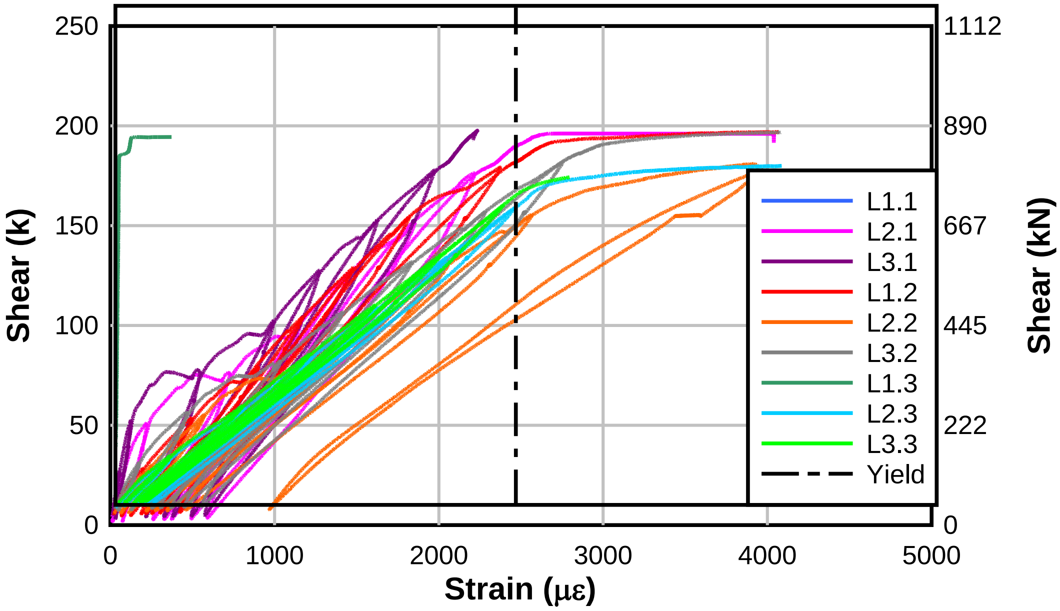

Figure A.15: Specimen T5.24.12.E1 longitudinal strain

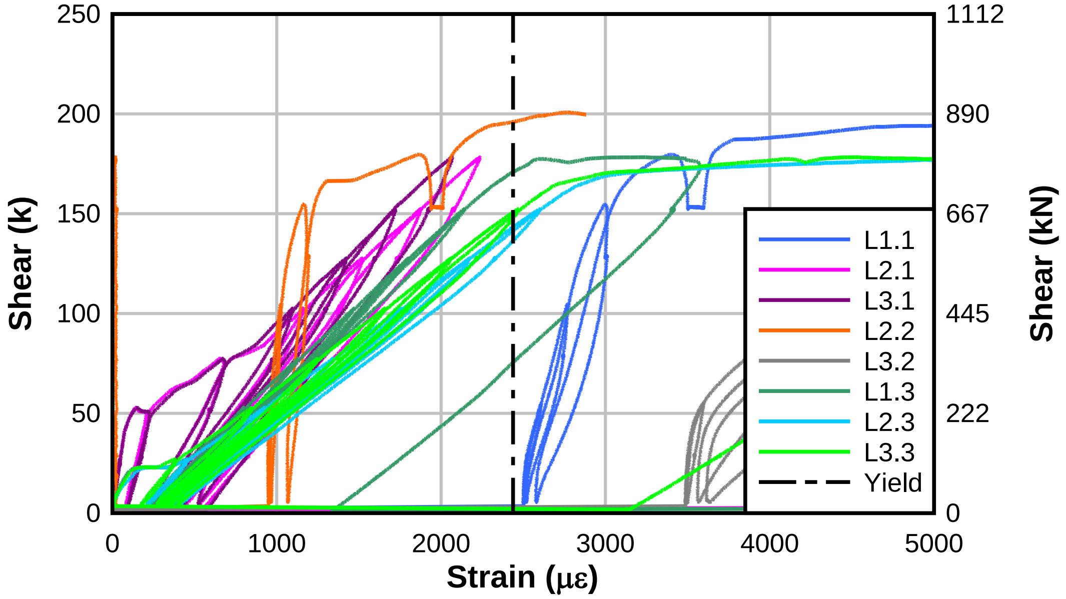

Figure A.16: Specimen T5.24.12S.E1* longitudinal strain

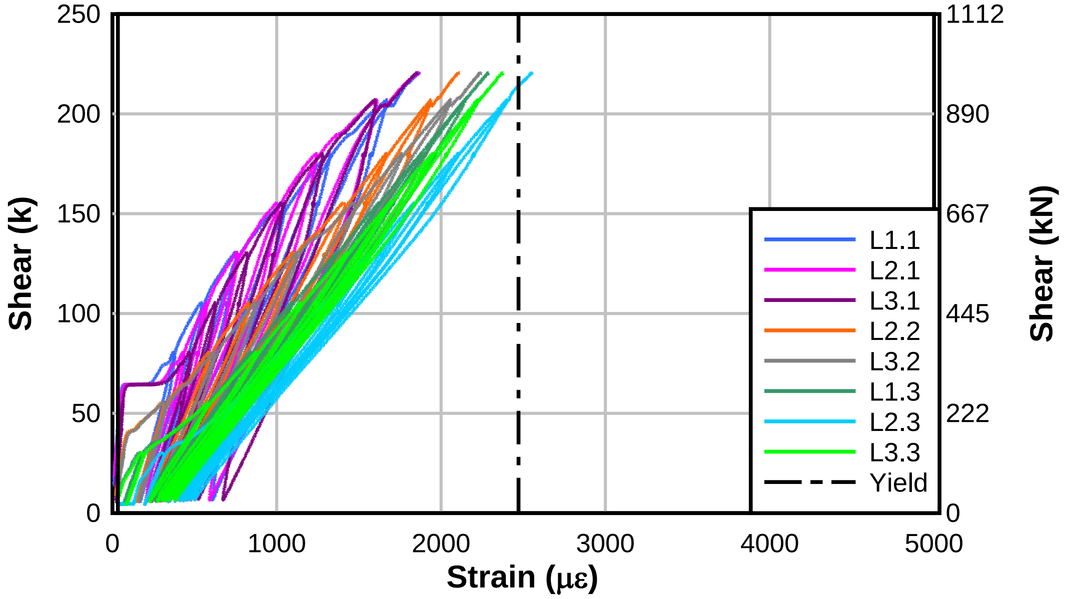

Figure A.17: Specimen IT6.18.18.E1 longitudinal strain

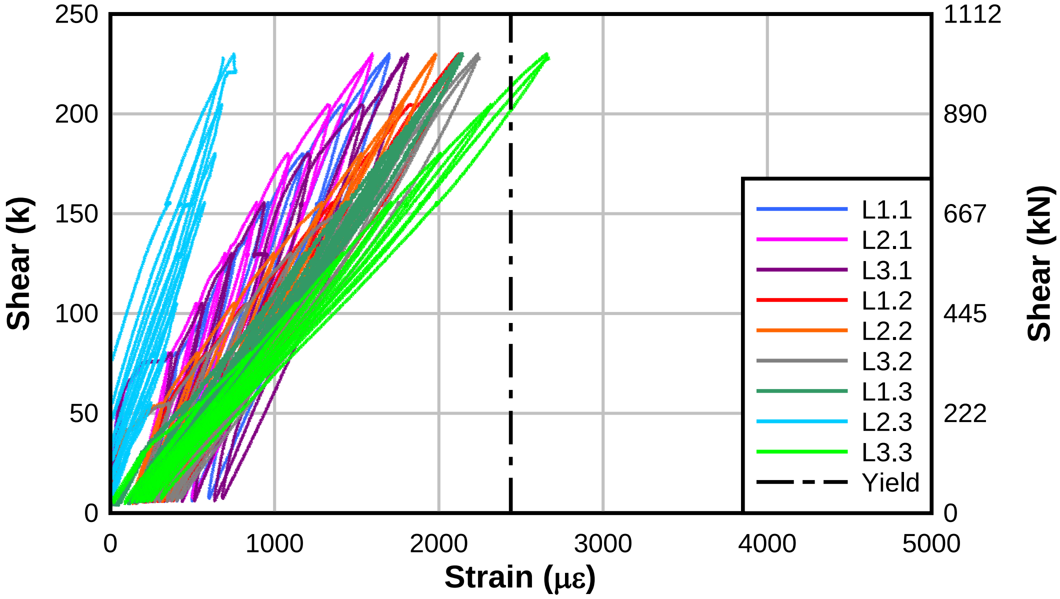

Figure A.18: Specimen IT6.18.12.E1 longitudinal strain

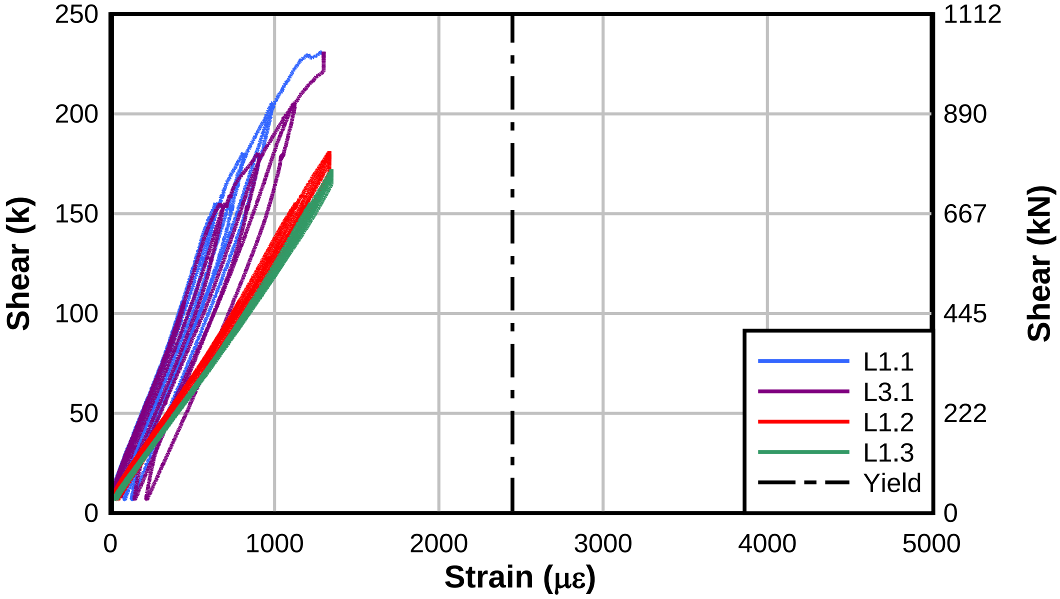

Figure A.19: Specimen IT6.18.12.E1.FTG longitudinal strain

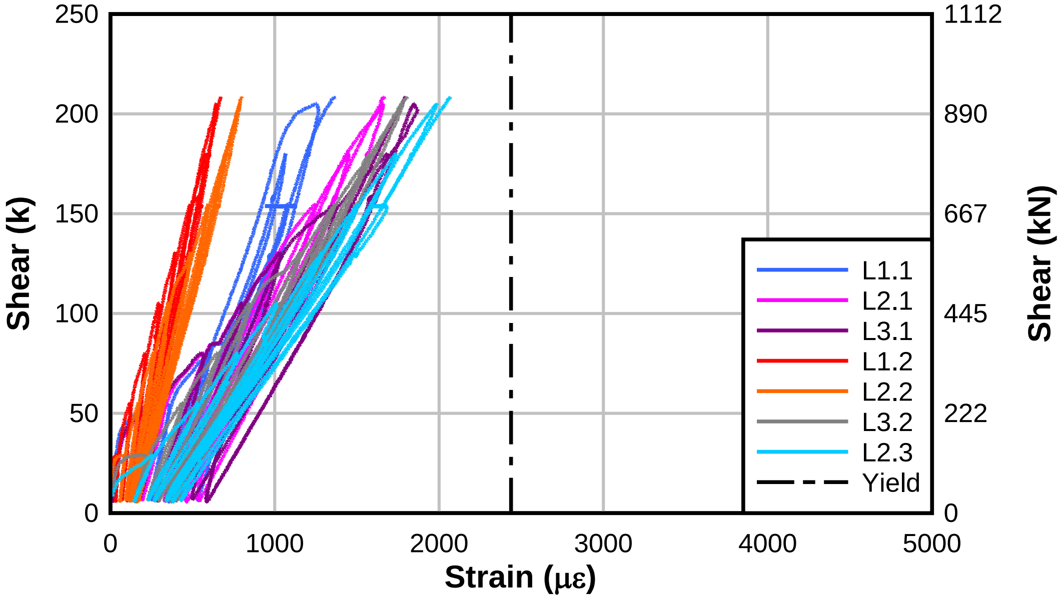

Figure A.20: Specimen IT6.18.12.E2 longitudinal strain

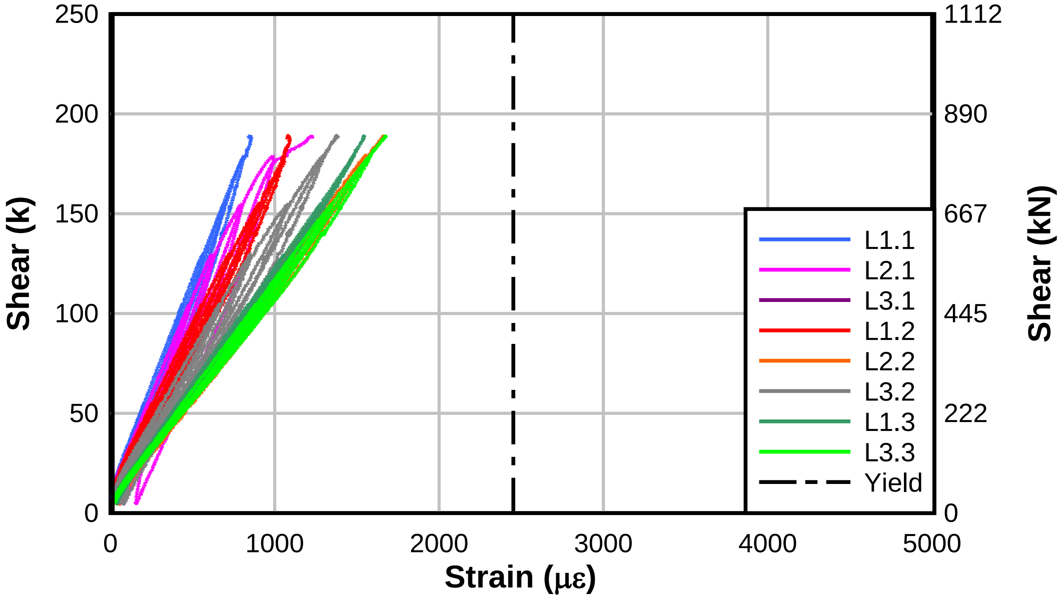

Figure A.21: Specimen IT6.18.12.E2.FTG longitudinal strain

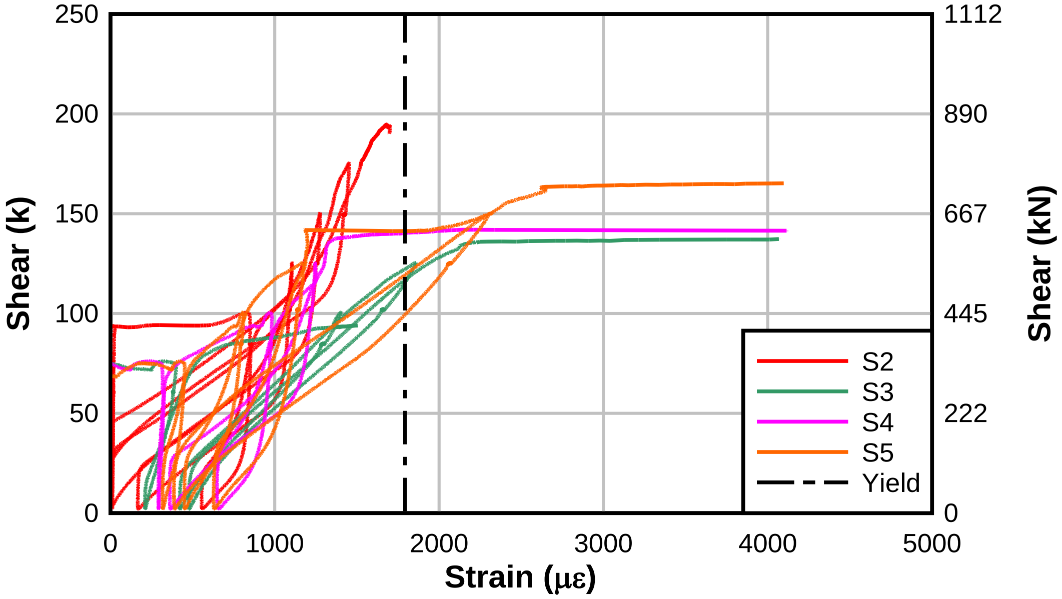

Figure A.22: Specimen T5.24.12.E1 internal stirrup strain

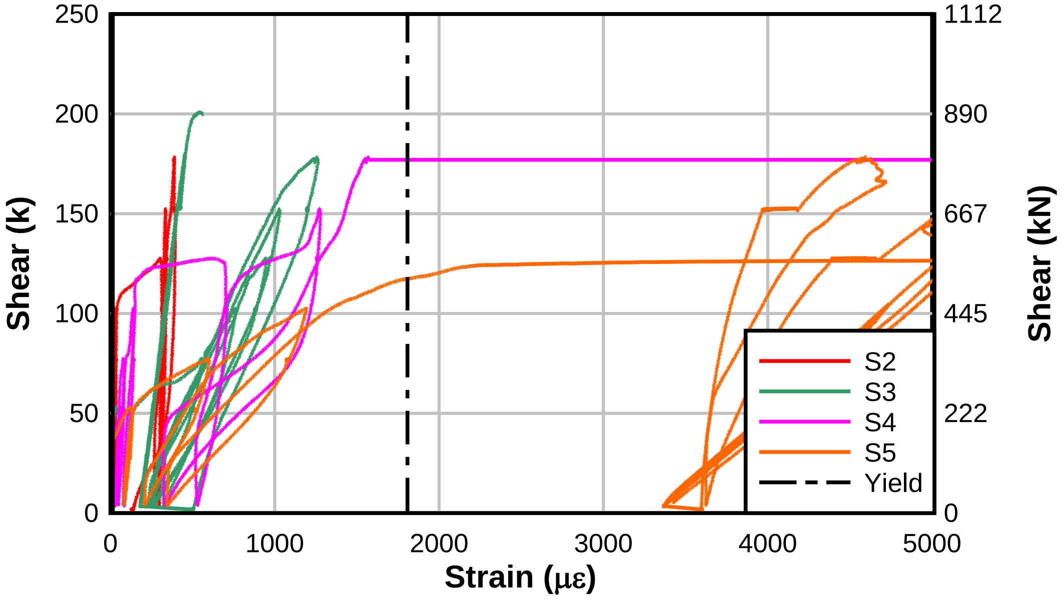

Figure A.23: Specimen T5.24.12S.E1* internal stirrup strain

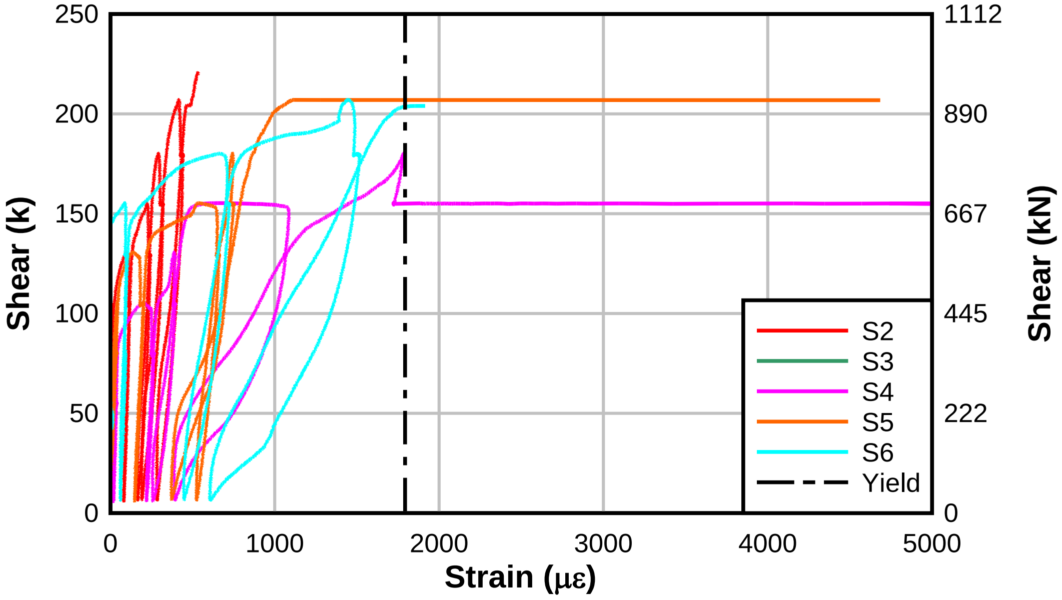

Figure A.24: Specimen IT6.18.18.E1 internal stirrup strain

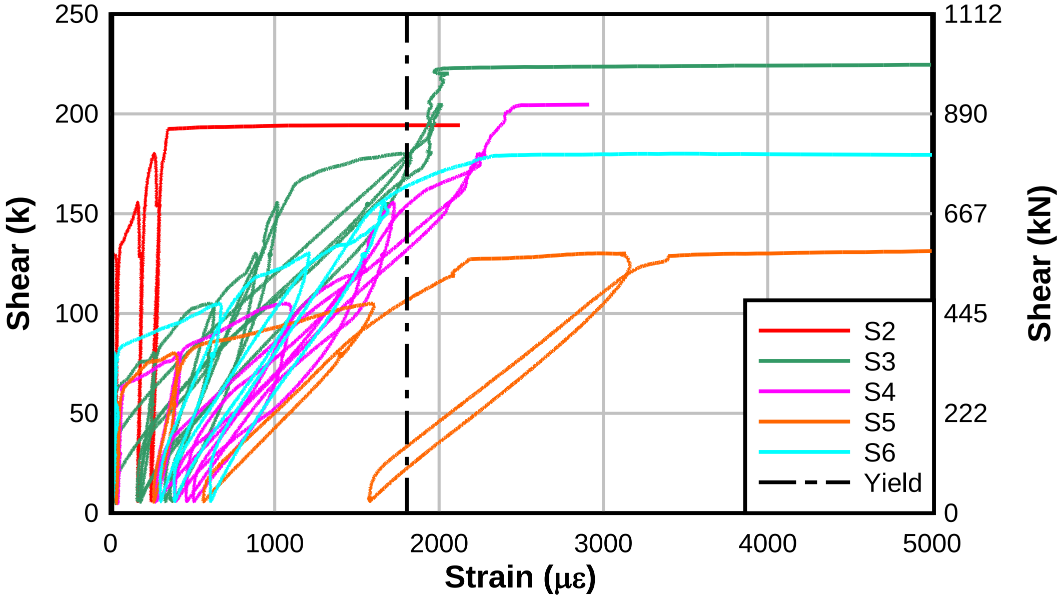

Figure A.25: Specimen IT6.18.12.E1 internal stirrup strain

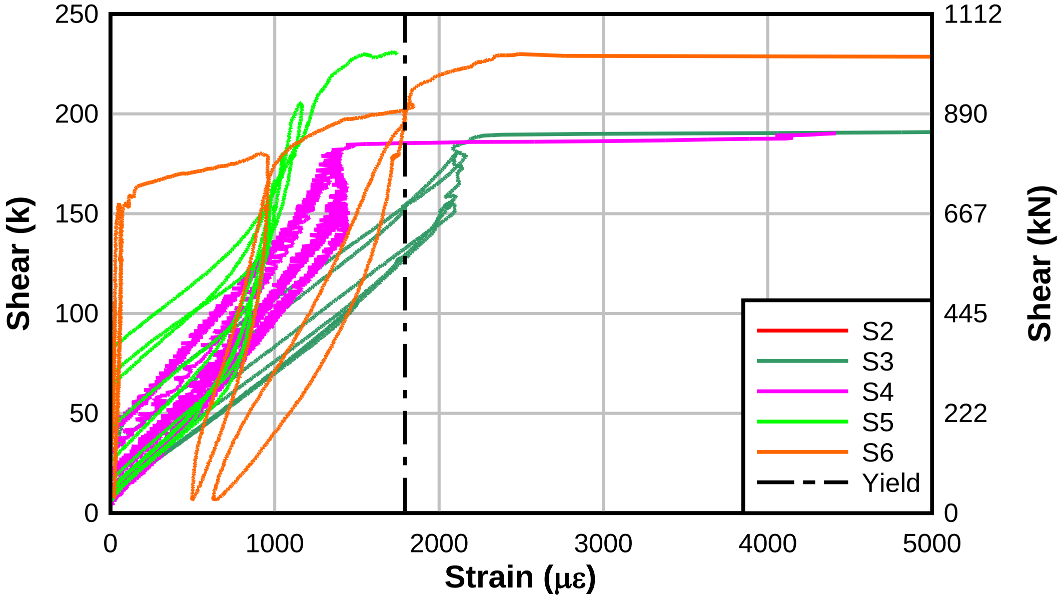

Figure A.26: Specimen IT6.18.12.E1.FTG internal stirrup strain

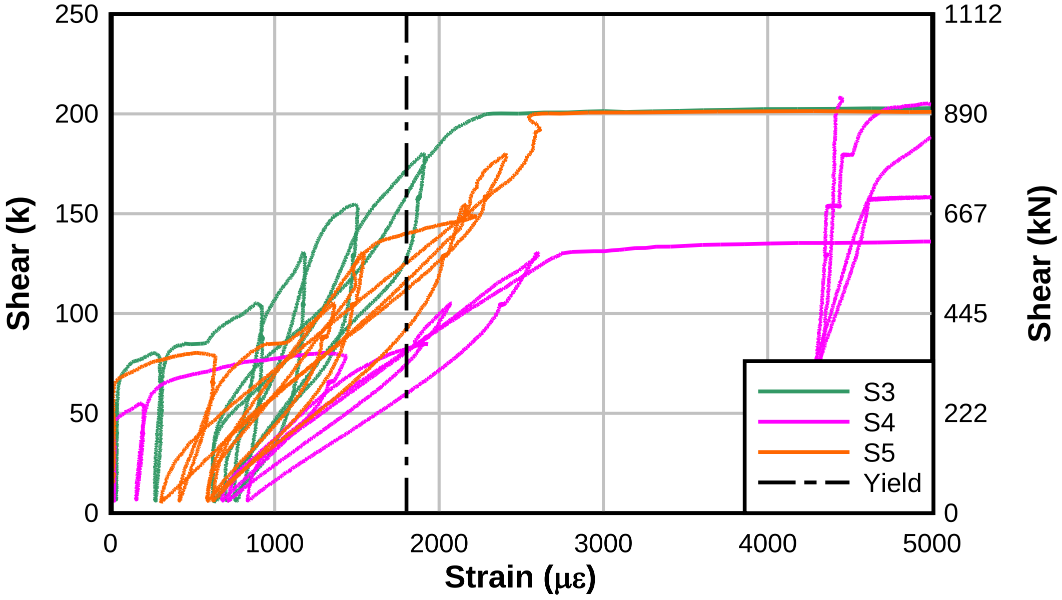

Figure A.27: Specimen IT6.18.12.E2 internal stirrup strain

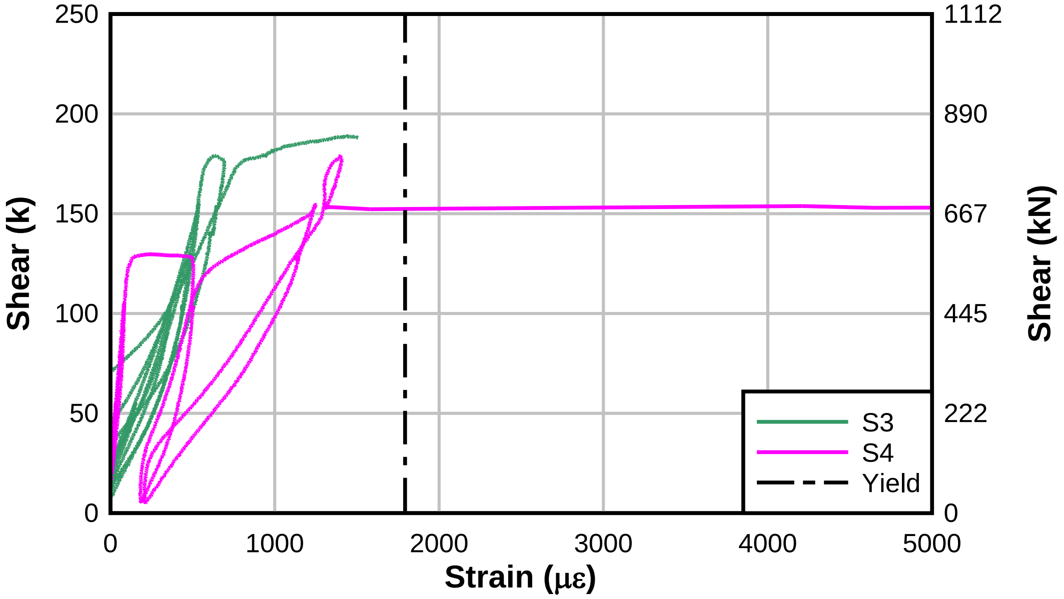

Figure A.28: Specimen IT6.18.12.E2.FTG internal stirrup strain

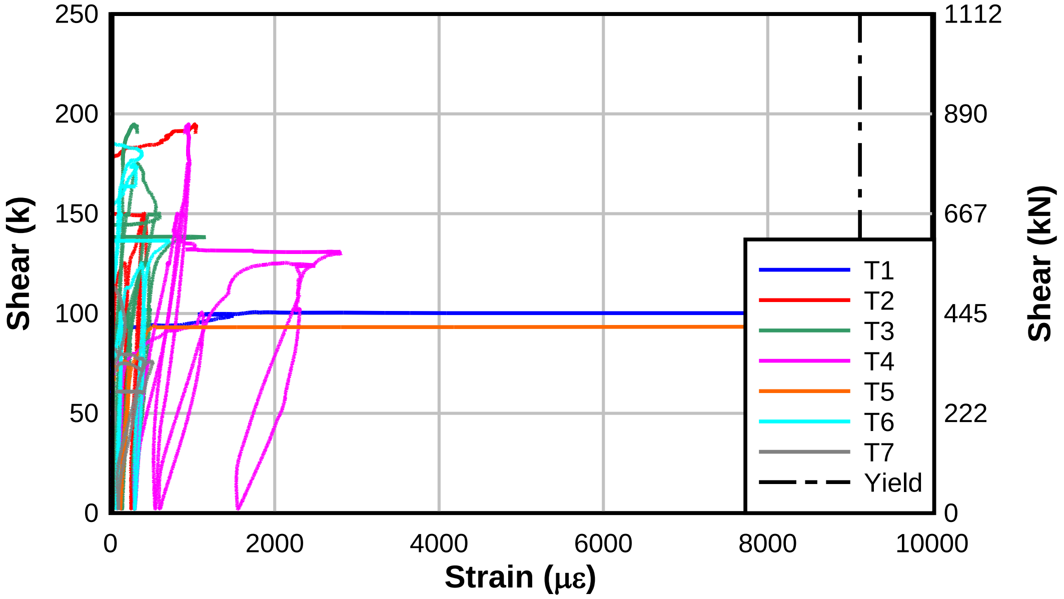

Figure A.29: Specimen T5.24.12.E1 titanium strain

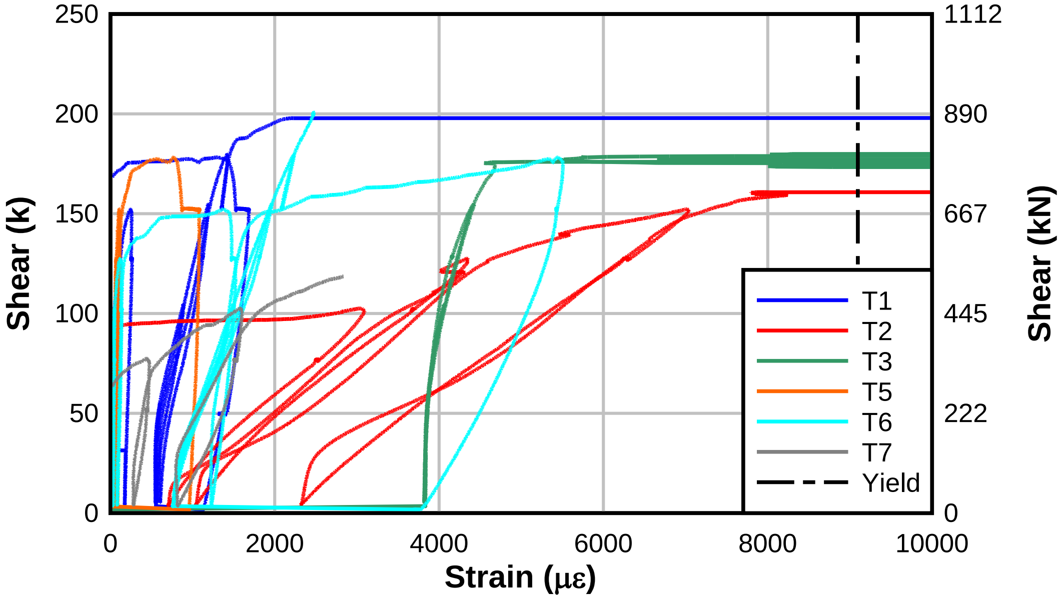

Figure A.30: Specimen T5.24.12S.E1* titanium strain

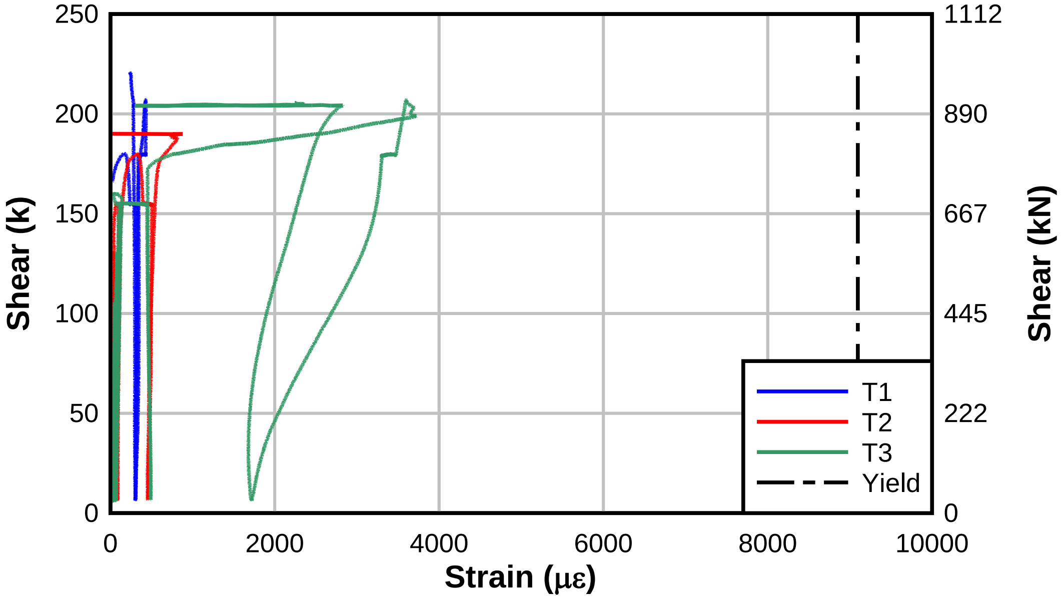

Figure A.31: Specimen IT6.18.18.E1 titanium strain

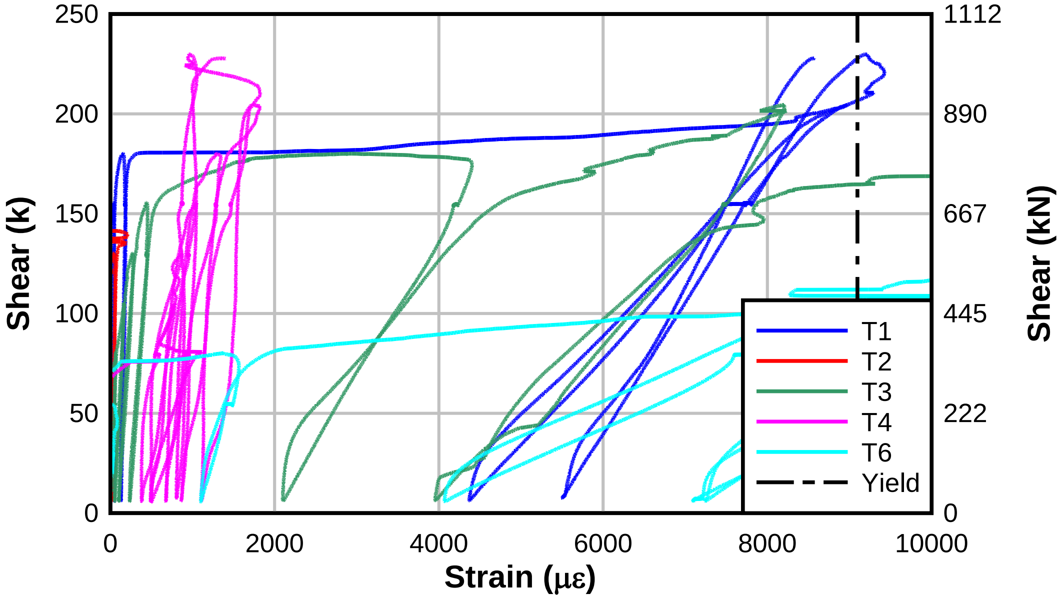

Figure A.32: Specimen IT6.18.12.E1 titanium strain

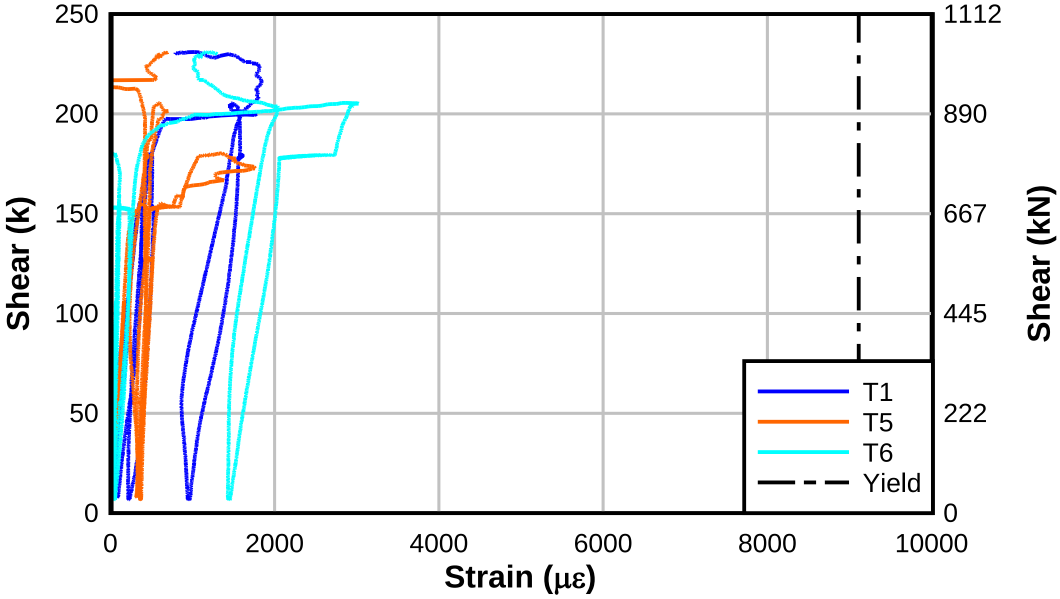

Figure A.33: Specimen IT6.18.12.E1.FTG titanium strain

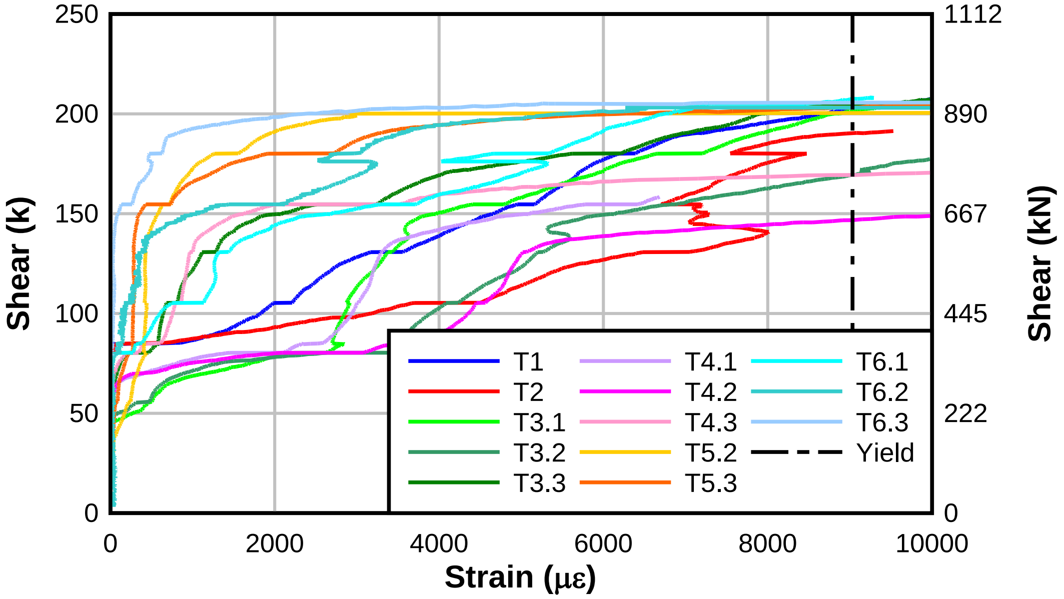

Figure A.34: Specimen IT6.18.12.E2 titanium strain – backbone curves

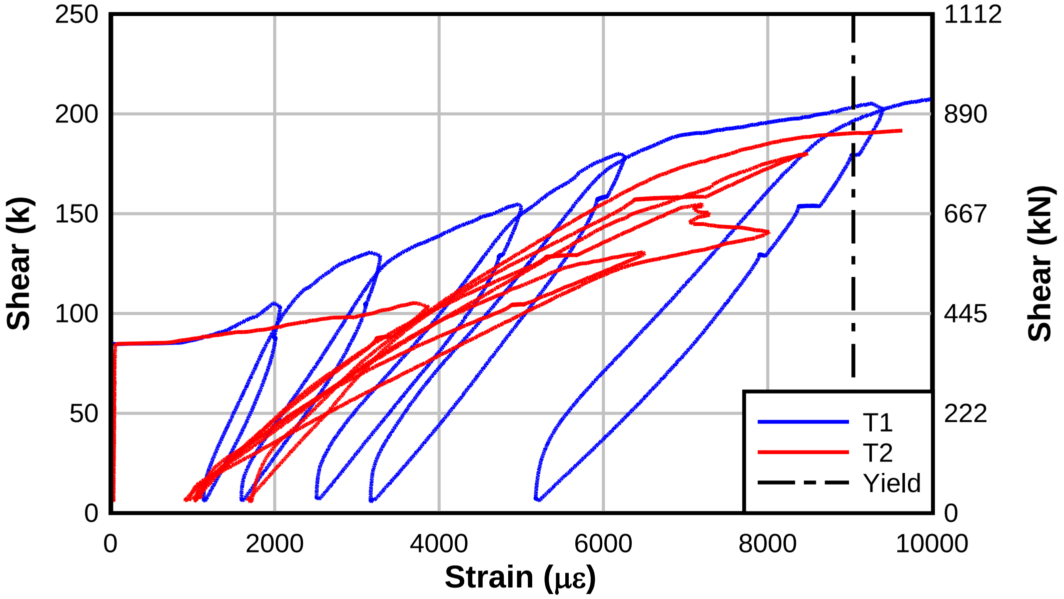

Figure A.35: Specimen IT6.18.12.E2 titanium strain – T1 and T2

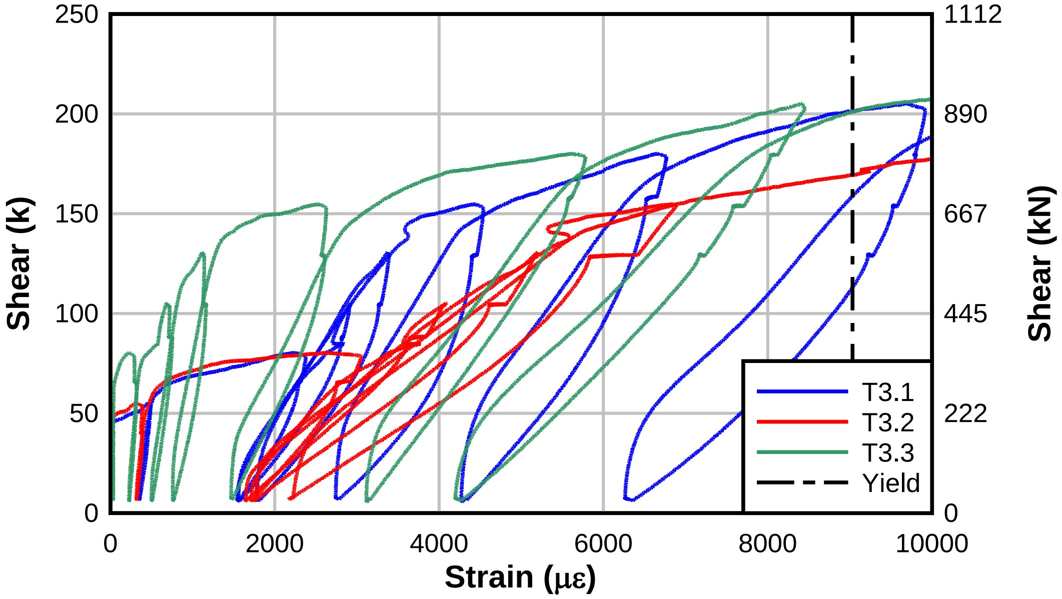

Figure A.36: Specimen IT6.18.12.E2 titanium strain – T3

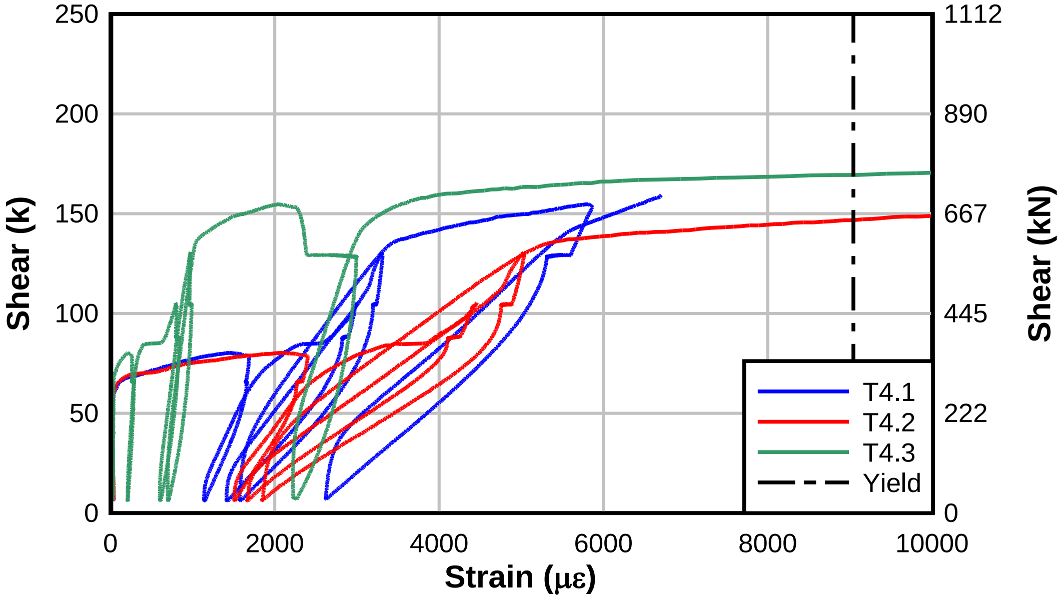

Figure A.37: Specimen IT6.18.12.E2 titanium strain – T4

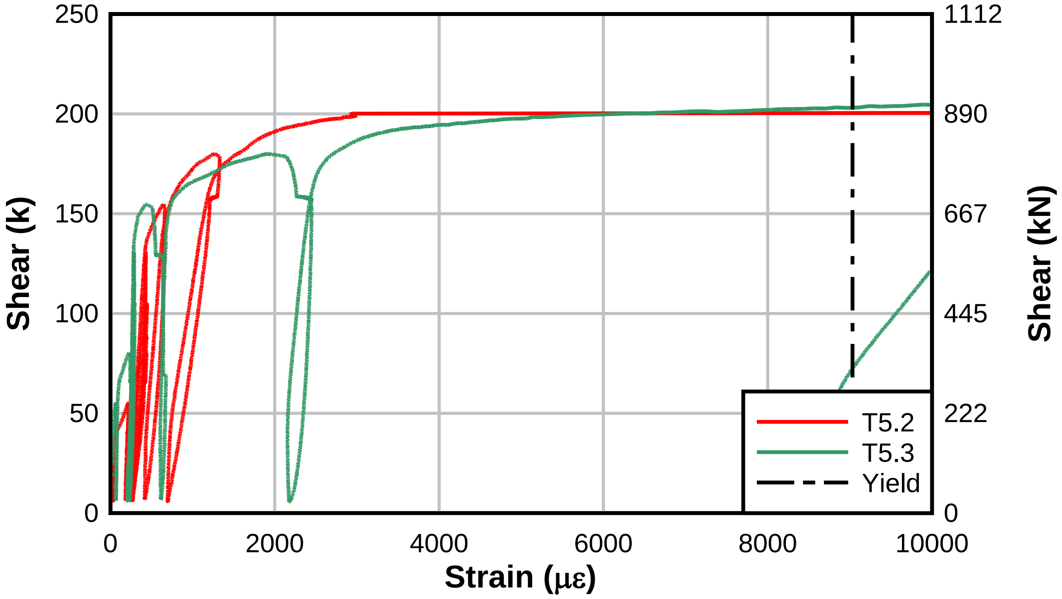

Figure A.38: Specimen IT6.18.12.E2 titanium strain – T5

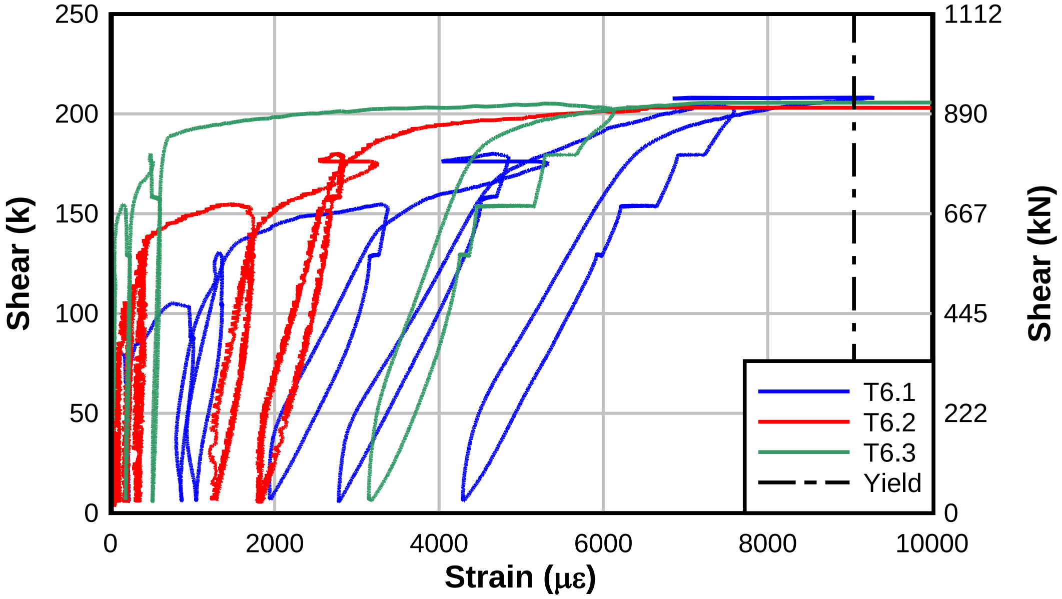

Figure A.39: Specimen IT6.18.12.E2 titanium strain – T6

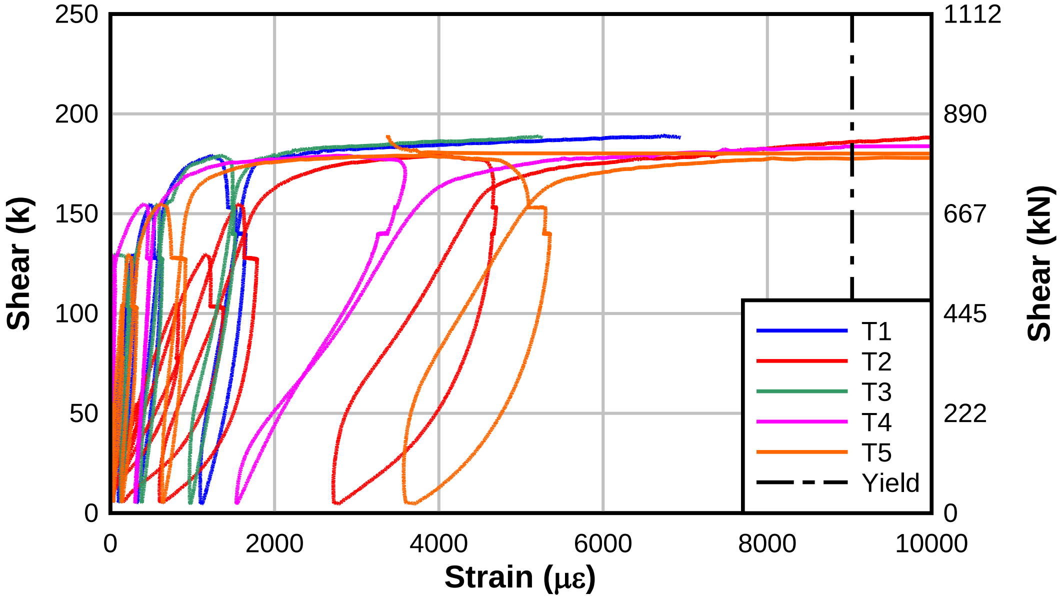

Figure A.40: Specimen IT6.18.12.E2.FTG titanium strain

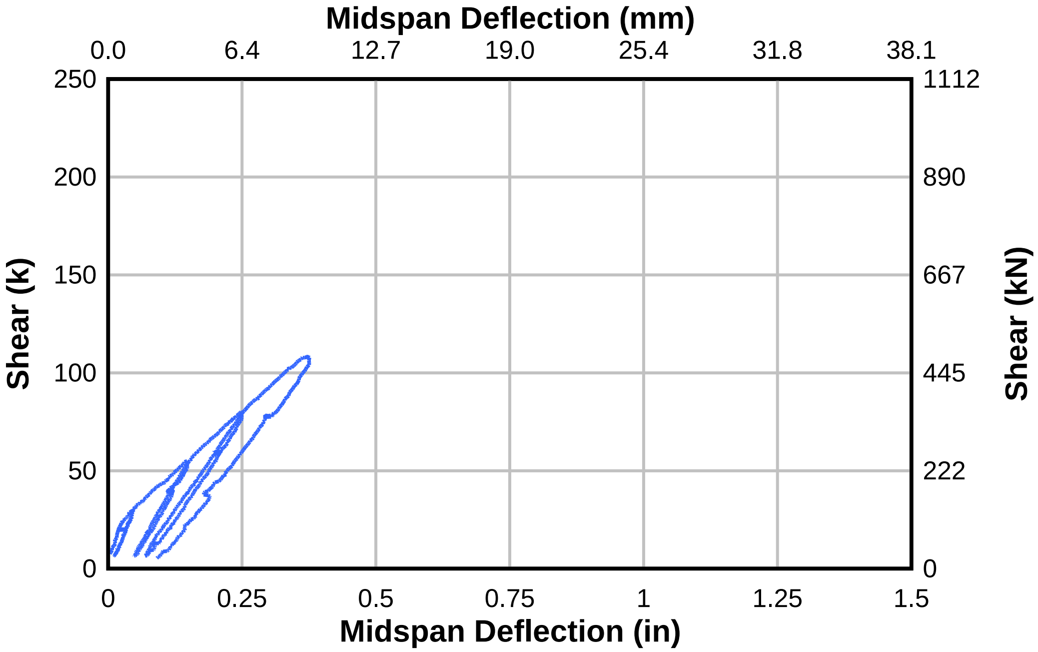

Figure A.41: Specimen IT6.18.12.E1.FTG midspan deflection 1st freezer loading

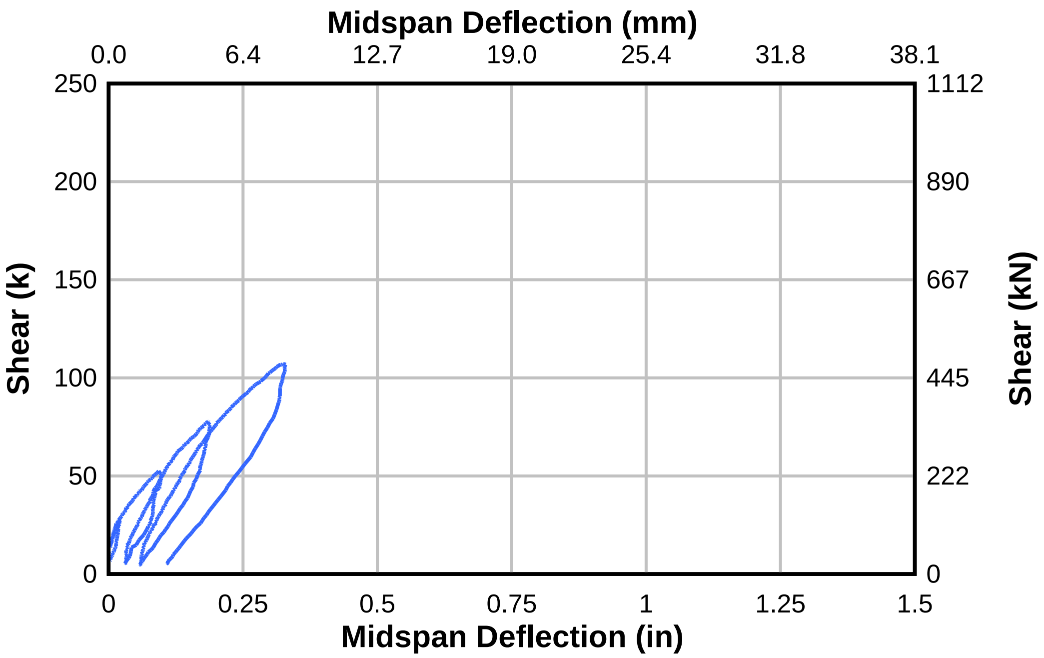

Figure A.42: Specimen IT6.18.12.E2.FTG midspan deflection first freezer loading

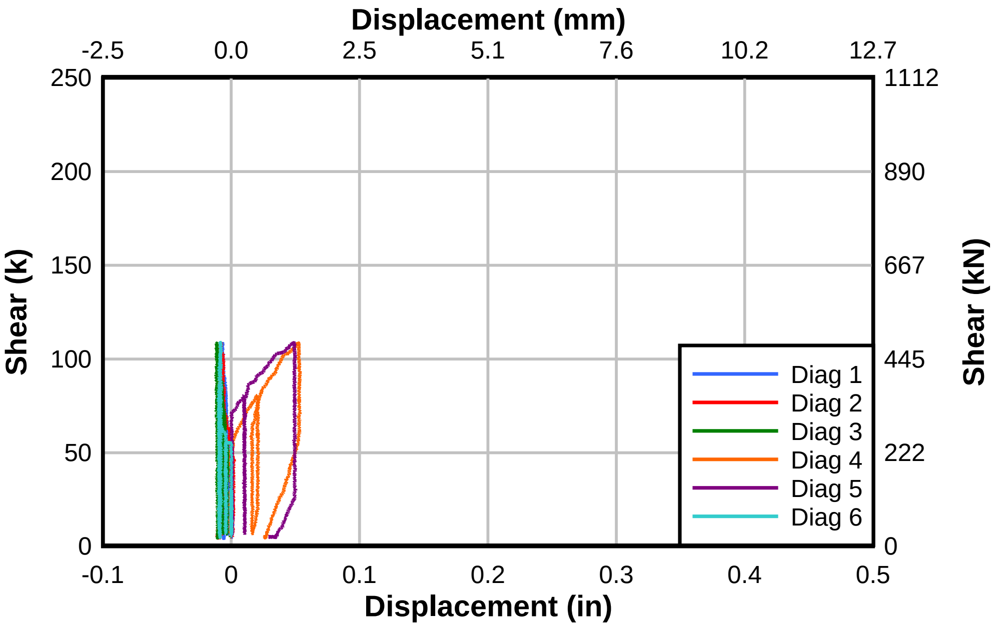

Figure A.43: Specimen IT6.18.12.E1.FTG diagonal disp. first freezer loading

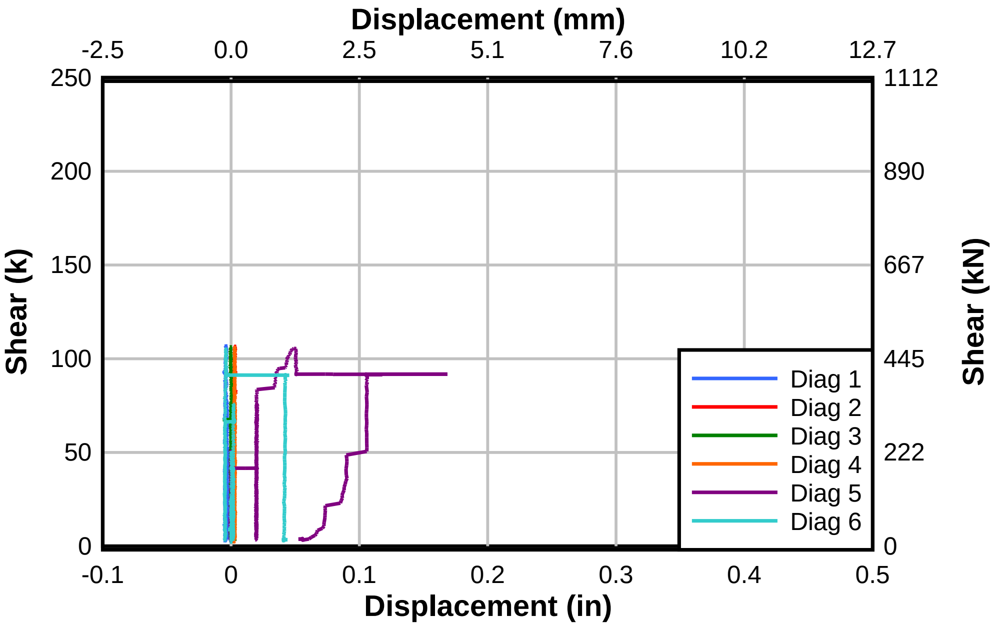

Figure A.44: Specimen IT6.18.12.E2.FTG diagonal disp. first freezer loading

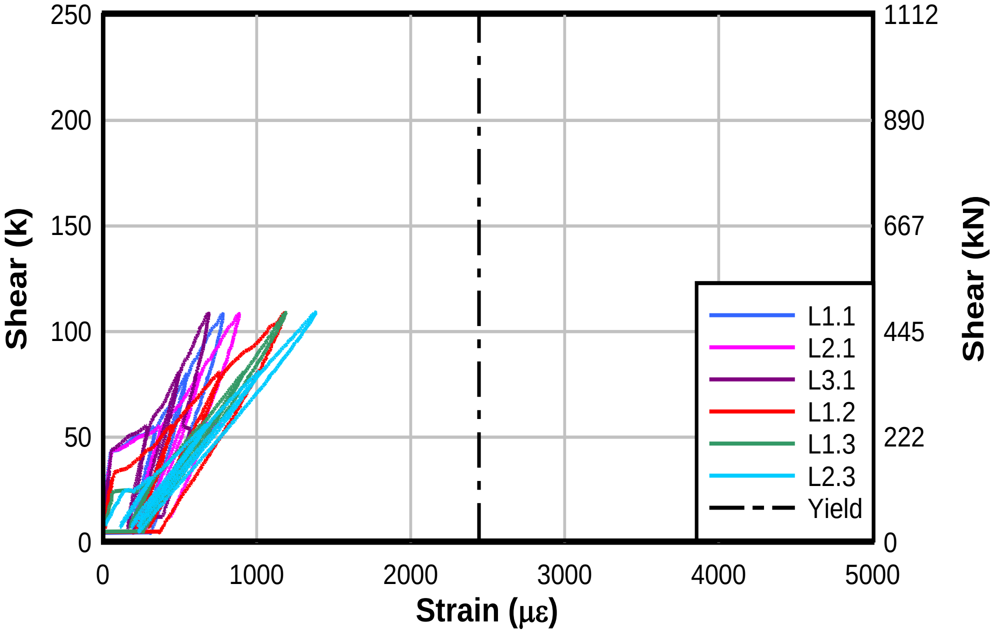

Figure A.45: Specimen IT6.18.12.E1.FTG longitudinal strain first freezer loading

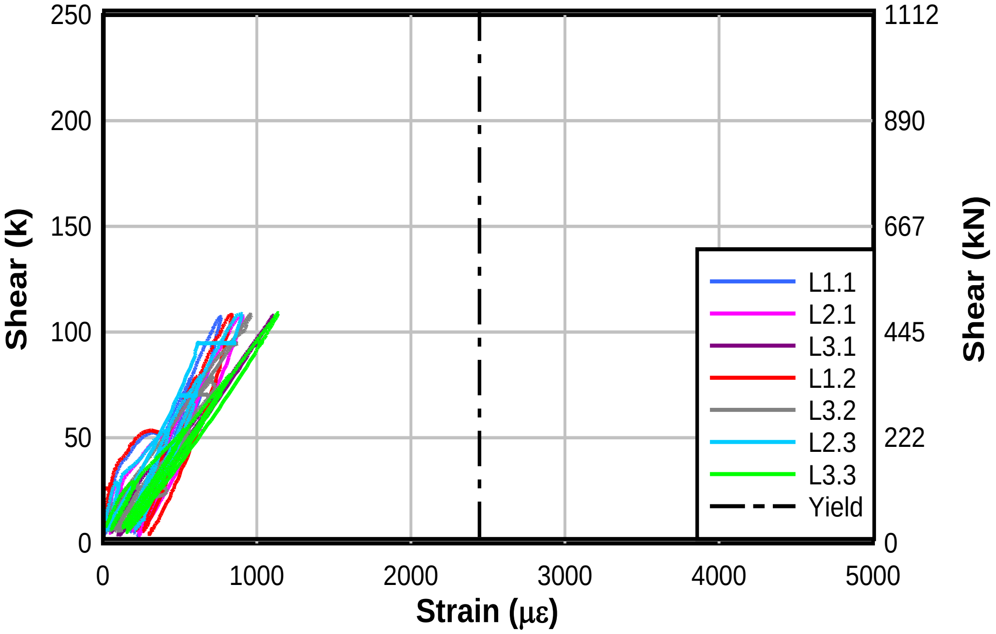

Figure A.46: Specimen IT6.18.12.E2.FTG longitudinal strain first freezer loading

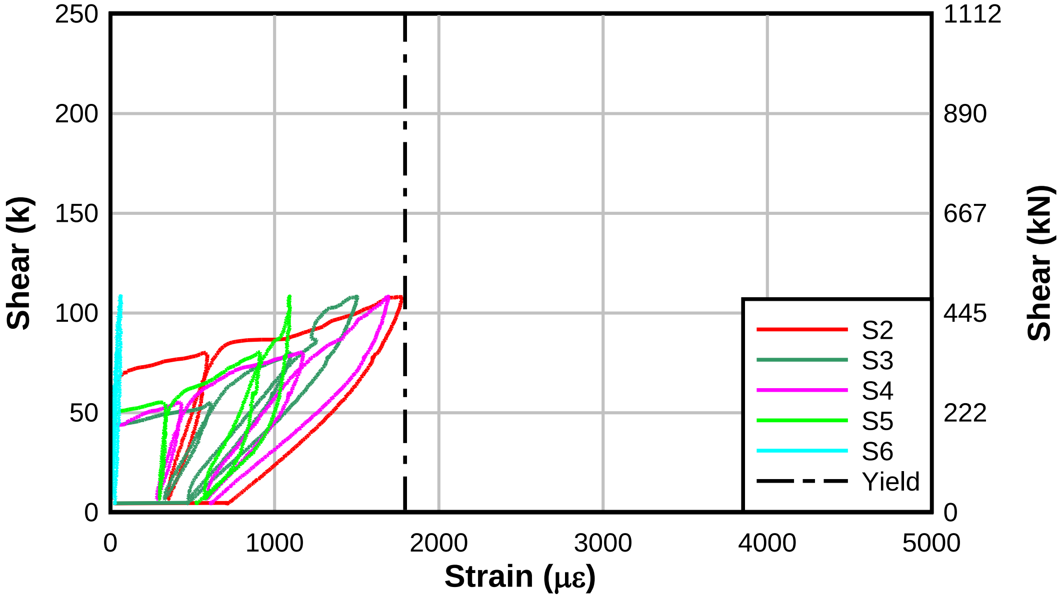

Figure A.47: Specimen IT6.18.12.E1.FTG internal stirrup strain first freezer loading

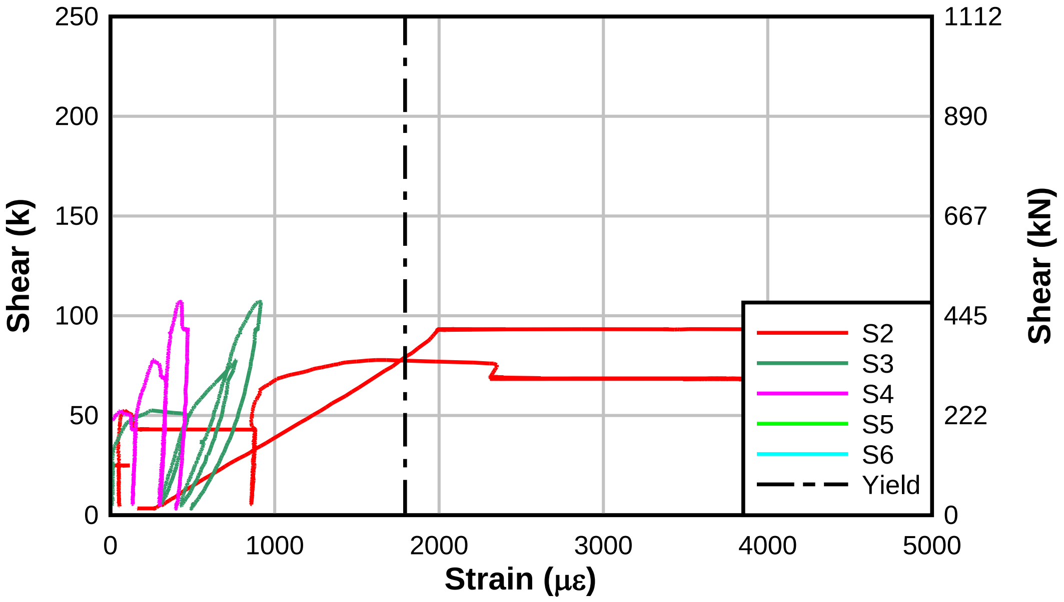

Figure A.48: Specimen IT6.18.12.E2.FTG internal stirrup strain first freezer loading

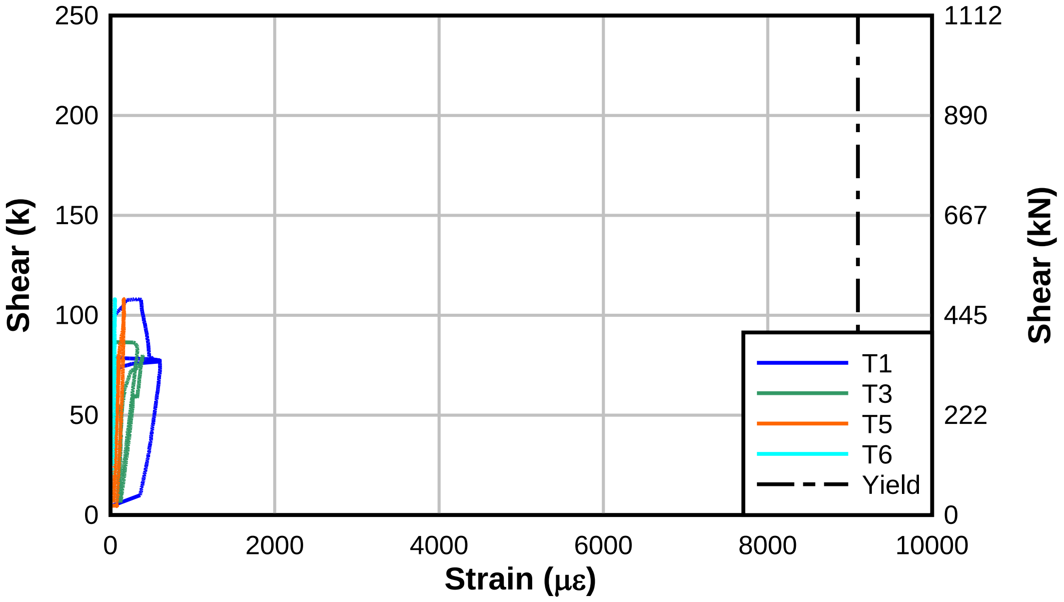

Figure A.49: Specimen IT6.18.12.E1.FTG titanium strain first freezer loading

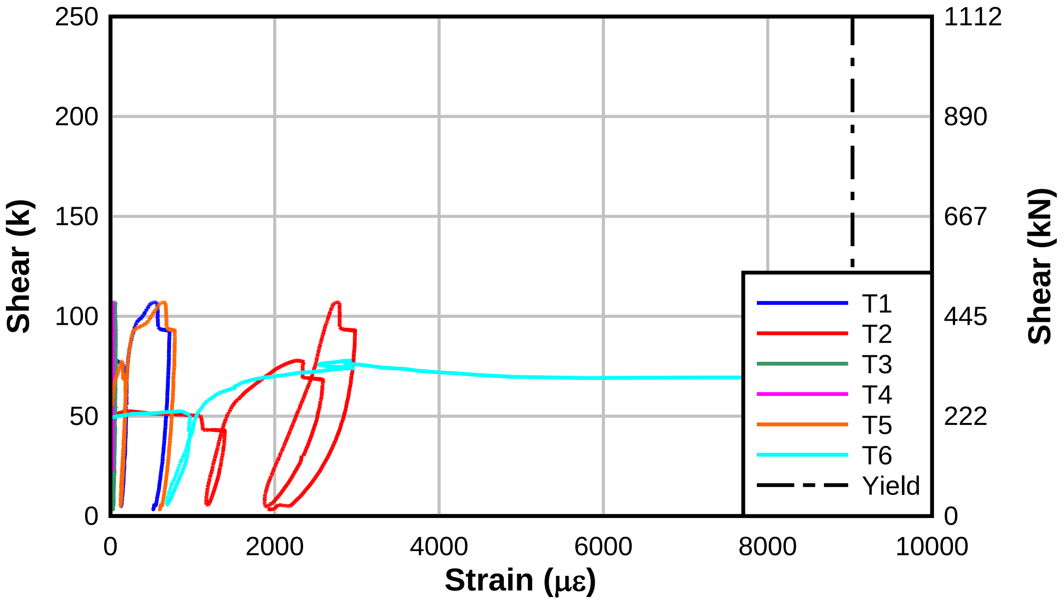

Figure A.50: Specimen IT6.18.12.E2.FTG titanium strain first freezer loading

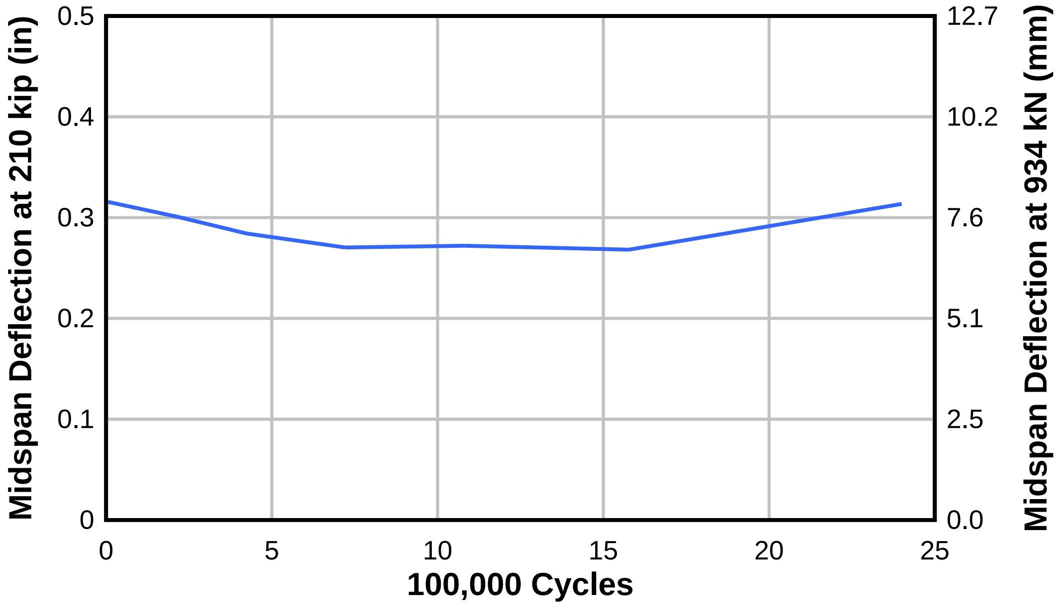

Figure A.51: Specimen IT6.18.12.E1.FTG fatigue midspan deflection

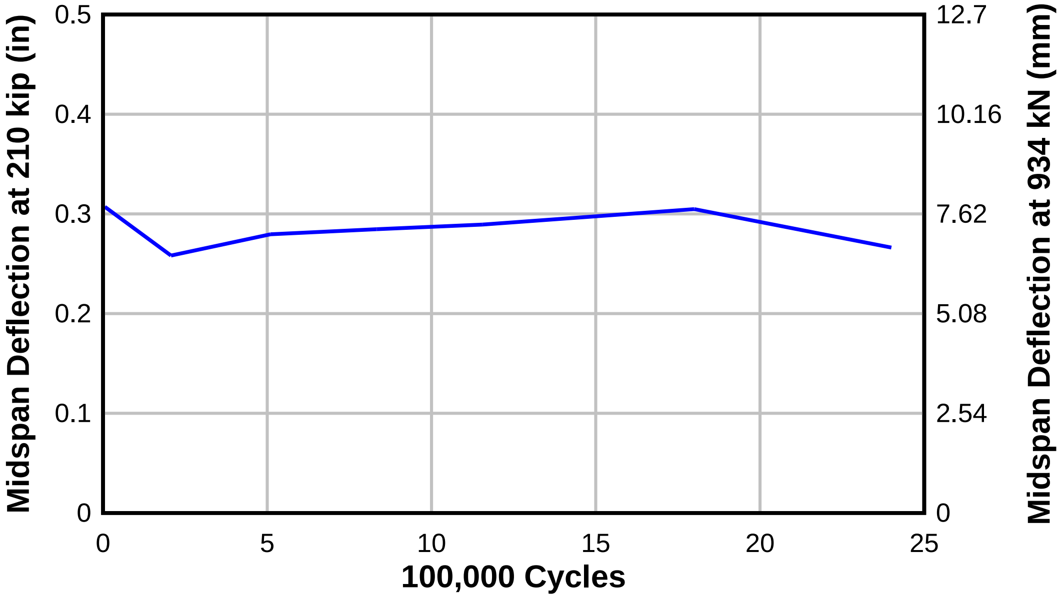

Figure A.52: Specimen IT6.18.12.E2.FTG fatigue midspan deflection

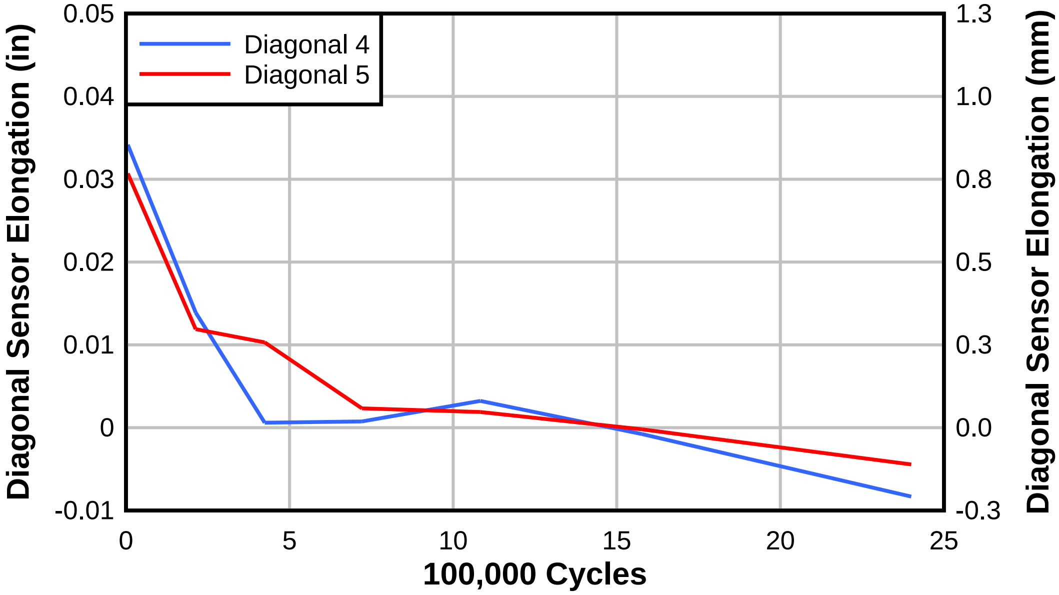

Figure A.53: Specimen IT6.18.12.E1.FTG fatigue diagonal sensor elongation

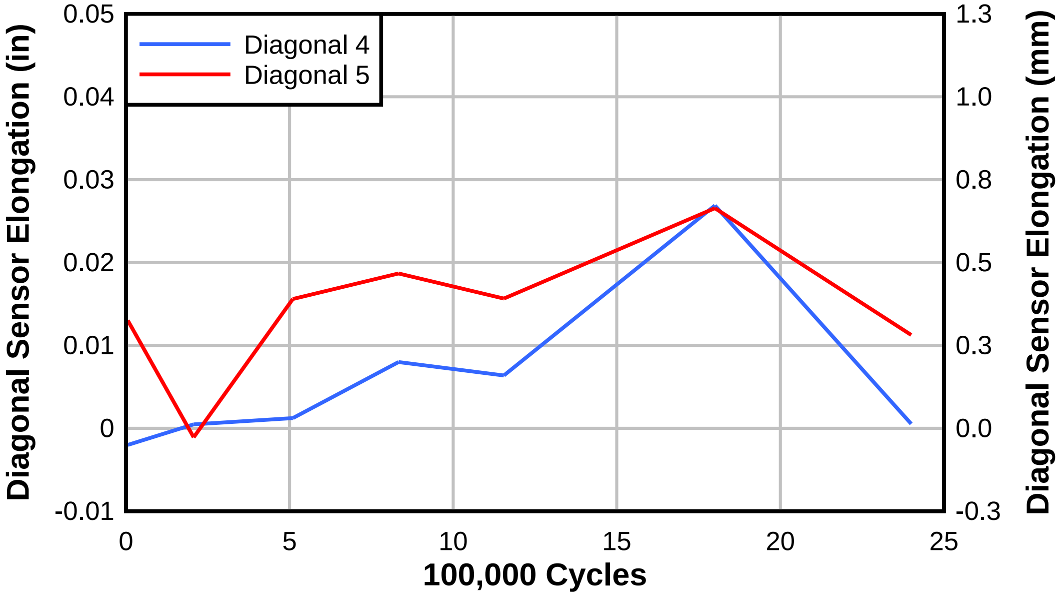

Figure A.54: Specimen IT6.18.12.E2.FTG fatigue diagonal sensor elongation

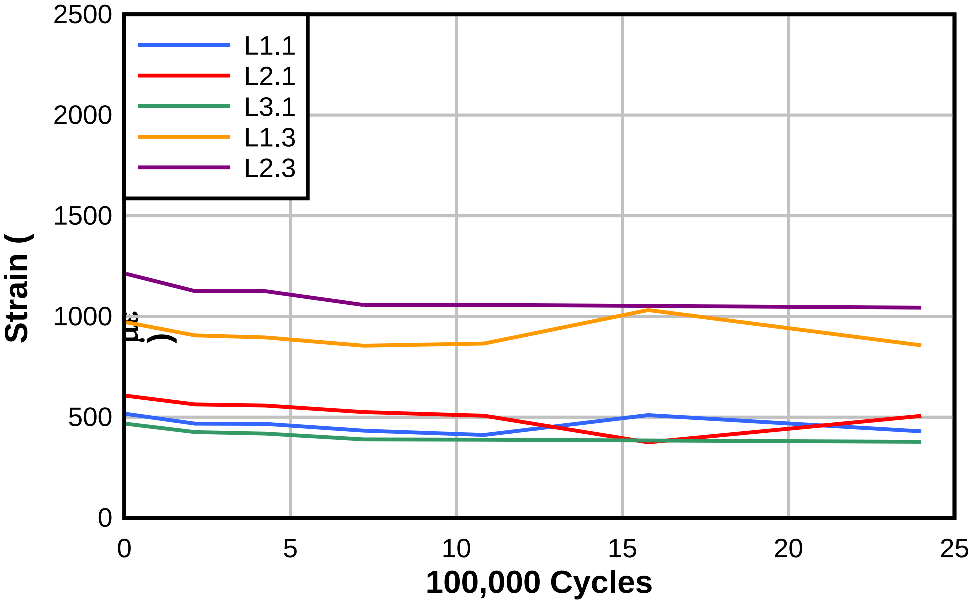

Figure A.55: Specimen IT6.18.12.E1.FTG fatigue long. strain at 210 kips (934 kN)

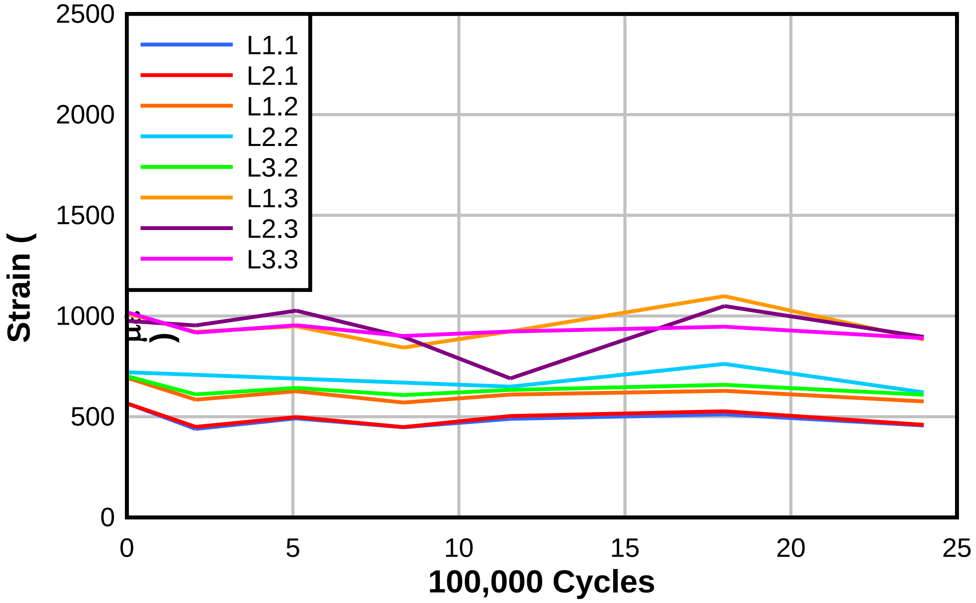

Figure A.56: Specimen IT6.18.12.E2.FTG fatigue long. strain at 210 kips (934 kN)

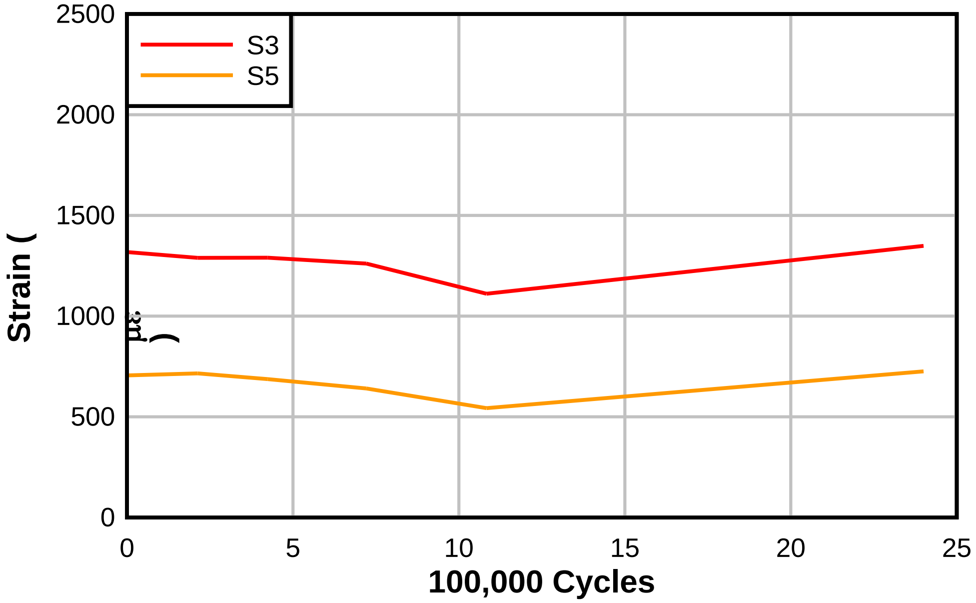

Figure A.57: Specimen IT6.18.12.E1.FTG fatigue stirrup strain at 210 kips (934 kN)

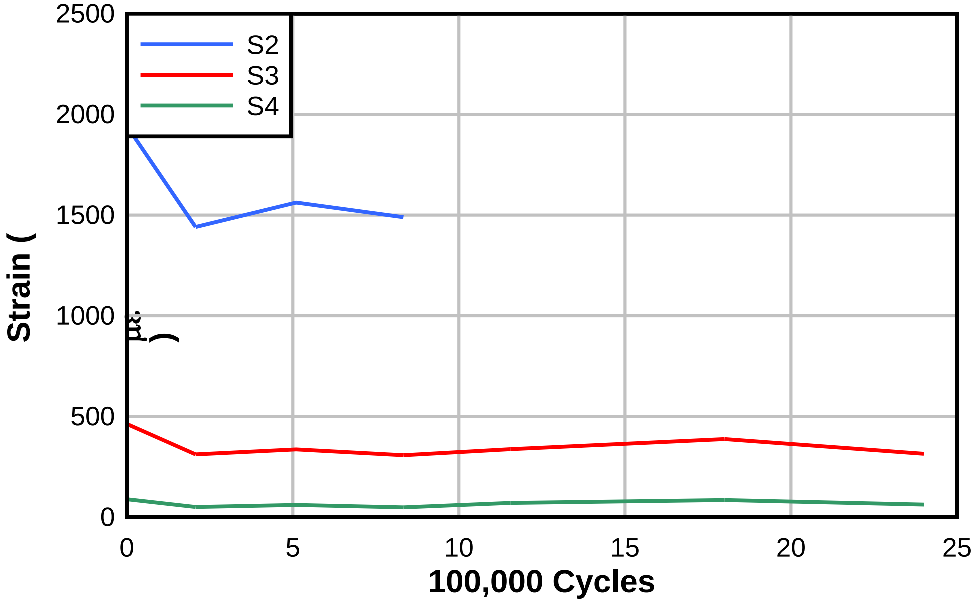

Figure A.58: Specimen IT6.18.12.E2.FTG fatigue stirrup strain at 210 kips (934 kN)

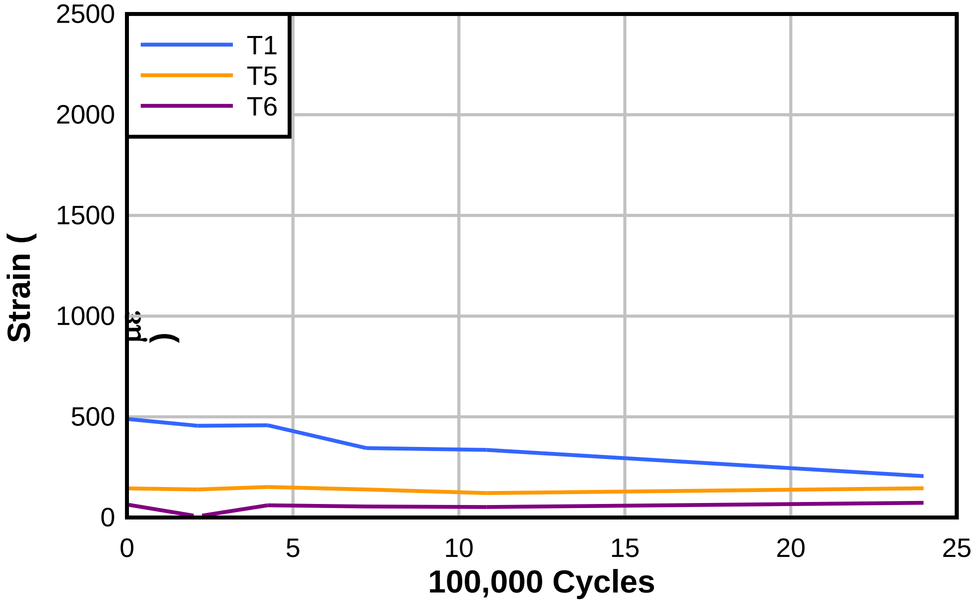

Figure A.59: Specimen IT6.18.12.E1.FTG fatigue titanium strain at 210 kips (934 kN)

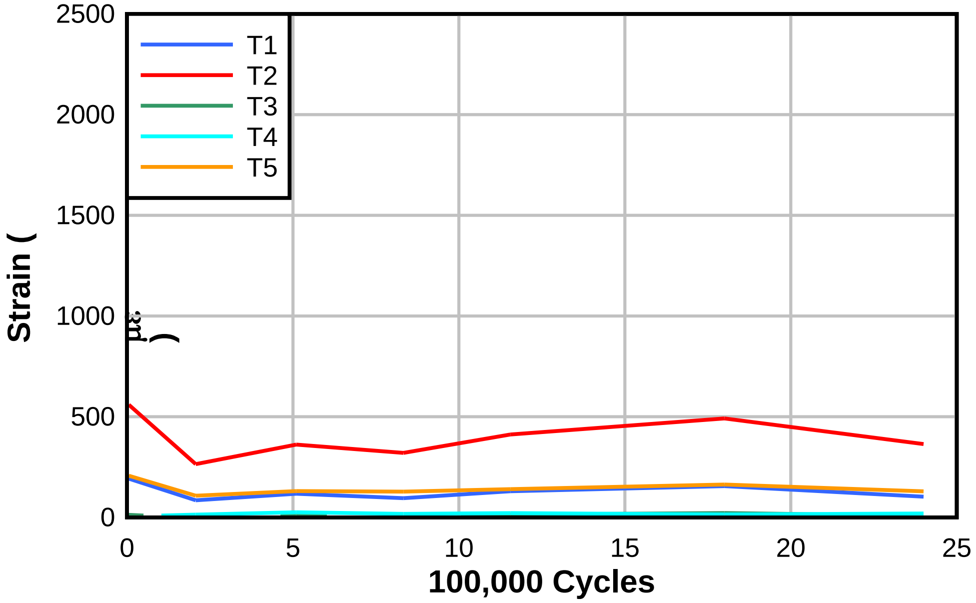

Figure A.60: Specimen IT6.18.12.E2.FTG fatigue titanium strain at 210 kips (934 kN)

APPENDIX B

B.0 TENSILE TEST RESULTS

Tensile tests were done on the internal reinforcing steel and NSM titanium alloy bars. A 110 kip (489 kN) Universal Testing Machine (UTM) was used for the tests. The samples were loaded at a rate of 0.0003 in/s (0.0076 mm/s) until strain hardening began, after which the test rate was gradually increased to 0.005 in/s (0.127 mm/s). The strain was measured using a 2 in. (51 mm) extensometer, which was removed prior to rupture in order to prevent damage. For bars that did not exhibit a clear yield plateau, the 0.2% offset method was used to determine the yield strength.

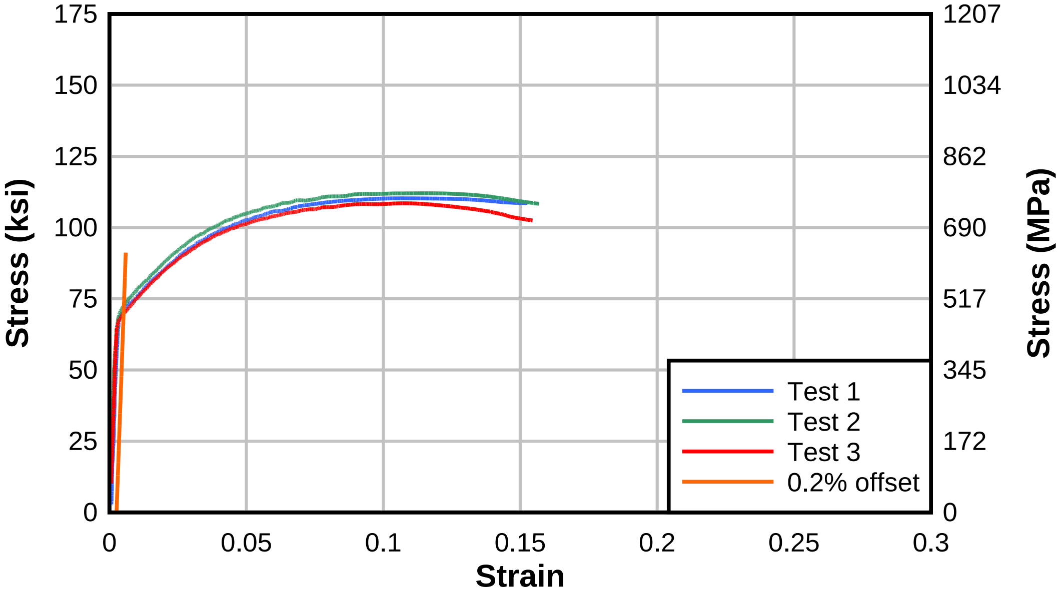

Figure B.1: Grade 60 #11 tensile test results

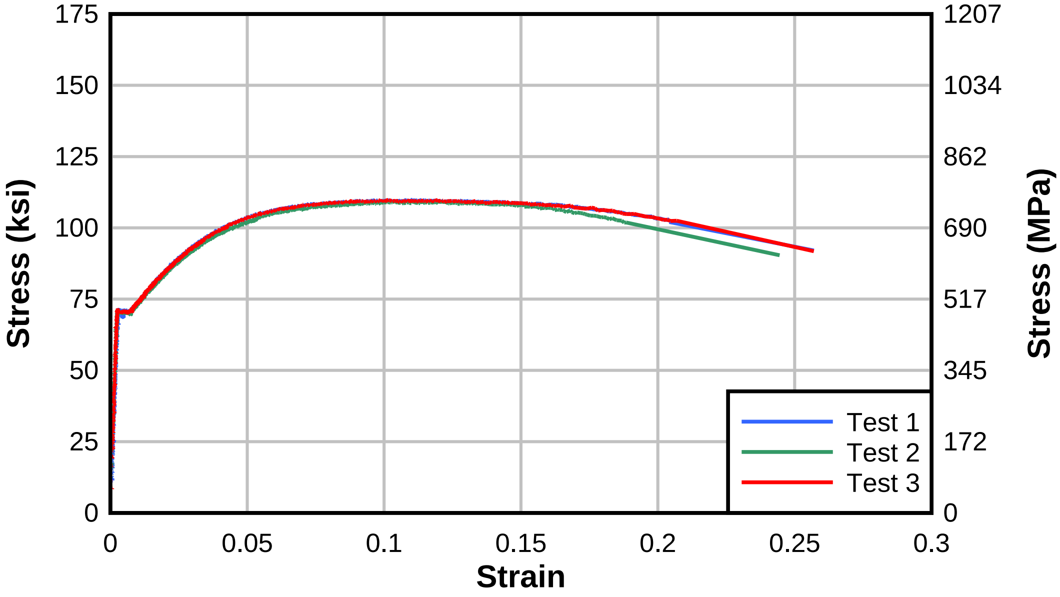

Figure B.2: Grade 60 #6 tensile test results

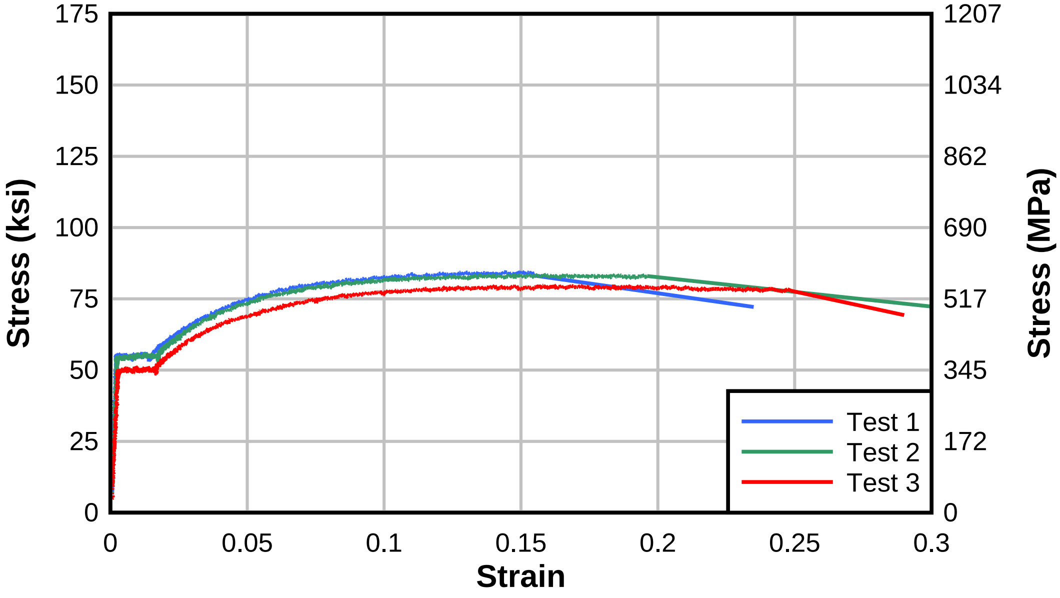

Figure B.3: Grade 40 #4 tensile test results

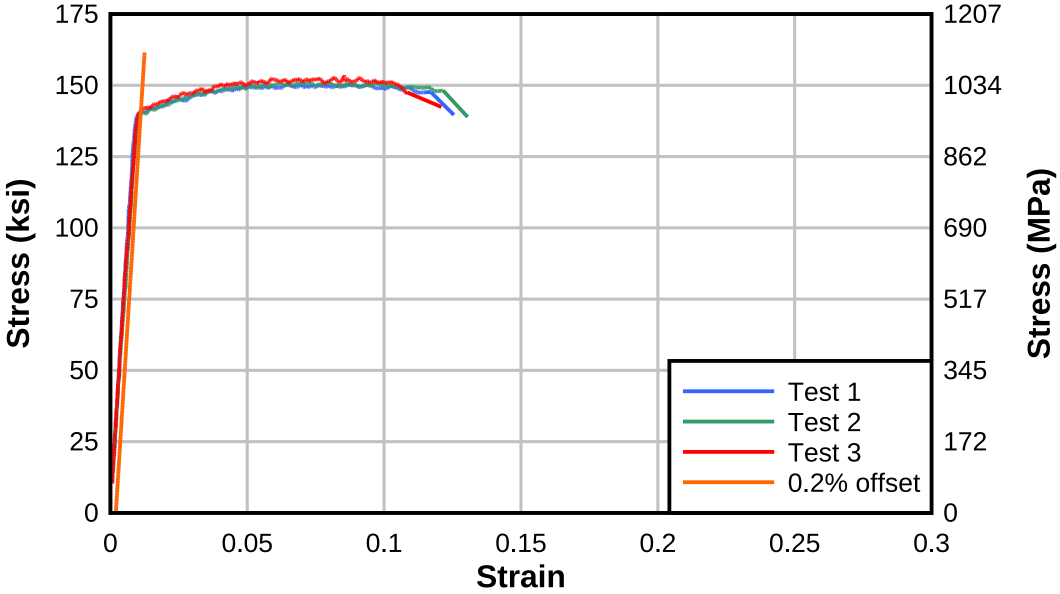

Figure B.4: 1/4 in. titanium alloy bar tensile test results – E1 specimens

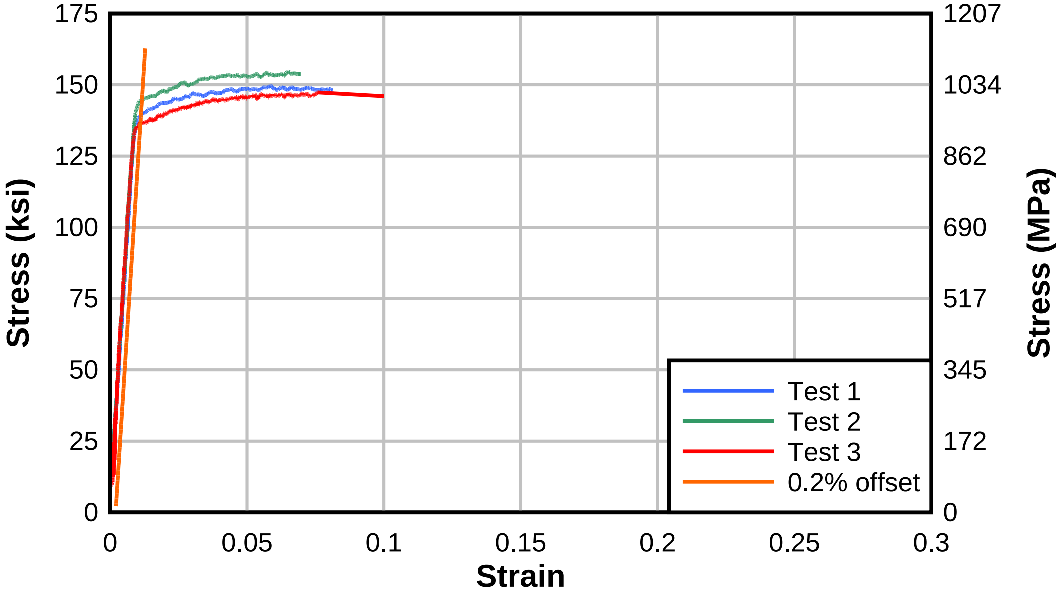

Figure B.5: 1/4 in. titanium alloy bar tensile test results – E2 specimens

APPENDIX C

C.0 R2K PREDICTION CURVES

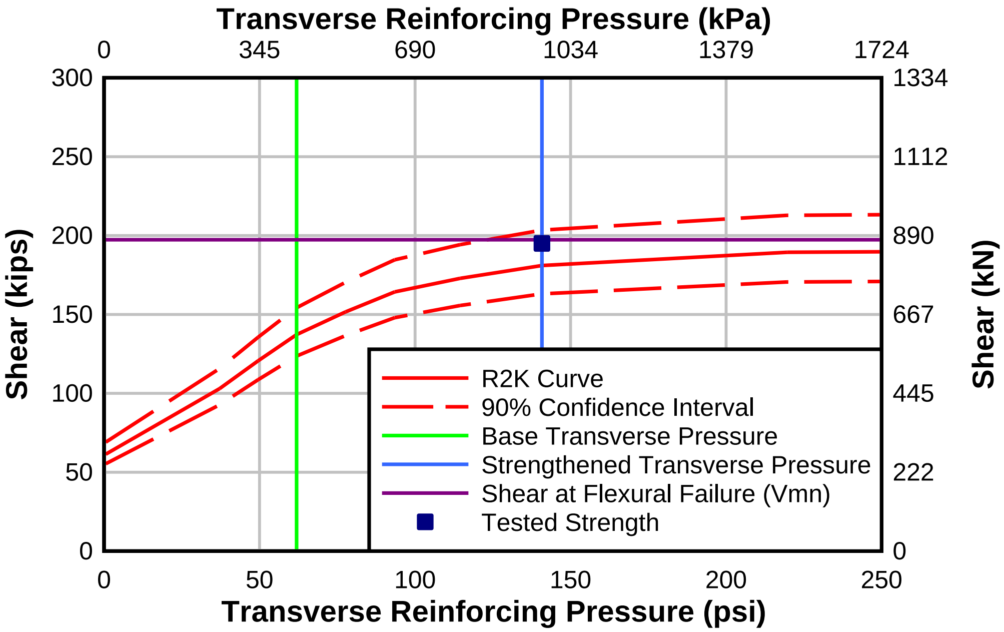

Figure C.1: Specimen T5.24.12.E1 R2K prediction curve

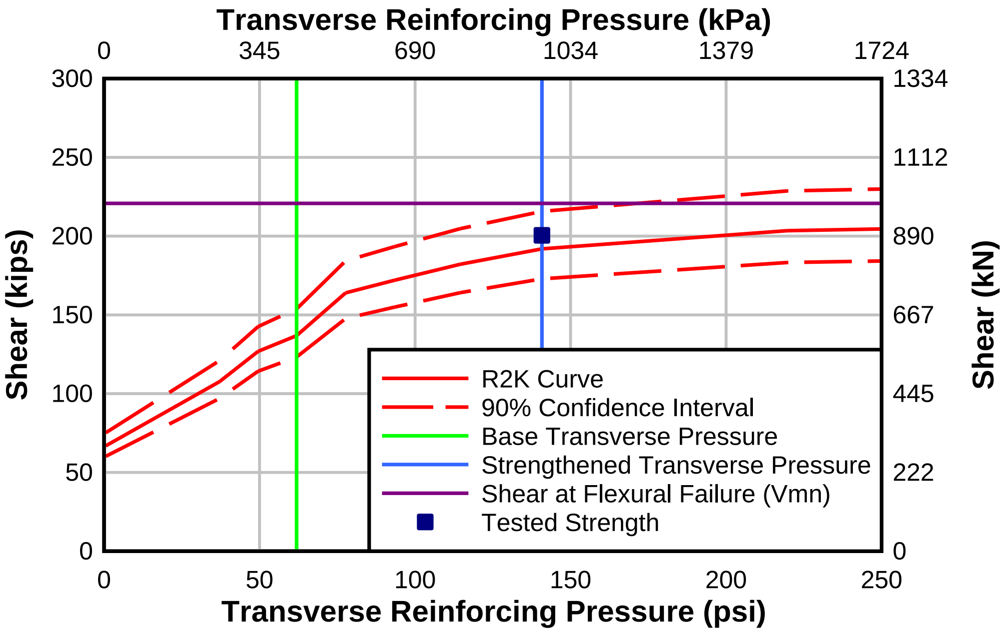

Figure C.2: Specimen T5.24.12S.E1* R2K prediction curve

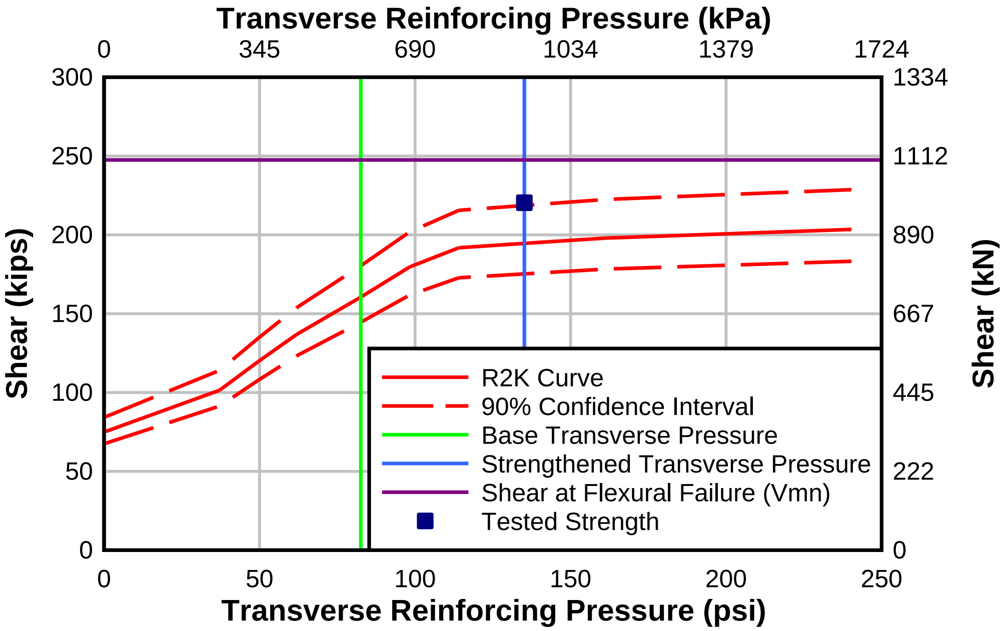

Figure C.3: Specimen IT6.18.18.E1 R2K prediction curve

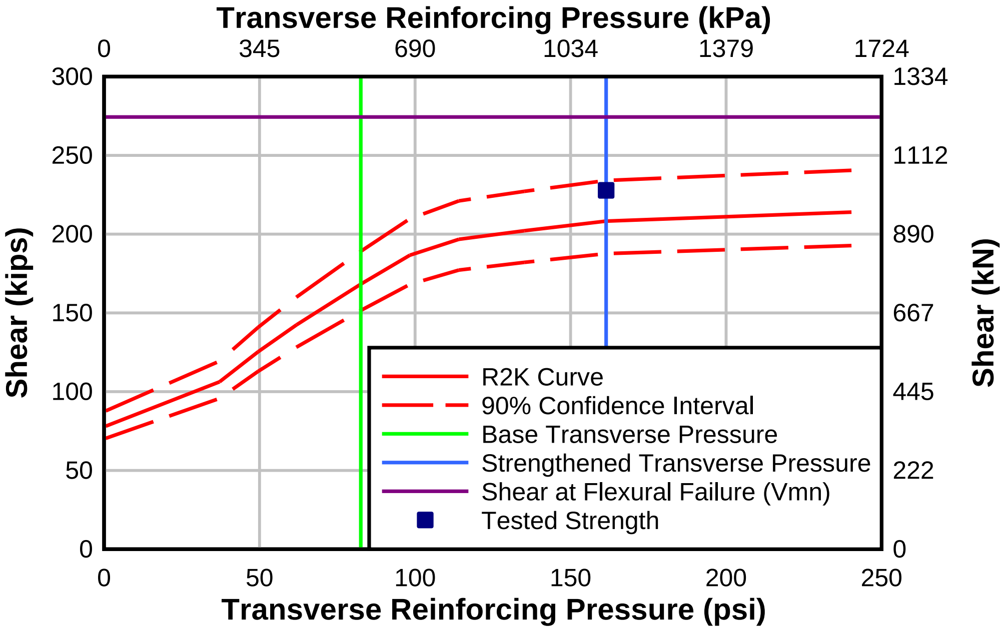

Figure C.4: Specimen IT6.18.12.E1 R2K prediction curve

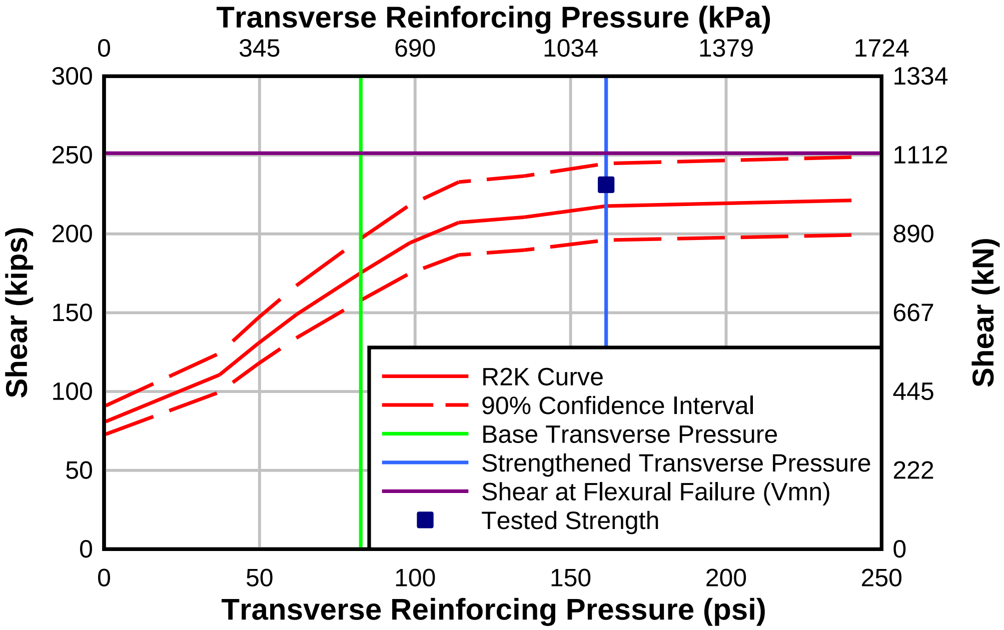

Figure C.5: Specimen IT6.18.12.E1.FTG R2K prediction curve

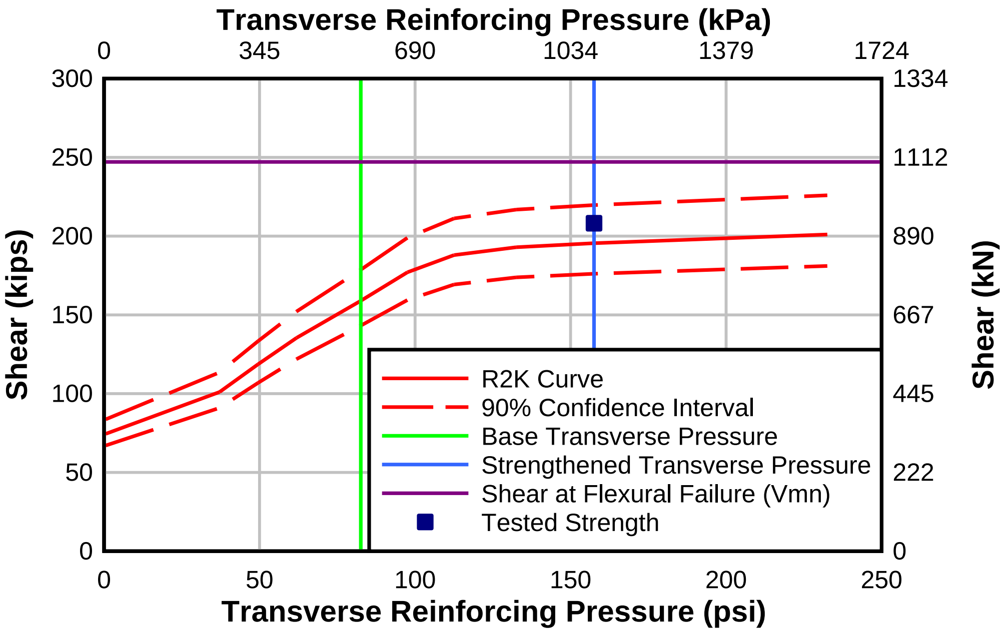

Figure C.6: Specimen IT6.18.12.E2 R2K prediction curve

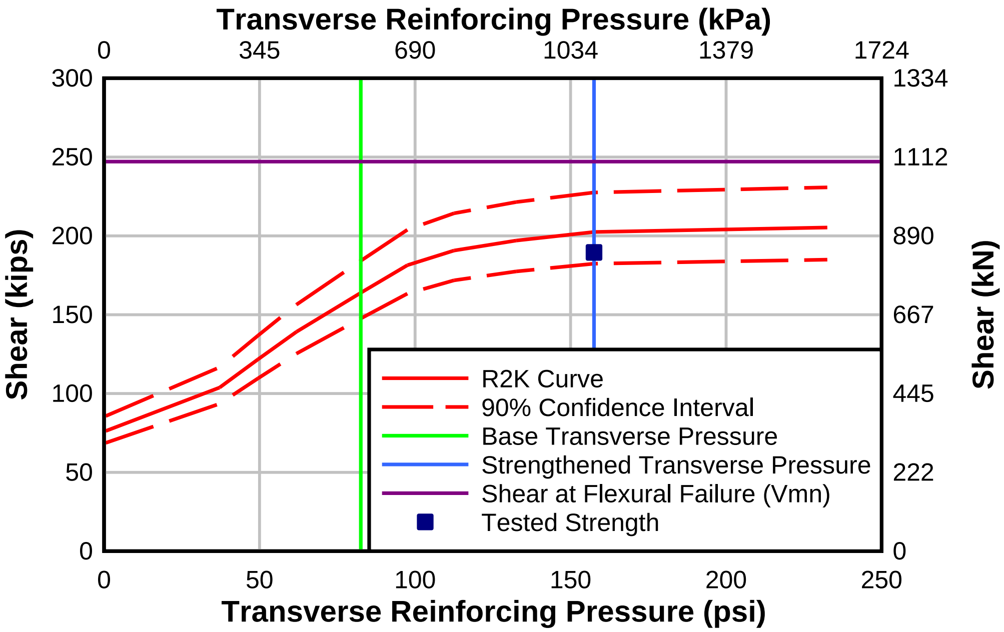

Figure C.7: Specimen IT6.18.12.E2.FTG R2K prediction curve

APPENDIX D

D.0 COST ESTIMATES

In order to illustrate the cost effectiveness of titanium, cost estimates were made for retrofits using titanium, stainless steel, and carbon fiber rods. The material properties and estimated unit costs are shown in Table D1. The bar spacing was adjusted such that each material gives a strength increase of 24.8 kips [110 kN], using the beam depth of the IT specimens tested in this research program. Because the bar spacings vary, this cost analysis was normalized by area, rather than by length. The unit costs are estimates, and do not represent actual quotes.

Table D.1: Material Properties

	Diameter in. [mm]	Yield ksi [MPa]	Spacing in [mm]	Unit cost USD/lb [kg]
Titanium	0.25 [6.4]	140 [965]	12.0 [305]	$38.50 [$84.88]
Stainless Steel	0.375 [9.5]	80 [552]	16.1 [409]	$4.18 [$9.21]
Carbon Fiber	0.375 [9.5]	64 [441]	12.9 [327]	$21.83 [$48.13]

The epoxy was assumed to cost $\$1.00/\text{in}^3$ [$61.33/L], based on the cost of the E1 epoxy. The costs of cutting the grooves and installing the NSM material could vary significantly, but was assumed to be $20.00 per cubic inch of concrete removed [$\$1.22/\text{cm}^3$]. The costs associated with cutting the grooves are shown in Table D2.

Table D.2: Groove Cutting Costs (USD) Per Square Foot [0.093 m^2]

	Groove width in. [mm]	Groove depth in. [mm]	Concrete removed in^3/sf [cm^3/m^2]	Cost USD
Titanium	0.375 [9.5]	0.5 [12.7]	2.25 [396]	$45.00
Stainless Steel	0.5 [12.7]	0.625 [15.9]	2.79 [492]	$55.85
Carbon Fiber	0.5 [12.7]	0.625 [15.9]	3.49 [615]	$69.82

The epoxy volume can be calculated as the volume of the NSM grooves less the volume occupied by the NSM material, while the costs of the NSM bar can be calculated directly based on the bar area. The material, epoxy, and labor costs per square foot of repair surface are shown in Table D3.

Table D.3: NSM Repair Costs (USD) Per Square Foot [0.093 m^2]

	NSM Bar	Epoxy	Labor	Total
Titanium	$3.47	$1.69	$45.00	$50.16
Stainless Steel	$1.17	$1.47	$55.85	$58.49
Carbon Fiber	$1.62	$2.17	$69.82	$73.60

These results demonstrate that despite titanium's high unit cost, it is ultimately more cost effective. This is because labor accounts for over 90% of the costs associated with these repairs. Thus even small savings in time and labor costs can have large effects, while changes in material costs have very small effects. Additionally, there are other cost savings associated with time, such as road closures and safety costs that were not included in this analysis. These would result in further savings when using titanium alloy bar.